



HAL
open science

Towards A Quantum Memory For Non-Classical Light With Cold Atomic Ensembles

Sidney Burks

► **To cite this version:**

Sidney Burks. Towards A Quantum Memory For Non-Classical Light With Cold Atomic Ensembles. Quantum Physics [quant-ph]. Université Pierre et Marie Curie - Paris VI, 2010. English. NNT : . tel-00699270

HAL Id: tel-00699270

<https://theses.hal.science/tel-00699270>

Submitted on 20 May 2012

HAL is a multi-disciplinary open access archive for the deposit and dissemination of scientific research documents, whether they are published or not. The documents may come from teaching and research institutions in France or abroad, or from public or private research centers.

L'archive ouverte pluridisciplinaire **HAL**, est destinée au dépôt et à la diffusion de documents scientifiques de niveau recherche, publiés ou non, émanant des établissements d'enseignement et de recherche français ou étrangers, des laboratoires publics ou privés.



LABORATOIRE KASTLER BROSSSEL



**DOCTORAL THESIS FOR
THE UNIVERSITÉ PIERRE ET MARIE CURIE**

Speciality: Quantum Optics

**Ecole Doctorale de Physique de la Particule à la Matière
Condensée**

Presented By

Sidney Burks

for the title of

Docteur de l'Université Pierre et Marie Curie

Thesis Subject :

**Towards A Quantum Memory For Non-Classical
Light With Cold Atomic Ensembles**

Defended October 13th, 2010 before the jury consisting of :

Mme Maria CHAMARRO

M. Thierry CHANELIERE

M. Thierry DEBUISSCHERT

Mme Elisabeth GIACOBINO

Mme Ottavia JEDRKIEWICZ

M. Julien LAURAT

Mme Rosa TUALLE-BROURI

Examiner

Examiner

Reporter

Thesis Director

Reporter

Co-Supervisor

Examiner

Abstract

A reversible quantum memory allowing us to store and retrieve quantum information serves as a key necessity for implementing many of novel quantum information protocols. As light serves as a reliable long-range carrier of quantum information, and atoms offer the possibility of long storage times, current attempts at creating quantum memories focus on the transfer of the quantum fluctuations of light onto atomic coherences. The work in this thesis focuses on the development of a quantum memory for squeezed light using an ensemble of cold Cesium atoms stored in a magneto-optical trap. Our two major milestones were the development of a source of nonclassical light, and the development of a suitable atomic medium for storage.

We first present the results of our efforts to generate a source of squeezed vacuum states resonant with the Cesium D_2 line using a PPKTP nonlinear crystal inside of an optical parametric oscillator. Additionally, we characterize these squeezed states by carrying out a quantum state tomography using an iterative maximum likelihood approach.

Next we look at the development of a new experiment which would allow us to use cold Cesium atoms as a storage medium in our recently developed magneto-optical trap. As this requires an array of novel tools and experimental techniques, we will discuss the development of these elements, and how they have furthered our progress towards storing quantum states onto our Cesium atoms, and eventually entangling two atomic ensembles.

Keywords: quantum optics, quantum information, continuous variables, quantum memory, optical parametric oscillator, squeezed states, entanglement, quantum tomography, electromagnetically induced transparency, cesium vapor.

Résumé

Une mémoire quantique réversible permettant de stocker et relire de l'information quantique est une composante majeure dans la mise en oeuvre de nombreux protocoles d'information quantique. Comme la lumière est un porteur de l'information quantique fiable sur des longues distances, et comme les atomes offrent la possibilité d'obtenir de longues durées de stockage, la recherche actuelle sur la création d'une mémoire quantique se concentre sur la transfert des fluctuations quantiques de la lumière sur des cohérences atomiques. Le travail réalisé durant cette thèse porte sur le développement d'une mémoire quantique pour la lumière comprimée, utilisant un ensemble d'atomes froids de Cesium stockés dans un piège magnéto-optique. Nos deux principaux objectifs étaient le développement d'une source de lumière non-classique, et le développement d'un milieu atomique pour le stockage de celle-ci.

Tout d'abord, nous commençons par présenter la construction d'un oscillateur paramétrique optique qui utilise un cristal nonlineaire de PPKTP. Cet OPO fonctionne comme source d'états de vide comprimé résonant avec la raie D_2 du Cesium. Nous caractérisons ces états grâce à une reconstruction par tomographie quantique, en utilisant une approche de vraisemblance maximale.

Ensuite, nous examinons une nouvelle expérience qui nous permet d'utiliser comme milieu de stockage des atomes froids de Césium dans un piège magneto-optique récemment développé. Car cette expérience exige l'utilisation de nouveaux outils et techniques, nous discutons le développement de ceux-ci, et comment ils ont contribué à notre progression vers le stockage des états quantiques dans nos atomes des Cesium, et finalement vers l'intrication de deux ensembles atomiques.

Mots clés: optique quantique, information quantique, variables continues, mémoire quantique, transparence induite électromagnétiquement, vapeur de césium, oscillateur paramétrique optique, états comprimés, intrication, tomographie quantique.

Acknowledgements

The work presented in this thesis results from the passionate efforts and support of many people, without whom none of the following results would have come into fruition.

I would like to begin by thanking Elisabeth Giacobino and Alberto Bramati for allowing me to join their Quantum Optics group and take part in their research.

An enormous thank you to Julien Laurat, who has supported me in every aspect of this work with his patience, encouragement, and trust, from the beginning through the end, and really made this work a success.

I would particularly like to thank Maria Chamarro, Thierry Chanelière, and Rosa Tualle-Brouri for accepting to take the time and effort to serve on the jury, alongside Ottavia Jedrkiewicz and Thierry Debuisschert, who have additionally agreed to serve as reporters for this thesis,

Antonino Chuimmo for introducing me to the OPO, and patiently teaching me as much as he possibly could in the short month we worked together,

Jean Cviklinski for acting as a role model of a researcher,

Jeremie Ortalo for his dedication in working with me side-by-side through all of the long hours developing the experiment for two years,

Xiaojun Jia for his insights on solving many of our problems in constructing the OPO,

Michael Scherman, Pietro Lombardi, Lambert Giner, and Lucile Veissier, and Oxana Mishina for all of their insights and discussion surrounding the experiment,

Jurgen Appel for his help with implementing the optical phase lock,

Bridgitte Delamour for her passion, attention to detail, and professionalism she put into her work,

Jean-Piere Okpizs for his excitement in developing new solutions to problems,

Mohammed Boujrad for working with me in developing microcontroller and FPGA based tools for our research,

Jean-Michel Isac, Pascal Travers, Alain Vogt, Chrisophe Rafaillac, Gael Coupin, and Arnaud Leclercq for their precision, diligence, and skill in creating new mechanical devices,

Eric LeBigot, Virginia D'Auria, Pierre Cladet, Benoit Chalopin, Olivier Pinel and Taoufik Amri for showing me other aspects of quantum optics beyond my immediate research,

My family for always pushing me to follow my dreams,

And most importantly, Elodie Culoma, my Sweetiedumonde, for being the most loving, patient, supportive sweetiedumonde ever.

Contents

Introduction	1
I Introduction to Quantum Optics	5
1 Motivation for a Quantum Memory	7
1.1 Applications of a Quantum Memory	7
1.2 Research Avenues	9
1.3 Our Approach	10
2 Continuous Variable Quantum Optics	11
2.1 Quantum States	12
2.1.1 The Density Operator	12
2.1.1.1 Properties of the Density Operator	13
2.1.2 The Wigner Representation	13
2.1.2.1 Properties of the Wigner Function	14
2.2 Quantum States of the Electric Field	15
2.2.1 Vacuum States	17
2.2.2 Fock States	17
2.2.3 Coherent States	18
2.2.4 Squeezed States	19
2.2.5 Operator Linearization	20
2.2.6 Noise Characterization	21
2.3 Quantum Correlations	22
2.3.1 Separability Criterion	22
2.3.2 States Incident on a Beamsplitter	22
2.3.3 Effects of Optical Losses	24

II	Squeezed Light Production With an OPO	25
3	Squeezed Light Production With Nonlinear Optics	27
3.1	Nonlinear Optics	28
3.1.1	Propagation Equations	28
3.2	Nonlinear Processes	28
3.2.1	Coupled Wave Equations	29
3.2.2	Second-Harmonic Generation	30
3.2.2.1	Nonlinear Efficiency	31
3.2.2.2	Cavity-Enhanced SHG	31
3.2.3	Parametric Down-Conversion	33
3.2.4	Phase Matching	35
3.3	Optical Parametric Amplification and Oscillation	35
3.3.1	Below Threshold Parametric Gain	37
3.3.2	Quantum Noise Below Threshold	38
4	Experimental Setup of the OPO	41
4.1	Optical Setup	42
4.1.1	Laser Source	42
4.1.1.1	Optical Fibers	42
4.1.2	OPO Table	43
4.1.2.1	Cavity Generalities	44
4.2	Nonlinear Crystal	45
4.2.1	Selection Characteristics	45
4.2.1.1	Quasi-Phase Matching	45
4.2.1.2	Periodic-Poling	46
4.2.1.3	Phase-Matching Angle	46
4.2.1.4	Nonlinear Coefficient	47
4.2.1.5	Phase-Matching Temperature	47
4.2.1.6	Damage Threshold	47
4.2.1.7	Blue Light Induced Losses	47
4.2.2	Implementation Parameters	48
4.2.2.1	Optical Losses	48
4.2.2.2	Temperature Control	48
4.2.2.3	Optimal Focusing	48
4.3	Doubling Cavity	50
4.3.1	Intracavity Losses	51
4.3.2	Tilt Locking	51
4.3.3	Second-Harmonic Generation Results	53
4.3.3.1	Nonlinear Efficiency	53
4.3.3.2	Phase-Matching Temperature	54

4.3.3.3	SHG Efficiency	54
4.4	OPO Cavity	56
4.4.1	Cavity Locking	57
4.4.1.1	Tilt Locking Attempts	57
4.4.1.2	Pound-Drever-Hall Locking	58
4.4.1.3	Electronic Implementation	59
4.4.2	Pump Matching	59
4.4.3	Classical Observations	60
4.4.3.1	OPO Threshold	60
4.4.3.2	Type I OPO Degeneracy	61
4.4.3.3	OPO Above Threshold	61
4.4.3.4	OPO Injected Below Threshold	62
5	Detection and Characterization of Squeezed Light	65
5.1	Balanced Homodyne Detection	66
5.1.1	Measuring the Rejection Ratio of Subtraction	68
5.1.2	Electronic Noise Floor	69
5.1.3	Detector Balancing	70
5.1.4	Visibility	70
5.2	Continuous-Wave Squeezing Measurements	71
5.2.1	Comparison With Theory	73
5.2.2	Accounting for Losses	73
5.3	Quantum State Tomography	74
5.3.1	Homodyne Measurements	74
5.3.2	Tomographic Reconstruction	75
5.3.3	Maximum Likelihood Estimation	75
5.3.4	Experimental Implementation	76
5.4	Creation of Pulses of Squeezed Light	78
5.4.1	AOM Implementation	79
5.4.2	Optical Chopper Implementation	80
5.4.2.1	Optical Detection Losses Due To Pulse Edges	80
5.4.2.2	Real Pulse Envelope	81
5.4.2.3	Slit Selection	82
5.4.2.4	Beam Focusing	83
5.4.2.5	Chopper Selection	83
5.4.2.6	Rotating Disc	84
5.4.2.7	Disc Balancing	84
5.4.2.8	Disc Geometry	85
5.4.2.9	Pulse Measurements	85
5.4.2.10	Noise	87
5.4.2.11	Vibrations	87

5.4.2.12	Jitter	87
Publication		89
III Preparation of a Quantum Memory With Cold Atoms		95
6	Experimental Tools for the Storage of Squeezed Light	97
6.1	Introduction	98
6.1.1	Optical Storage Through EIT	98
6.2	Phase Lock	99
6.2.1	Theory	100
6.2.1.1	Frequency Division	101
6.2.1.2	Phase-Frequency Detection	101
6.2.2	Experimental Setup	102
6.2.3	Analysis	107
6.3	The Magneto-Optical Trap	107
6.3.1	Basic Trapping Principles	108
6.3.2	MOT Characteristics	109
6.3.3	Laser Sources	110
6.3.3.1	Locking	111
6.3.4	Controlling the Magnetic Field	112
6.3.4.1	Control Signal	113
6.3.4.2	Labview Interface	114
6.3.4.3	Program Operation	114
6.3.4.4	Results	118
6.3.5	Timing	118
6.4	Optical Layout	120
6.4.1	Beam Displacers	123
6.4.2	Signal Beam	124
6.4.3	Local Oscillator	124
6.4.4	Control Beam	124
6.4.5	Auxiliary Beam	125
6.5	Optical Density Measurements	125
6.5.1	Implementation	126
6.6	Raman Scheme for the Compensation of the Magnetic Field	127
6.6.1	Raman Spectroscopy	129
6.6.2	Labview Interface	130
6.7	Conclusion	131

7	Usage of an FPGA for Timing Applications	133
7.1	Digital Timekeeping	134
7.1.1	Software Based Clocks	135
7.1.2	Hardware Based Clocks	136
7.1.2.1	RC Oscillators	136
7.1.2.2	Crystal Oscillators	137
7.1.3	Digitizing the Oscillator	137
7.2	FPGA Digital Circuits	138
7.2.1	Programming an FPGA	139
7.2.1.1	Higher Level Programming	139
7.2.1.2	NI Labview and Labview FPGA	140
7.2.2	The Labview FPGA Programming Model	142
7.3	Basics Concepts in Digital Logic	145
7.3.1	Data Representation	145
7.3.2	Digital Input and Output (DIO)	145
7.3.3	Integers	146
7.3.4	Floating Point Numbers	146
7.4	Basic Building Blocks for Timing Applications	147
7.4.1	Describing a Pulse	147
7.4.2	Labview Timer Implementation	148
7.4.2.1	Digital Input and Output	150
7.4.2.2	Detecting Edge Transitions	151
7.4.3	Labview Implementation	151
7.4.4	Implementing the Pulse generator	151
7.4.5	Putting the Blocks Together	153
7.5	Experimental Application	153
7.5.1	Laser Timing via Pulse Delay Generation	155
7.5.2	Chopper Period Measurement	156
7.6	Where to find Source Code	157
	Conclusion	159
	Appendix	161
A	Matisse Laser	163
A.1	Laser Locking	163
A.1.1	Cavity Locking	164
A.1.2	Saturated Absorption	165
B	Chopper Disc Diagram	167
C	Electronic Diagrams	169
	Bibliography	175

List of Figures

1.1	Quantum repeater schematic	9
2.1	Wigner function for Coherent state	19
2.2	Wigner of Squeezed State	20
2.3	Electric fields incident on a beamsplitter	23
2.4	Beamsplitter model of optical losses	24
3.1	Photon model of second-harmonic generation	30
3.2	Cavity-enhanced SHG	32
3.3	Photon model of parametric down-conversion	33
3.4	Optical parametric amplification	36
3.5	Parametric gain vs. pump parameter	38
3.6	OPO squeezing	40
4.1	Polarization alignment for fiber optics	43
4.2	OPO table block diagram	44
4.3	Quasi-phase matching in a nonlinear crystal	46
4.4	Doubling cavity geometry	50
4.5	Tilt locking schematic	51
4.6	Experimental tilt locking error signal	52
4.7	Nonlinear efficiency measurement	53
4.8	SHG output vs. temperature	54
4.9	SHG output efficiency vs input coupler and pump power	55
4.10	SHG output vs. fundamental input	56
4.11	OPO cavity geometry	57
4.12	Pound-Drever-Hall block diagram	59
4.13	Experimental Pound-Drever-Hall error signal	60
4.14	Type I crystal degeneracy	62
4.15	OPO above-threshold operation	63
4.16	Below-threshold parametric gain	63

5.1	Fresnel representation of direct and homodyne detection	66
5.2	Homodyne detection schematic	67
5.3	Homodyne detection noise floors	69
5.4	Homodyne detector optical balancing	70
5.5	Squeezed vacuum at 1.5 MHz with scanned LO phase	72
5.6	Broadband and low-frequency squeezing	72
5.7	Estimation of squeezing production in our OPO	74
5.8	Digitized photocurrents of shot noise and vacuum squeezing	77
5.9	Density matrix estimated using iterative MLE	77
5.10	Wigner functions for shot noise and squeezed state	78
5.11	Schematic for AOM optical pulse generation	80
5.12	Illustration of a pulse generated by an optical chopper	81
5.13	Chopper pulse model with gaussian profile	82
5.14	Thorlabs 200 μm slit	83
5.15	Scitec 310CD Chopper	84
5.16	Optical timing sequence for pulse generation	84
5.17	Custom designed disc for optical chopper	85
5.18	Optical chopper pulse measurements	86
5.19	Acoustic isolation box for dampening chopper noise	87
5.20	Chopper vibration isolation stack	88
6.1	EIT transitions for Cesium quantum memory	99
6.2	PLL block diagram	100
6.3	Phase-frequency detector logic diagram	101
6.4	PFD output signal	102
6.5	OPLL optical table photo	102
6.6	OPLL block diagrams	103
6.7	Optical PLL beat note demodulated to 400 MHz	104
6.8	PLL circuit block diagram	104
6.9	PLL circuit photo	105
6.10	OPLL integrator and diode current modulation circuits	105
6.11	OPLL error signal	106
6.12	Phase lock results	106
6.13	MOT illustration and transitions	108
6.14	Glass MOT chamber	109
6.15	Laser diode	110
6.16	Block diagram for diode table	111
6.17	Saturated absorption Doppler measurements	112
6.18	B-Field control signal	115
6.19	B-Field control generation code	116
6.20	B-Field generator Labview code	117

6.21	Magnetic field extinction times	118
6.22	MOT timing diagram	119
6.23	Photo of MOT layout	121
6.24	Optical layout for MOT	122
6.25	Beam displacer schematic	123
6.26	Optical density block diagram	126
6.27	Optical density measurement	127
6.28	Optical density and Raman spectroscopy Labview interface	128
6.29	Raman spectroscopy transitions	129
6.30	Raman timing diagram	130
6.31	Raman detuning scanner block diagram	132
7.1	Electronic Comparator	137
7.2	FPGA Picture	138
7.3	Black box representation of HDLs	139
7.4	Half Adder Logic	139
7.5	Half Adder in Labview	141
7.6	Labview project window	143
7.7	Example FPGA vi for digital input and output	144
7.8	Example host vi	144
7.9	Short Caption	145
7.10	Abstract Representation Of a Pulse	147
7.11	Timebase With Reference Point	148
7.12	Timebase	148
7.13	Labview Counter Implementations	149
7.14	Clock Timer	149
7.15	Digital Output	150
7.16	Digital Input	150
7.17	Digital Input Representation	151
7.18	Edge Transitions in Labview	152
7.19	Pulse Generator	152
7.20	Digital delay generator project	153
7.21	Digital delay generator FPGA.vi	154
7.22	Digital delay generator Host.vi	155
7.23	DDG Subvis	155
7.24	MOT timing interface	156
7.25	Chopper pulse acquisition	156
8.1	Matisse laser ring cavity	163
8.2	Matisse Commander fast piezo	164
8.4	Matisse slow piezo lock	165
8.5	Chopper disc mechanical diagram	168

8.6	PDH photodiode circuit	170
8.7	Tilt Locking photodiode circuit	171
8.8	PDH integrator circuit	172
8.9	Tilt Locking integrator circuit	173

Introduction

Quantum Information vs. Classical Information

The field of Quantum Information has developed rapidly over the last few decades. Quantum Mechanics has allowed us to manipulate light and matter in new ways, permitting us to observe phenomenon that have no classical parallel. Many of these phenomenon arise due to core quantum principles such as the Heisenberg Uncertainty Principle, and the superposition of states. As a result, this has led to a shift from our classical definitions of information towards the concept of quantum information. The fundamental element at the core of quantum information is the quantum bit, or *qubit*. While classical bits allow us to represent information as discrete values of 1 or 0, qubits take advantage of quantum superposition, which allows them to represent information as 1, 0, or a superposition of both values.

This characteristic of qubits has led to the development of novel protocols concerning information transfer, calculation, and computation that are impossible to implement when only considering classical bits of information. One of the first insights on ways to benefit from using quantum information was proposed by Feynman in 1981, when he suggested that we use a quantum computer to simulate the evolution of quantum systems [Feynman, 1982]. Shortly afterwards in 1984, Bennett and Brassard developed a protocol to use secure quantum channels for the distribution of cryptographic keys [Bennett and Brassard, 1984]. This was quickly followed by the work of Deutsch, who developed the first model of a quantum Turing machine, thus giving us a means to analyze quantum algorithms using quantum logic gates [Deutsch, 1985]. In 1991, Ekert continued the exploration of quantum information transfer by developing a protocol for secure communication based on quantum entanglement [Ekert, 1991]. Research concerning the usage of quantum information for calculations continued throughout the 1990s with the development of Shor's algorithm in 1994, which provided a means to rapidly factor large numbers using a quantum computer [Shor, 1994], and Grover's algorithm, which provided a means of using quantum information to search an unsorted database [Grover, 1996].

All of these protocols concerning the manipulation of quantum information rest

on the premise that we preserve the quantum superposition of our qubits. Preserving the quantum superposition requires us to avoid measuring the value of a qubit, which would force it to take on a well-defined value and destroy its quantum characteristics. This poses a problem if we approach these protocols with our classical treatment of information, as quantum mechanics imposes a no-cloning theorem which forbids us from making exact copies of unknown quantum states. This limitation has sparked the need to develop a new means of preserving quantum information for long-term manipulation and storage.

Quantum Memories

A reversible quantum memory allowing us to store and retrieve quantum information serves as a key necessity for implementing many of these quantum information protocols. We could for example, use a quantum memory as a deterministic single-photon source, which would serve as an important element in optical quantum computing. Quantum memories would also resolve a critical problem with the long-distance transfer of quantum information. The optical propagation of photons in fiber optic cables is subject to losses, which limits the distance over which we can transfer optical qubits. Quantum repeaters could be developed to bypass this limitation by entangling photons at both ends of our communications chain, but this is only possible if quantum memories are used to temporarily store quantum states. It is this context that has motivated our group to work towards the development of a quantum memory.

Research at the Laboratoire Kastler-Brossel

Over the last 20 years, the Quantum Optics group at the Laboratoire Kastler-Brossel has focused on studying the quantum-optical effects of light-matter interactions in Cesium atoms. There have been a variety of experiments carried out to study the quantum noise reduction in cavities and with cold atoms by Laurent Hilico [Hilico, 1992], Astrid Lambrecht [Lambrecht, 1995], Thomas Coudreau [Coudreau, 1997], and Vincent Josse [Josse, 2003]. The theses of Laurent Vernac [Vernac, 2001] and Auriel Dantan [Dantan, 2005] have developed the theoretical work concerning quantum electromagnetic fluctuations and their transfer towards atoms via light-matter interactions. Most recently, the work of Jean Cviklinski [Cviklinski, 2008] and Jeremie Ortalo [Ortalo, 2009] has yielded the development and characterization of an atomic memory for coherent states with warm atoms, and an experimental study of electromagnetically-induced transparency in Cesium.

Thesis Outline

Part [I](#) of this thesis begins with a theoretical overview of the general quantum optics concepts used to carry out the experimental work shown here. We define the quantum states of the electromagnetic field, and show how we can represent those states using the density matrix and Wigner function. We then proceed to discuss the nonlinear optics of light as it passes through a nonlinear material, and show how we can use these interactions to generate squeezed states.

In Part [II](#), we look at the experimental setup used to create an optical parametric oscillator, which allows us to generate squeezed vacuum states resonant with the Cesium D2 line at 852 nm. We then look at the techniques used to characterize these states using quantum homodyne tomography and iterative maximum likelihood estimation. We finish by discussing the approaches that we developed to convert our continuous source of squeezed light into pulses compatible with our quantum memory.

Finally in Part [III](#), we look at the development of a new experiment which would allow us to use cold Cesium atoms as a storage medium in our recently developed magneto-optical trap. As this requires an array of novel tools and experimental techniques, we will discuss the development of these elements, and how they have furthered our progress towards storing quantum states onto our Cesium atoms, and eventually entangling two atomic ensembles.

Part I

Introduction to Quantum Optics

Motivation for a Quantum Memory

The aim of a quantum memory is to provide a means of storing information encoded into quantum states, and allow a mechanism for reliable, on-demand retrieval. As light serves as a reliable long-range carrier of quantum information, and atoms offer the possibility of long storage times, current attempts at creating quantum memories focus on the transfer of the quantum fluctuations of light onto atomic coherences. We can establish a performance metric for a quantum memory by using measurements such as its storage and retrieval efficiency, the conditional or non-conditional fidelity of its output state as a representation of its input state, the overall storage lifetime, and our ability to store arbitrary quantum states in it. Other considerations for a quantum memory include the wavelength of light to which it responds, the number of frequential modes we can store inside of it simultaneously, and the bandwidth of light it supports. Despite current attempts at implementing a quantum memory, as of yet there is no system available that shows a high performance with regards to all of these characteristics.

1.1 Applications of a Quantum Memory

We can define a quantum memory as a coherent and reversible transfer of qubits to and from a storage medium, such that our retrieved state superposition is a faithful representation of the original stored state.

$$\underbrace{\alpha |0\rangle + \beta |1\rangle}_{\text{Input state}} \rightarrow \underbrace{\alpha |a\rangle + \beta |b\rangle}_{\text{Stored state}} \rightarrow \underbrace{\alpha |0\rangle + \beta |1\rangle}_{\text{Retrieved state}}. \quad (1.1)$$

A quantum memory for light is a necessary component in several systems which would permit the advanced manipulation of quantum information.

One of the simplest usages of a quantum memory is as an on-demand source of single photons. If we create a pair of photons simultaneously using a system such as parametric down-conversion, we can store one of the photons in the quantum memory, and use the detection of the second photon to signal that our memory has been *prepared*. Once the memory is charged with a photon, we can release it on demand with the assurance that it yields a single-photon state.

Another usage of a quantum memory would be as a component of a quantum computer. Current quantum algorithms require the manipulation of entangled qubits, which are often processed in parallel for each step in a computation. We can use a quantum memory as a timing mechanism which stores qubits while other steps of the computation are being prepared so they can be processed at the right moment. In this way, a quantum memory would serve as a synchronizing tool for quantum computations [Lvovsky *et al.*, 2009].

We can also envision the usage of a quantum memory for long-range quantum communication. The promise of unbreakable quantum communications channels depends on protocols such as quantum key distribution, which require the exchange of qubits over long distances. Fiber optic cables at the telecom 1550 nm wavelength typically have attenuation levels of 0.25 dB/km, and experiments with the detection of entangled photons has resulted in the detection of around 100 qubits/second [Hubel *et al.*, 2007]. Due to attenuation losses, transferring quantum states through fiber optic cables is currently limited to a few hundred kilometers.

Using a quantum repeater protocol illustrated in Figure 1.1 would allow us to bypass this limitation [Briegel *et al.*, 1998], [Duan *et al.*, 2001]. We can begin by defining two points A_0 and A_N separated by a distance L , over which we would like to entangle two quantum states. One way to accomplish this is by first dividing our distance up into N segments. At the end of each segment, we can place a twin photon source, which we can use to entangle each segment with its neighboring segment. By entangling each sub-segment with its neighbor, we can swap entanglement over the entire length L .

One problem with this approach however, is that entangling the path extremities via entanglement swapping is a process that must be properly synchronized, so that the entanglement of every segment node happens simultaneously. This poses a problem because the probability of experiencing an entanglement error in at least one of the nodes increases exponentially as the number of nodes increase, and as a result, so does the time required to simultaneously entangle all nodes.

A solution to this would be to place a quantum memory at each node, which would allow us to temporarily store our entangled photons while the other nodes were being prepared, allowing us to independently entangle each segment. Once all of the nodes were in a prepared state, we could then carry out the entanglement swapping over the entire distance. This would lower the probability of error to a polynomial order with increasing distance, as opposed to exponential, thus rendering our long-distance

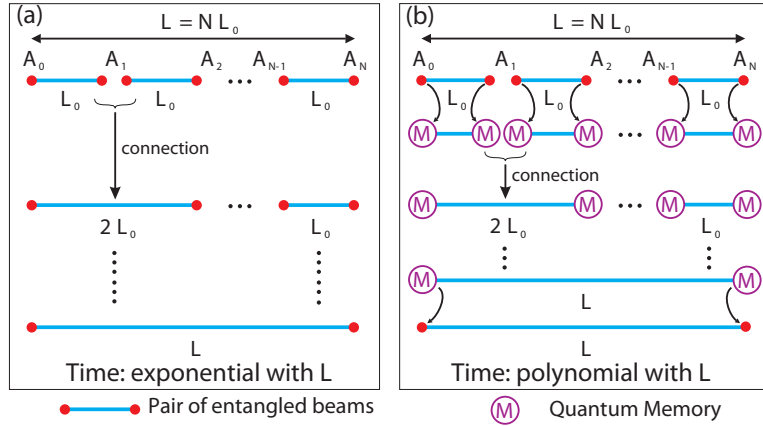


Figure 1.1: Diagram of the protocol for distributing photon entanglement between points A_0 and A_N . Length L is divided into N segments, which are connected by quantum repeaters. Entanglement is shared between segments via entanglement swapping at the nodes. a) Entanglement swapping along the entire length requires perfect synchronization, and a time exponential in the path length. b) Placing a quantum memory at each node facilitates the synchronization, and reduces the time to a polynomial time with path length.

communication practical. As in the case of quantum computation, a quantum memory makes quantum repeaters practical by synchronizing the entanglement of states.

As these applications all show the potential promise of novel ways to manipulate quantum information, they provide a great motivation for the development of a performant quantum memory.

1.2 Research Avenues

The last 10 years have seen a large development in the research attempts in constructing a quantum memory. Numerous methods exist for preserving the quantum state of light, but the most promising techniques for longer storage times are those using large ensembles of atoms. Work such as that done by [Chanelière *et al.*, 2005], and [Eisaman *et al.*, 2005] has succeeded in the storage and retrieval of single-photon states. The work of [Julsgaard *et al.*, 2004] has shown the ability to use continuous-variable quantum non-demolition techniques to achieve high efficiencies and storage times in Cesium, yet they have only allowed the retrieval of a single quadrature of light. Photon-echo techniques have also been explored in order to preserve the atomic coherences, and thus extend the overall memory storage time. Work done by [Alexander *et al.*, 2006] in 2006 using Controlled Reversible Inhomogenous Broadening (CRIB) has been applied in Pr doped solid-state Y_2SiO_5 crystals cooled to 4 K, however with low efficiency re-

sults. Other photon-echo techniques such as the usage of an Atomic Frequency Comb (AFC) have been demonstrated showing a 9% storage efficiency of weak photon pulses [Chanelière *et al.*, 2010]. The usage of EIT as a storage mechanism has also yielded results by several groups. In the work of [Choi *et al.*, 2008], entangled states were successfully stored and retrieved from Cesium vapor. Several groups have also succeeded in the storage and retrieval via EIT of coherent states in Cesium vapor [Cviklinski, 2008], and squeezed vacuum states in Rubidium vapor [Appel *et al.*, 2008], [Honda *et al.*, 2008], [Arikawa *et al.*, 2009].

1.3 Our Approach

Our approach towards the construction of a quantum memory focuses on the transfer of squeezed vacuum states onto Cesium cloud trapped and cooled in a magneto-optical trap (MOT). We wish to transfer the quadrature fluctuations of the light field onto the collective spin of Cesium atoms stored in an magneto-optical trap, and after the storage time of a few tens of microseconds, re-emit the light to show the preservation of quadrature squeezing. Once this is accomplished, we aim to carry out the storage in two atomic ensembles, and show the ability of our system to preserve the entanglement of two remote ensembles.

Continuous Variable Quantum Optics

Contents

2.1 Quantum States	12
2.1.1 The Density Operator	12
2.1.2 The Wigner Representation	13
2.2 Quantum States of the Electric Field	15
2.2.1 Vacuum States	17
2.2.2 Fock States	17
2.2.3 Coherent States	18
2.2.4 Squeezed States	19
2.2.5 Operator Linearization	20
2.2.6 Noise Characterization	21
2.3 Quantum Correlations	22
2.3.1 Separability Criterion	22
2.3.2 States Incident on a Beamsplitter	22
2.3.3 Effects of Optical Losses	24

In this chapter, we will review the foundations of quantum mechanics and quantum optics, and explore the different quantum states of the electromagnetic field. We will then examine how to manipulate these quantum states to produce non-classical correlations in optical beams.

2.1 Quantum States

The postulates of quantum mechanics give us a way of defining the state of a system and its observable quantities that is fundamentally different from that used in classical mechanics. The first axiom says that the state of a system at a fixed time is defined by a state vector $|\psi\rangle$. We can represent a state vector as a superposition of basis states by

$$|\psi\rangle = \sum_n c_n |n\rangle \quad p_n = |c_n|^2 = \frac{|\langle n|\psi\rangle|^2}{\langle\psi|\psi\rangle} \quad \sum |c_n|^2 = 1, \quad (2.1)$$

where each of the c_n coefficients represent a complex amplitude of the eigenvector $|n\rangle$, and the probability amplitudes $|c_n|^2$ are subject to a normalization condition. Upon measurement, we have a probability p_n of detecting the system in the state $|n\rangle$. Within this framework, observable quantities are represented by Hermitian operators \hat{O} , whose expected value can be calculated by

$$\langle \hat{O} \rangle_{|\psi\rangle} = \sum_n c_n \langle n | \hat{O} | n \rangle. \quad (2.2)$$

When we know for certain that a system exists within a uniquely given state, we can refer to this state as a *pure state*, and the state vector $|\psi\rangle$ encompasses all of the information that we can obtain about the system. We can, however, imagine a more general case of a system that is composed of an ensemble of sub-states $|\psi_n\rangle$, where each sub-state appears in the ensemble with a probability P_n . We can thus describe this system, as a *statistical mixture* of pure states, or a *mixed state*, where

$$\sum_i P_i = 1. \quad (2.3)$$

2.1.1 The Density Operator

We can introduce the *density operator* $\hat{\rho}$ as a means of representing a system composed of mixed states, using the expression

$$\hat{\rho} = \sum_n P_n |\psi_n\rangle \langle \psi_n|. \quad (2.4)$$

This operator fully describes the quantum state of the system as it encompasses the complex coefficients for the pure states available to our system, as well as the fact that we only have probabilistic information P_n about precisely which state our system is in. Furthermore, the density operator allows us to calculate all of the information

that quantum mechanics can provide about the system, whether the system be in a precisely known pure state, or in a statistical mixture of states.

2.1.1.1 Properties of the Density Operator

The density operator has several properties which allow us to make predictive measurements about our system. If we have an Hermitian observable \hat{O} , then we can calculate the expectation value of our observable using [Cohen-Tannoudji *et al.*, 1973]

$$\langle \hat{O} \rangle = \sum_n P_n \langle \psi_n | \hat{O} | \psi_n \rangle = \text{Tr}(\hat{O}\hat{\rho}). \quad (2.5)$$

The density operator also has the following properties: it is Hermitian, its trace equals 1, and it is positive semi-definite

$$\hat{\rho}^\dagger = \hat{\rho} \quad \text{Tr}(\hat{\rho}) = 1 \quad \langle \psi | \hat{\rho} | \psi \rangle = \sum_n P_n |\langle \psi | \psi_n \rangle|^2 \geq 0. \quad (2.6)$$

We can use the density operator to distinguish between pure states and mixed states by using the *purity*, which is given by [Gerry and Knight, 2005]

$$\text{Tr}(\hat{\rho}^2) \quad \text{with} \quad \text{Tr}(\hat{\rho}^2) \leq 1. \quad (2.7)$$

The equality holds only when the state is a pure state, whereas for mixed states, $\text{Tr}(\hat{\rho}^2) < 1$. Furthermore, by using Equation 2.8 and the system's Hamiltonian \mathcal{H} , we can determine the dynamic properties of our system

$$i\hbar \frac{\partial \hat{\rho}}{\partial t} = [\mathcal{H}, \hat{\rho}]. \quad (2.8)$$

A complete specification of $\hat{\rho}$ allows us to determine the values of all measurable quantities allowed by quantum mechanics. For this reason, we consider the density operator as the most general representation of a quantum state.

2.1.2 The Wigner Representation

Although the density operator $\hat{\rho}$ provides the most general representation of a quantum state, it still remains an abstract concept which provides us with little intuition about the information contained in a system's state. We can seek a more illustrative representation of the information contained in the density matrix by using the *Wigner Function* [Wigner, 1932].

The Wigner function has its conceptual origins in classical and statistical physics, where for a classical statistical ensemble, it is possible to specify the state of the system by precise, simultaneous measurements of its conjugate phase space variables q and p

[Schleich, 2001]. A measurement of these variables would allow us to create a phase-space probability distribution $\mathcal{W}(q, p)$, which would permit the prediction of any other quantities related to the system.

An attempt to similarly predict the quantities involved with a quantum system is not as straightforward however. Quantum mechanics prevents us from carrying out the precise, simultaneous measurement of q and p due to their non-commutativity, thus there is no way to create a *true* quantum phase space distribution for our system.

Instead of using a true phase space distribution, we can suppose that there exists a function $\mathcal{W}(q, p)$ which acts like joint probability distribution for q and p . The Wigner function fits this characteristic, and allows us to relate the system's density matrix to a quasi-probability distribution through the following definition [Schleich, 2001]:

$$\mathcal{W}(q, p) = \frac{1}{2\pi\hbar} \int_{-\infty}^{\infty} e^{-\frac{i}{\hbar}p\xi} \left\langle q + \frac{1}{2}\xi \left| \hat{\rho} \right| q - \frac{1}{2}\xi \right\rangle d\xi. \quad (2.9)$$

We can express the Wigner function for a state as a Fourier transform of its density matrix, and in the cases of pure states where $\hat{\rho} = |\psi\rangle\langle\psi|$ and given the wavefunction $\psi(x) = \langle x | \psi \rangle$, we can express it as a Fourier transform of position-shifted wavefunctions

$$\mathcal{W}(q, p) = \frac{1}{2\pi\hbar} \int_{-\infty}^{\infty} e^{-\frac{i}{\hbar}p\xi} \psi^* \left(q - \frac{1}{2}\xi \right) \psi \left(q + \frac{1}{2}\xi \right) d\xi. \quad (2.10)$$

We can define the *marginal distributions* as the true probability distributions of q and p individually. By integrating $\mathcal{W}(q, p)$ over q or p , we can obtain these marginal distributions for q and p respectively [Leonhardt, 1997]

$$W(q) = \int_{-\infty}^{\infty} \mathcal{W}(q, p) dp \quad \text{and} \quad W(p) = \int_{-\infty}^{\infty} \mathcal{W}(q, p) dq. \quad (2.11)$$

These marginals serve as projections of the Wigner function onto the axis of our q and p coordinates, thus while we cannot measure the entire Wigner function at once, we can measure the marginal projections of it.

2.1.2.1 Properties of the Wigner Function

The Wigner function has certain properties that make it useful for describing quantum states [Schleich, 2001]. It acts like a probability distribution through its normalization constraint

$$\int_{-\infty}^{\infty} \int_{-\infty}^{\infty} \mathcal{W}(q, p) dq dp = 1, \quad (2.12)$$

and it is purely real for Hermitian operators $\hat{\rho}$, such that

$$\mathcal{W}(q, p)^* = \mathcal{W}(q, p). \quad (2.13)$$

Additionally, $\mathcal{W}(q, p)$ satisfies a trace rule, which allows us to evaluate the overlap of two density operators

$$Tr(\hat{\rho}_1 \hat{\rho}_2) = 2\pi\hbar \int_{-\infty}^{\infty} \int_{-\infty}^{\infty} \mathcal{W}_{\hat{\rho}_1}(q, p) \mathcal{W}_{\hat{\rho}_2}(q, p) dq dp. \quad (2.14)$$

Using this trace rule, we can once again evaluate the expectation value of an operator \hat{O} using

$$\langle \hat{O} \rangle = Tr(\hat{\rho} \hat{O}) = 2\pi\hbar \int_{-\infty}^{\infty} \int_{-\infty}^{\infty} \mathcal{W}_{\hat{\rho}}(q, p) \mathcal{W}_{\hat{O}}(q, p) dq dp, \quad (2.15)$$

or similarly, we can determine the purity $Tr(\hat{\rho}^2)$ of a state by

$$Tr(\hat{\rho}^2) \leq 1 \Rightarrow 2\pi\hbar \int_{-\infty}^{\infty} \int_{-\infty}^{\infty} \mathcal{W}_{\hat{\rho}}^2(q, p) dq dp \leq 1. \quad (2.16)$$

The Wigner function is positive when describing Gaussian states, but can take on negative values when we use it to describe non-gaussian states. When $\mathcal{W}(q, p) < 0$, we interpret this as a strong signature of non-classical behavior. Because of its ability to take on negative values under certain conditions, we consider it to be a *quasiprobability* distribution as opposed to a true probability distribution.

Finally, the overlap formula allows us to express the density matrix in terms of the Wigner function in a given basis by using the relation shown in [Leonhardt, 1997]

$$\langle \psi_a | \hat{\rho} | \psi_b \rangle = Tr(\hat{\rho} | \psi_b \rangle \langle \psi_a |) = 2\pi\hbar \int_{-\infty}^{\infty} \int_{-\infty}^{\infty} \mathcal{W}(q, p) \mathcal{W}_{\psi_a \psi_b}(q, p) dq dp. \quad (2.17)$$

These properties shows us that we can treat the Wigner function as a true representation of a quantum state, and use it for the calculation of relevant quantities.

2.2 Quantum States of the Electric Field

Light serves as an extremely useful tool in the study of quantum states, and the development of lasers over the last 50 years has allowed us to easily create highly coherent sources of light. By using these light sources, we can easily encode information and transmit it over long distances. Additionally, as light is well understood in the classical

domain, by studying its uniquely quantum properties we can further our understanding of quantum mechanics.

In the previous section, we have reviewed several means of describing the quantum states of a system. Here, we will begin to apply this formalism to the electromagnetic field. First, we will begin with a classical description of the electric field, and show how through its quantization, it is possible to produce uniquely quantum states of light whose properties have no classical analogues.

We begin with the classical expression for a single mode electric field:

$$E(t) = |E_0| \cos(\omega t + \phi) = E_1 \cos(\omega t) + E_2 \sin(\omega t). \quad (2.18)$$

Through this description, we see that we have two canonical variables available for describing the E-field: either the field amplitude E_0 and phase ϕ , or the quadrature components of the field E_1 , and E_2 .

We can develop a similar quantum expression for the E field by replacing the classical quadratures with quantum operators

$$\hat{E}(t) = \hat{E}_1 \cos(\omega t) + \hat{E}_2 \sin(\omega t). \quad (2.19)$$

By using the non-commuting photon annihilation and creation operators \hat{a} and \hat{a}^\dagger , we can rewrite these quantum quadrature operators in the form

$$\hat{E}_1 = \hat{a} + \hat{a}^\dagger \quad \hat{E}_2 = i(\hat{a}^\dagger - \hat{a}) \quad [\hat{a}, \hat{a}^\dagger] = 1. \quad (2.20)$$

When performing measurements on our state, it is useful to specify our measurements in terms of a *generalized quadrature* \hat{X}_θ , which is a linear combination of our two quadrature operators \hat{E}_1 and \hat{E}_2 [Fabre, 1990]

$$\hat{X}_\theta = \hat{E}_1 \cos\theta + \hat{E}_2 \sin\theta = \hat{a} e^{-i\theta} + \hat{a}^\dagger e^{i\theta}. \quad (2.21)$$

Through the commutation relation of the boson operators given in Equation 2.20, we can derive the commutation relationship for the field quadratures, and see that they do not commute

$$[\hat{E}_1, \hat{E}_2] = 2i. \quad (2.22)$$

The non-commutativity of these two quadratures tells us that any simultaneous measurement on them both will only result in a limited precision measurement, which we can quantify by defining the *variance* of our measure as

$$\Delta \hat{E}_i^2 = \langle \hat{E}_i^2 \rangle - \langle \hat{E}_i \rangle^2. \quad (2.23)$$

We can then use the generalized uncertainty principle given in Equation 2.22 to derive an uncertainty relationship between the two quadrature variances

$$\Delta\hat{A}\Delta\hat{B} \geq \frac{1}{2i} \left\langle \left[\hat{A}, \hat{B} \right] \right\rangle. \quad (2.24)$$

Using Equation 2.22 with this uncertainty relation tells us that any simultaneous measurement of the two quadrature components will yield a certain amount of imprecision in the measurement. Thus, the result of our measurement will be subjected to a *quantum noise*.

$$\Delta\hat{E}_1\Delta\hat{E}_2 \geq 1. \quad (2.25)$$

2.2.1 Vacuum States

Now that we have a quantum expression for the electric field, we can begin to look at the quantum optical states that we can produce. The most fundamental state is the vacuum state $|0\rangle$, which is a purely quantum state that has no classical analogue. The mean number of photons $\langle\hat{n}\rangle$ in the vacuum state is 0, however because we cannot violate the uncertainty principle given above, the variances of the photon number can never go to 0

$$\langle\hat{n}\rangle = \langle 0 | \hat{n} | 0 \rangle = 0 \quad \text{and} \quad \Delta\hat{E}_1 = \Delta\hat{E}_2 = 1. \quad (2.26)$$

This restriction tells us that even in the vacuum state with an average photon number of 0, we observe noise fluctuations in our quadrature measurements. The vacuum state has symmetric variances in both quadratures, which allows it to satisfy the equality given by Equation 2.25. By satisfying this equality, we can call this state a *minimum uncertainty* state whose noise fluctuations are at the *standard quantum limit* (SQL). We can express the Wigner function for the vacuum state by [Leonhardt, 1997]

$$\mathcal{W}(q, p) = \frac{1}{\pi} e^{-q^2 - p^2}. \quad (2.27)$$

2.2.2 Fock States

The next set of states that we can consider are the Fock or *number* states [Fox, 2006]. The Fock state represents a state that contains a precisely well-defined number of photons, thus a completely undefined phase. We can define the number operator \hat{n} in terms of the annihilation and creation operators

$$\hat{n} = \hat{a}^\dagger \hat{a}. \quad (2.28)$$

The action of the number operator on a number state vector gives us the number of photons present in that state, and shows us that the variance of the photon number is 0

$$\hat{n} |n\rangle = n |n\rangle \quad \text{and} \quad \text{Var}(\hat{n}) = 0. \quad (2.29)$$

Fock states containing photons have symmetric noise variances, but are not minimum uncertainty states

$$\Delta \hat{E}_1 = \Delta \hat{E}_2 = \sqrt{2n + 1}. \quad (2.30)$$

We can express the Fock state for a given photon number as a series of photon creation operations acting on the vacuum state.

$$|n\rangle = \frac{\hat{a}^{\dagger n}}{\sqrt{n!}} |0\rangle. \quad (2.31)$$

The Fock states have a Wigner function given by

$$\mathcal{W}(q, p) = \frac{(-1)^n}{\pi} e^{-q^2 - p^2} L_n(2q^2 + 2p^2), \quad (2.32)$$

where the $L_n(x)$ represent the Laguerre polynomials [Leonhardt, 1997].

2.2.3 Coherent States

Mathematically, we can construct a coherent state by applying the *displacement operator* $\hat{D}(\alpha)$ to the vacuum state $|0\rangle$ [Scully and Zubairy, 1997]. Coherent states $|\alpha\rangle$ are considered as quantum states which most closely resemble classical states

$$\hat{D}(\alpha) = e^{\alpha \hat{a}^\dagger - \alpha^* \hat{a}} = e^{\frac{1}{2}|\alpha|^2} e^{\alpha \hat{a}^\dagger} e^{-\alpha^* \hat{a}} \quad (2.33)$$

$$\hat{D}(\alpha) |0\rangle = |\alpha\rangle. \quad (2.34)$$

We can use Equation 2.33 to express the coherent states as an expansion of Fock states [Glauber, 1963]

$$|\alpha\rangle = e^{-\frac{|\alpha|^2}{2}} \sum_n \frac{\alpha^n}{\sqrt{n!}} |n\rangle. \quad (2.35)$$

We can also calculate the probability of a coherent state having a given number of photons $P(n)$, and we see that this probability follows *Poisson* statistics [Fox, 2006]. Thus due to our ability to approximate classical states with coherent states, we can define classical states of light as having Poissonian statistics

$$P(n) = |\langle n | \alpha \rangle|^2 = \frac{|\alpha|^{2n} e^{-|\alpha|^2}}{n!} \quad (2.36)$$

As Equation 2.37 shows, we can express coherent states as eigenstates of the annihilation operator \hat{a}

$$\hat{a} |\alpha\rangle = \alpha |\alpha\rangle. \quad (2.37)$$

Coherent states have equal variances in their quadratures, and an optical beam composed of coherent states has a mean number of photons that is proportional to its intensity $|\alpha|^2$

$$\Delta \hat{E}_1 = \Delta \hat{E}_2 = 1 \quad \Delta \hat{n} = |\alpha| \quad \langle \hat{n} \rangle = |\alpha|^2. \quad (2.38)$$

The Wigner function of a coherent state is given by Equation 2.39

$$\mathcal{W}(q, p) = \frac{1}{\pi} e^{-(q-q_0)^2 - (p-p_0)^2}. \quad (2.39)$$

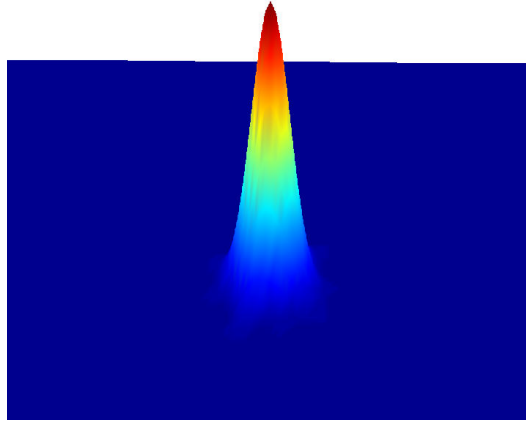


Figure 2.1: Wigner function depicting a coherent state

2.2.4 Squeezed States

Squeezed states are another example of purely quantum states. We can create a squeezed state through the action of the squeezing operator [Garrison and Chiao, 2008]

$$\hat{S}(\zeta) = e^{\frac{1}{2}(\zeta^* \hat{a}^2 - \zeta \hat{a}^{\dagger 2})}, \quad (2.40)$$

where we define ζ as the squeezing parameter

$$\zeta = r e^{i\phi}. \quad (2.41)$$

Squeezed states respect the uncertainty principle in that the product of the quadrature variances has a minimum value, however, the quadrature variances are not equal. Thus, we can obtain a variance in one quadrature measurement that goes below the standard quantum limit, at the expense of an increased variance in the other measurement. Squeezed states have a mean photon number that is a function of the magnitude of squeezing parameter r , and $|\alpha|^2$ where $\alpha = \langle \hat{a} \rangle$ [Gerry and Knight, 2005]

$$\Delta \hat{E}_1 = e^{-r} \quad \Delta \hat{E}_2 = e^r \quad \langle \hat{n} \rangle = |\alpha|^2 + \sinh(r). \quad (2.42)$$

One important type of squeezed state that we will discuss is the squeezed vacuum, whose Wigner function we can express with [Leonhardt, 1997]

$$\mathcal{W}(q, p) = \frac{1}{\pi} \exp(-e^{2\zeta} q^2 - e^{-2\zeta} p^2). \quad (2.43)$$

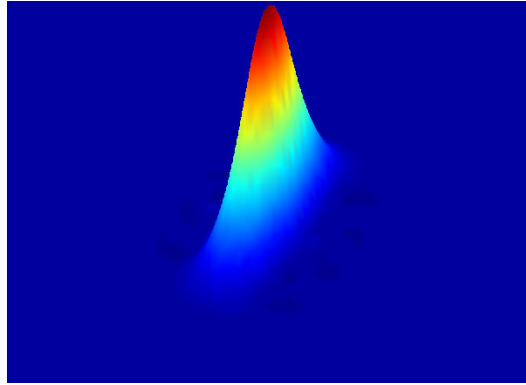


Figure 2.2: Wigner function for a squeezed state representing -2.6 dB of quadrature squeezing

2.2.5 Operator Linearization

We can linearize our quantum operators by decomposing them into a steady-state classical term, and a fluctuating term, and assuming that the classical term has a much larger amplitude than the fluctuating term [Fabre, 1990]. If we take the annihilation and creation operators \hat{a} and \hat{a}^\dagger as examples, we can represent them in the following form

$$\hat{a}(t) = \alpha + \delta\hat{a}(t) \quad (2.44)$$

$$\hat{a}^\dagger(t) = \alpha^* + \delta\hat{a}^\dagger(t) \quad (2.45)$$

$$|\alpha| \gg |\delta\hat{a}(t)|. \quad (2.46)$$

In this decomposition, the first term α represents a classical value, which is the time-averaged value $\langle \hat{a} \rangle$ of the annihilation operator, and the second term $\delta\hat{a}(t)$ represents the first order fluctuation where we assume that the mean value of the fluctuating term is zero.

This technique provides us with an alternative decomposition of our quantum operators, which can often allow us to solve many problems using analytical approaches. By using this decomposition, we can express our noise variance directly as a function of our fluctuating term

$$\left(\Delta\hat{O}\right)^2 = \left\langle (\delta\hat{O})^2 \right\rangle. \quad (2.47)$$

2.2.6 Noise Characterization

One problem with using the variance directly for characterizing noise can arise in a case where the variance diverges, such as when we measure white noise. This divergence occurs due to high-frequency fluctuations in our signal. In practice, our measurement of noise takes place over a finite frequency bandwidth which filters our noise spectrum. We can thus obtain a more precise characterization of our noise for a quadrature $\hat{X}(t)$ by using the autocorrelation function [Courty, 2005]

$$C_{\hat{X}}(\tau) = \left\langle \delta\hat{X}(t)\delta\hat{X}^\dagger(t') \right\rangle. \quad (2.48)$$

When $C(\tau)$ only depends on the time difference between two instants such that $\tau = t - t'$, we can take the Fourier transform of the autocorrelation function to obtain the noise spectral density

$$S_{\hat{X}}(\Omega) = \int_{-\infty}^{\infty} C_{\hat{X}}(\tau)e^{i\Omega\tau} d\tau. \quad (2.49)$$

We can relate the autocorrelation function of our Fourier-transformed quadrature to the noise spectral density with

$$\left\langle \delta\hat{X}(\Omega)\delta\hat{X}^\dagger(\Omega') \right\rangle = 2\pi S_{\hat{X}}(\Omega)\delta(\Omega - \Omega'). \quad (2.50)$$

2.3 Quantum Correlations

One phenomenon that we can observe in the quantum domain is the existence of non-classical correlations for a system. The production of purely quantum states of light aides us in the experimental observation of these correlations. Here we will show how using a simple tool such as a beamsplitter, and squeezed light will allow us to produce two entangled beams that exert non-classical correlations.

2.3.1 Separability Criterion

There are many criteria that can be used to determine if correlations between quadratures are of quantum origin [Treppe and Fabre, 2005], such as gemellity as shown in [Heidmann *et al.*, 1987], quantum non-demolition measurements, inseparability, and EPR criteria [Reid, 1988]. Of these we will consider the inseparability criterion for our experiment here.

We define two entangled, or inseparable, systems as systems where it is impossible to factor the two states $\hat{\rho}_{i1}$ and $\hat{\rho}_{i2}$ into the independent form

$$\hat{\rho} = \sum_i p_i \hat{\rho}_{i1} \otimes \hat{\rho}_{i2} \quad (2.51)$$

Duan [Duan *et al.*, 2000] and Simon [Simon, 2000] established a criterion which allows us to more easily experimentally determine the separability of two states, using

$$Var(\hat{X}_1 + \hat{X}_2) + Var(\hat{P}_1 - \hat{P}_2) < 2, \quad (2.52)$$

where \hat{X}_i and \hat{P}_i represent the non-commuting conjugate operators of system i . If the variances of our operators \hat{X}_i and \hat{P}_i satisfy Equation 2.52, we can say that the states are inseparable, and thus exhibit quantum correlations between them.

2.3.2 States Incident on a Beamsplitter

With this criterion in place, we can study the properties of two fields incident on a 50/50 beamsplitter.

The reflection and transmission relations for the field give us the following field compositions for the output beams E^+ and E^- , where E_1 and E_2 are two different optical modes

$$E^+ = \frac{E_1 + E_2}{\sqrt{2}} \quad \text{and} \quad E^- = \frac{E_1 - E_2}{\sqrt{2}}. \quad (2.53)$$

We can use the linearization procedure outlined earlier in Section 2.2.5 to derive the fluctuations on the beamsplitter output ports

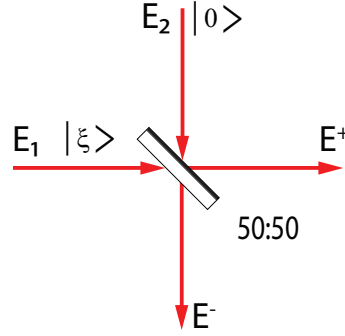


Figure 2.3: A squeezed vacuum state $|\xi\rangle$, and a vacuum state $|0\rangle$ incident on a 50/50 beamsplitter creates two entangled beams at the output.

$$\delta E^+ = \frac{\delta E_1 + \delta E_2}{\sqrt{2}} \quad \text{and} \quad \delta E^- = \frac{\delta E_1 - \delta E_2}{\sqrt{2}}. \quad (2.54)$$

If our fields E_1 and E_2 are not correlated, we can then calculate the variances of our fluctuations using $V_i = \langle \delta E_i^\dagger \delta E_i \rangle$ and obtain the following output port variances

$$V^- = V^+ = \frac{V_1 + V_2}{2}. \quad (2.55)$$

If we now consider the case where we send a squeezed state $|\xi\rangle$ into path 1, and a vacuum state $|0\rangle$ into path 2, such as shown in Figure 2.3, the variance of the vacuum state is given by $V = 1$ for both quadratures, since it is a minimum uncertainty state. However for the squeezed quadrature of our squeezed state, we have a variance where $V_{SQZ} < 1$. By reinserting these quadrature variances into Equation 2.52, we satisfy the criterion for our output beams, thus showing that the two beams are entangled.

$$V^- = V^+ = \frac{1 + V_{SQZ}}{2} < 1. \quad (2.56)$$

Although our beam quadratures exhibit quantum correlations, this inseparability criterion does not satisfy the requirements for EPR entanglement [Reid, 1988] [Reid, 1989]. EPR correlations are a stronger criterion than the inseparability criterion, as all EPR beams are non-separable, whereas not all non-separable beams are EPR entangled. In a system possessing EPR entanglement, the measurements of the quadratures of one beam would provide precise information on the quadratures for the other beam, this appearing to violate the Heisenberg inequality.

2.3.3 Effects of Optical Losses

While we can use the two output ports of a beamsplitter to detect quantum correlations, we can also use the beamsplitter to model optical losses by only detecting light from a single port, and treating the other port's output as lost information.

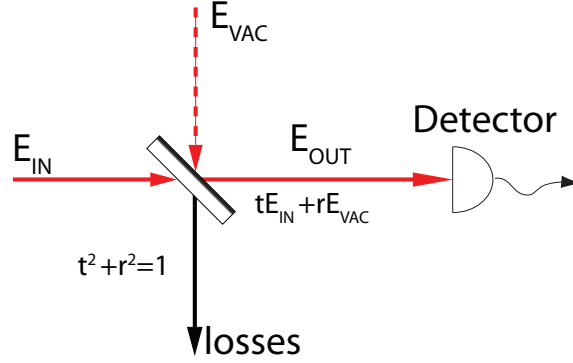


Figure 2.4: We can represent optical losses as a vacuum field being mixed with our optical field on a beamsplitter, with the undetected information lost to the environment.

We can once again consider our beamsplitter with an input beam E_{in} and a vacuum state input on the second port as shown in Figure 2.4, with reflection and transmission amplitudes r and t , where $t^2 + r^2 = 1$. We can express the transmitted portion of this input beam with

$$E_{out} = tE_{in} + rE_{vac}. \quad (2.57)$$

We can also calculate the variances of our beam fluctuations with

$$(\Delta E_{out})^2 = t^2(\Delta E_{in})^2 + r^2(\Delta E_{vac})^2 \quad (2.58)$$

$$V_{out} = t^2V_{in} + r^2 = TV_{in} + (1 - T). \quad (2.59)$$

If we again consider the case where we send in a squeezed state as our input beam, its variance in one quadrature will be less than the vacuum fluctuations. We can see from Equation 2.58 that the beam splitter adds the vacuum fluctuations to our squeezed beam fluctuations by mixing the two beams, and thus our output state contains less squeezing than it originally contained on input. Thus upon detection of our exit beam, if we set $\eta = t^2$ the noise of our squeezed state will be increased to [Fabre *et al.*, 1989]

$$S_-^{out}(\Omega) = S_-^{in}(\Omega)\eta + (1 - \eta). \quad (2.60)$$

Since we can use a beamsplitter to model optical losses, this shows us that losses destroy squeezing by mixing in vacuum fluctuation. Thus, we need to minimize these losses in any process aimed to create or manipulate squeezed states.

Part II

Squeezed Light Production With an OPO

Squeezed Light Production With Nonlinear Optics

Contents

3.1 Nonlinear Optics	28
3.1.1 Propagation Equations	28
3.2 Nonlinear Processes	28
3.2.1 Coupled Wave Equations	29
3.2.2 Second-Harmonic Generation	30
3.2.3 Parametric Down-Conversion	33
3.2.4 Phase Matching	35
3.3 Optical Parametric Amplification and Oscillation	35
3.3.1 Below Threshold Parametric Gain	37
3.3.2 Quantum Noise Below Threshold	38

In order to create a Cesium based atomic memory, we first need to produce a source of squeezed light at 852 nm resonant with the Cesium D_2 line. In this section, we will develop the theory behind the degenerate optical parametric oscillator, and show how its below-threshold operation can lead to the creation of squeezed vacuum states. As we typically create quantum states of light with the aid of materials having nonlinear optical properties, we will begin by studying the classical interaction of an electric field passing through such a material.

3.1 Nonlinear Optics

3.1.1 Propagation Equations

Typically, when a light beam passing through a medium interacts with it, the medium counter-reacts to the light field in a fashion that is linear with the polarization. However, if we can supply intense enough electric fields, we can begin to see effects that are due to a nonlinear polarization response P^{NL} . We can show this by expressing the polarization as a power series in E where $\chi^{(n)}$ represents the n_{th} order susceptibility of the material. When we expand this expression in the form of a power series, we can describe the polarization as a sum of a linear first-order term, and nonlinear higher order terms

$$P = \underbrace{\chi^{(1)}E}_{\text{Linear part}} + \underbrace{\chi^{(2)}E^2 + \chi^{(3)}E^3 + \dots}_{\text{Nonlinear part}} \quad (3.1)$$

We can then explore the interaction of light passing through a nonlinear medium by inserting the nonlinear component of the polarization into the optical wave equation for a series of plane waves [Boyd, 1992]

$$\frac{d^2 E_n}{dz^2} + \frac{1}{c^2} \cdot \frac{\partial^2 E_n}{\partial t^2} = -\frac{1}{c^2} \frac{\partial^2 P_n^{NL}}{\partial t^2}. \quad (3.2)$$

3.2 Nonlinear Processes

If we send two optical beams of frequencies ω_1 and ω_2 into a material having a nonlinear response, we can write the electric field as

$$E(t) = E_1 e^{-i\omega_1 t} + E_2 e^{-i\omega_2 t} + c.c. \quad (3.3)$$

With this expression for the electric field, we can examine the polarization components produced by the second-order polarization

$$P^{(2)} = \chi^{(2)} E^2, \quad (3.4)$$

and we see that we obtain the following components

$$\begin{aligned} P^{(2)} = & \chi^{(2)} [E_1^2 e^{-i2\omega_1 t} + E_2^2 e^{-i2\omega_2 t} + 2E_1 E_2 e^{-i(\omega_1 + \omega_2)t} \\ & + 2E_1 E_2^* e^{-i(\omega_1 - \omega_2)t} + c.c.] + 2\chi^{(2)} [E_1 E_1^* + E_2 E_2^*]. \end{aligned} \quad (3.5)$$

We can express the second-order polarization as the following sum of complex frequency components

$$P^{(2)}(t) = \sum_n P(\omega_n) e^{-i\omega_n t}. \quad (3.6)$$

Due to Equation 3.2, we see that the time-dependent polarization components lead to the production of electromagnetic waves at new frequencies. Using the $\chi^{(2)}$ non-linearity, we are able to produce the following second-order effects with their respective complex amplitudes [Boyd, 1992].

$$P(2\omega_1) = \chi^{(2)} E_1^2 \quad SHG \quad (3.7)$$

$$P(2\omega_2) = \chi^{(2)} E_2^2 \quad SHG \quad (3.8)$$

$$P(\omega_1 + \omega_2) = 2\chi^{(2)} E_1 E_2 \quad SFG \quad (3.9)$$

$$P(\omega_1 - \omega_2) = 2\chi^{(2)} E_1 E_2^* \quad DFG \quad (3.10)$$

$$P(0) = 2\chi^{(2)} (E_1 E_1^* + E_2 E_2^*) \quad OR \quad (3.11)$$

These components show how by using a $\chi^{(2)}$ non-linearity, we can observe the effects of Second Harmonic Generation, Sum Frequency Generation, Difference Frequency Generation (or Parametric Amplification), and Optical Rectification. The processes of second-harmonic generation and parametric amplification play the most central role in our work of generating squeezed states.

3.2.1 Coupled Wave Equations

We can now make the slowly-varying envelope approximation for the field E_i , which assumes that the wavelength of the light is much shorter than the length scale over which the electric field amplitude varies [Fox, 2006]

$$\left| k_i \frac{dE_i}{dz} \right| \gg \left| \frac{d^2 E_i}{dz^2} \right|. \quad (3.12)$$

By using this approximation along with the propagation equation 3.2, we can express the propagation of an electric field through the non-linear medium using the expression [Shen, 1984]

$$\frac{\partial E_i}{\partial z} = \frac{i\omega}{2n_i \epsilon_0 c} P_i^{(NL)} e^{-ik_i z}. \quad (3.13)$$

Once we calculate the appropriate non-linear polarization vector, we can use this expression to derive a system of coupled equations expressing the propagation of several light waves through a non-linear medium.

3.2.2 Second-Harmonic Generation

The first nonlinear process that will prove useful in the generation of squeezed states is Second Harmonic Generation (SHG). We can visualize this process using the photon picture, where two photons of a fundamental frequency combine their energy to produce a single photon of the second-harmonic frequency, as illustrated in Figure 3.1.

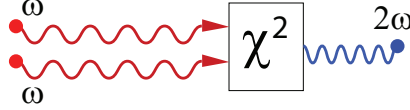


Figure 3.1: Second-harmonic generation uses a second-order nonlinearity to convert two pump photons at the fundamental frequency into one photon at the second-harmonic. Energy and momentum are conserved in the process.

To analyze the SHG process, we will consider the case where there are 2 interacting electric fields that propagate through a nonlinear crystal with a high $\chi^{(2)}$ coefficient - one at the fundamental frequency $E_1(\omega)$ and the other at the second-harmonic $E_2(2\omega)$. We can begin by expressing our beams as a set of infinite plane waves where

$$E_i = A_i e^{ik(\omega_i)z}. \quad (3.14)$$

If we now suppose that we have a beam $E_1(\omega)$ propagating through our crystal, we can use Equation 3.7 and obtain the following expressions for the nonlinear polarization, as shown in [Boyd, 1992]

$$P_1^{(2)} = \epsilon_0 \chi^{(2)} A_2(z) A_1^*(z) e^{i(k_2 - k_1)z} \quad (3.15)$$

$$P_2^{(2)} = \frac{\epsilon_0 \chi^{(2)}}{2} A_1^2(z) e^{2ik_1 z}. \quad (3.16)$$

With these nonlinear polarizations, we can use Equation 3.13 to derive a set of coupled propagation equations for our system [Joffre, 2009]

$$\frac{\partial E_1}{\partial z} = \frac{i\omega_1 \chi^{(2)}}{n_1 c} A_2(z) A_1^*(z) e^{-i\Delta k z} \quad (3.17)$$

$$\frac{\partial E_2}{\partial z} = \frac{i\omega_2 \chi^{(2)}}{2n_2 c} A_1^2(z) e^{i\Delta k z}. \quad (3.18)$$

Chromatic dispersion present in the crystal leads to a *phase mismatch* between the co-propagating waves, which is represented by $\Delta k = 2k_1 - k_2$. These equations can be

solved by assuming that our pump beam E_1 remains constant, and undepleted by its propagation through the crystal, and that the second harmonic amplitude E_2 at the crystal input is zero. These assumptions allow us to obtain the solution [Shen, 1984]

$$A_2(z) = \frac{i\omega_2\chi^{(2)}}{4n_2c}A_1^2\frac{e^{i\Delta kz} - 1}{i\Delta k}. \quad (3.19)$$

This expression shows us the amount of second-harmonic light produced as a function of the input fundamental light.

3.2.2.1 Nonlinear Efficiency

We can quantify the single-pass efficiency of our nonlinear interaction by defining a nonlinear efficiency coefficient E_{NL} , where

$$P_2(z) = E_{NL}P_1^2(0), \quad (3.20)$$

and where $P_1(0)$ is the power of our fundamental beam at the crystal input, and $P_2(z)$ is the power of our second-harmonic at position z in the crystal. If we take the time averaged expression for the power P with the beam having a surface area S , and $P = |I| \cdot S = \frac{1}{2}c\epsilon_0 nS |E|^2$, then we can use Equation 3.19 to obtain

$$E_{NL} = \frac{\omega_2^2\chi^{(2)2}}{8n_1^2n_2\epsilon_0c^3S}z^2\text{sinc}^2\left(\frac{\Delta kz}{2}\right). \quad (3.21)$$

This shows us that the conversion efficiency is periodic in z and depends on the phase mismatch Δk .

3.2.2.2 Cavity-Enhanced SHG

While we see that the propagation through our crystal leads to the production of a field at the second-harmonic frequency, we are working in the regime of weak conversion efficiency. In order to provide a useful amount of light, we need to greatly increase the overall second-harmonic output power. We can accomplish this by placing our crystal inside of an optical cavity that is resonant for the pumping field. We can consider the case of a ring cavity with the crystal placed on the inside, and one mirror serves as an input coupler for our pump beam which has power P_1 , as shown in Figure 3.2.

The mirrors have reflection and transmission coefficients r_i and t_i where $r_i^2 + t_i^2 = R_i + T_i = 1$. We can represent linear losses in the cavity by $L_c = 1 - T_c = 1 - t_c^2$, and the losses due to the nonlinear conversion can be represented by the coefficient Γ , which is expressed in W^{-1} . If we then use the cavity round trip condition to determine the electric field inside the cavity E_c

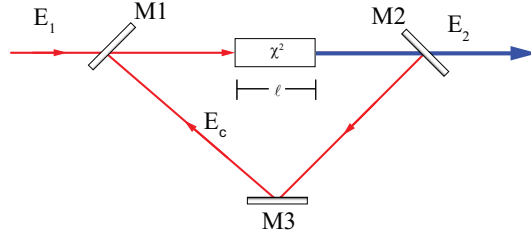


Figure 3.2: Second-harmonic generation enhanced by placing the crystal in a ring cavity resonant for the pumping field.

$$E_c = E_1 \frac{t_1}{1 - r_1 r_2 r_3 t_c \sqrt{1 - \Gamma E_c^2}}, \quad (3.22)$$

we can then calculate the pump power circulating within the cavity [Targat *et al.*, 2005] to be

$$P_c = P_1 \frac{T_1}{[1 - \sqrt{(1 - T_1)(1 - L_c)(1 - \Gamma P_c)}]^2}. \quad (3.23)$$

If we now assume that the reflectivities of our mirrors 2 and 3 are high for the pump, and that we have low cavity losses L_c and our nonlinear losses are only due to the frequency conversion, $\Gamma = E_{NL}$, we can express the circulating power in the simpler form

$$P_C = P_1 \frac{4T_1}{(T_1 + L + E_{NL}P_c)^2}. \quad (3.24)$$

Now that we have an expression for the intracavity power, we can use it to determine the total output power of the second-harmonic generated by the cavity as a function of our input coupler and input power by substituting P_c in for $P_1(0)$ in Equation 3.20. We can make the variable substitution $\lambda = T_1 + L$ and $\rho = 4T_1P_1E_{NL}$ as outlined in [Sørensen, 1998], which gives us the following expression of the second-harmonic output

$$P_2 = \frac{\lambda^2}{9E_{NL}} \left[\left[1 + \frac{27\rho}{2\lambda^3} \left(1 + \sqrt{1 + \frac{4\lambda^3}{27\rho}} \right) \right]^{\frac{1}{6}} - \left[1 + \frac{27\rho}{2\lambda^3} \left(1 + \sqrt{1 + \frac{4\lambda^3}{27\rho}} \right) \right]^{-\frac{1}{6}} \right]^4. \quad (3.25)$$

With this expression, we can determine an optimal transmission for the input coupler for our doubling cavity that we need to maximize our SHG conversion efficiency, as well as estimate a second-harmonic output that we should expect to observe experimentally.

3.2.3 Parametric Down-Conversion

The next non-linear effect that we will analyze is Parametric Down-Conversion, which allows us to directly create squeezed states of light. We can again visualize this effect using photon interactions, as shown in Figure 3.3, as a process which splits a single pump photon into two lower frequency photons in such a way that the energy and momentum are conserved.

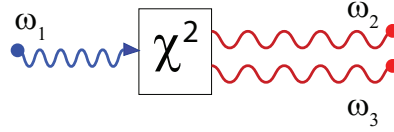


Figure 3.3: Conversion of one second-harmonic pump photon into two lower-frequency photons where $\omega_1 = \omega_2 + \omega_3$, using a χ^2 material

We can begin to understand this effect by first using a classical approach. Here we can consider the case where we have three optical waves of distinct frequencies E_1 , E_2 , and E_3 present in our non-linear crystal, which we will respectively call the *pump*, *signal*, and *idler*. We find that our expression for the non-linear polarization becomes [Boyd, 1992]

$$P_2^{(2)} = \frac{\epsilon_0 \chi^{(2)}}{2} (E_1 E_2^* + E_1 E_3^* + E_2 E_3). \quad (3.26)$$

As with the case of second-harmonic generation, we can insert our expression for the nonlinear polarization into Equation 3.13, and obtain a set of coupled wave equations for our system [Fabre, 1990]

$$\frac{\partial E_1}{\partial z} = \frac{i\omega_1 \chi^{(2)}}{2n_2 c} E_2 E_3 e^{-i\Delta k z} \quad (3.27)$$

$$\frac{\partial E_2}{\partial z} = \frac{i\omega_2 \chi^{(2)}}{2n_2 c} E_1 E_3^* e^{i\Delta k z} \quad (3.28)$$

$$\frac{\partial E_3}{\partial z} = \frac{i\omega_3 \chi^{(2)}}{2n_2 c} E_1 E_2^* e^{i\Delta k z}. \quad (3.29)$$

Here, $\Delta k = k_1 - k_2 - k_3$ represents the phase mismatch between the waves. We can now make a substitution which allows us to express these equations in a simpler form

$$\alpha_i(z) = \sqrt{\frac{n_i c \epsilon_0}{2 \hbar \omega_i}} E_i(z) \quad (3.30)$$

$$\xi = \chi^{(2)} \sqrt{\frac{\hbar \omega_1 \omega_2 \omega_3}{2 \epsilon_0 c^3 n_1 n_2 n_3}}. \quad (3.31)$$

We can remark that the quantity $|\alpha_i(z)|^2 = \frac{n_i c \epsilon_0 |E_i(z)|^2}{2 \hbar \omega_i} = \Phi_i$ gives us the photon flux through the crystal. Carrying out these substitutions gives us the following set of coupled equations

$$\frac{\partial \alpha_1}{\partial z} = i \xi \alpha_2 \alpha_3 e^{-i \Delta k z} \quad (3.32)$$

$$\frac{\partial \alpha_2}{\partial z} = i \xi \alpha_1 \alpha_3^* e^{i \Delta k z} \quad (3.33)$$

$$\frac{\partial \alpha_3}{\partial z} = i \xi \alpha_1 \alpha_2^* e^{i \Delta k z} \quad (3.34)$$

By looking at these equations, we see that the fields α_2 and α_3 change as a function of α_1 , thus we can define a gain coefficient g , where $g = i \xi |\alpha_1|$. If we consider that our pump α_1 has constant intensity, our coupled equations have the solution given by [Joffre, 2009]

$$\alpha_2(z) = \alpha_2(0) \cosh(gz) + \alpha_3^*(0) \sinh(gz) \quad (3.35)$$

$$\alpha_3(z) = \alpha_3(0) \cosh(gz) + \alpha_2^*(0) \sinh(gz). \quad (3.36)$$

If we consider the special case of degenerate beams, where $\omega_2 = \omega_3$, then the solution reduces to

$$\alpha_2(z) = \alpha_2(0) \cosh(gz) + \alpha_2^*(0) \sinh(gz) \quad (3.37)$$

$$= \operatorname{Re}(\alpha_2(0)) e^{gz} + i \operatorname{Im}(\alpha_2(0)) e^{-gz}. \quad (3.38)$$

We now recall that we can decompose the electric field into quadratures, which have a 90° phase difference between them

$$E_2(z) = E_X + i E_P. \quad (3.39)$$

If we inject a signal beam into our crystal while it is being pumped, we see by substituting this decomposition into Equation 3.38 that the quadrature components are amplified and deamplified depending on the beam's phase relation with the pump.

$$E_2(z) = E_X(0)e^{gz} + iE_P(0)e^{-gz}. \quad (3.40)$$

This shows us that our crystal undergoing parametric down-conversion can function as a phase-sensitive amplifier for an injected signal beam.

3.2.4 Phase Matching

For the processes that we have reviewed up until now, the major results have been derived by assuming that the phase matching condition $\Delta k = 0$ holds true. We can interpret this phase matching condition as a requirement that the energy and momentum conservation is conserved between the pump photons and generated photons, such that

$$\omega_1 + \omega_2 = \omega_3 \quad \text{and} \quad k_1 + k_2 = k_3. \quad (3.41)$$

As stated earlier, the dispersion in the crystal introduces the potential for a phase-mismatch between the propagating waves. In order to satisfy the phase-matching condition, one technique is to use birefringent materials which have different refraction indices for their ordinary and extraordinary axes. In this case, it is possible to have a wave propagation in the crystal where their dispersion can compensate for the phase mismatch [Bourzeix, 1995]. There are two main classes of this birefringent phase matching. Type I phase matching involves two waves of the same polarization generating a third wave of the opposite polarization. Type II phase matching involves two waves of different polarizations generating a third wave that may have either polarization.

Type I	e + e → o	o + o → e
Type II	o + e → o	e + o → e

Table 3.1: Birefringent phase matching for ordinary (o) and extraordinary (e) polarizations. Type I phase matching converts two equal polarizations to the opposite polarization. Type II converts two opposite polarizations into one of the input polarizations.

By satisfying the phase-matching condition throughout the beam's propagation in the crystal, we manage to achieve the most efficient transfer of power between the beams.

3.3 Optical Parametric Amplification and Oscillation

Whereas for second-harmonic generation we inserted our crystal in a cavity resonant for the pump, here we can place our crystal in a cavity resonant for the signal and idler

beams that are generated. We can begin analyzing this case by first supposing that a beam passing through a crystal of length l experiences a very small gain. This allows us to linearize the variations of our fields α_i over the length of the crystal with the expression [Fabre *et al.*, 1989]

$$\alpha_i(l) = \alpha_i(0) + l \frac{d\alpha_i}{dz} \quad (3.42)$$

where $\alpha_i(0)$ represents the field amplitude at the entrance of the crystal, $\alpha_i(l)$ represents it at the exit, and α_i at the midpoint $l/2$. We can now place the system in an optical cavity, as shown in Figure 3.4, where the mirrors are transparent for the second-harmonic pump beam, and have reflectivities r_i for our signal and idler beams, where $1 - r_i \approx \frac{T_i}{2} \ll 1$, and after one cavity round-trip, the beams experience a phase shift ϕ_i where $e^{i\phi_i} \approx 1 + i\delta_i$, with $|\delta_i| \ll 2\pi$. Furthermore, we will assume that the pump beam α_1 has a high transmissivity for the mirrors, and remains undepleted in its propagation through the crystal. We can now apply the cavity condition which states that the round-trip phase must equal the original phase

$$\alpha_i(l)r_1r_2e^{i\phi_i} = \alpha_i(0). \quad (3.43)$$

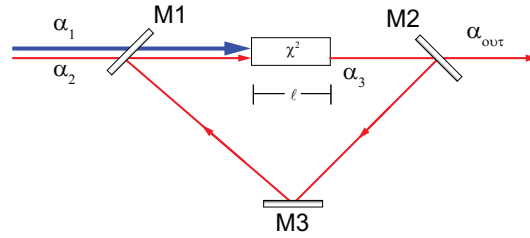


Figure 3.4: We achieve optical parametric amplification by carrying out parametric down-conversion in a cavity resonant with the signal and idler beams. The pump beam is not resonant with the cavity.

By using this condition along with Equations 3.32 and 3.42, we can derive the following relations for the signal and idler beams [Joffe, 2009]

$$i\xi \frac{l}{2} \alpha_1 \alpha_3^* + \alpha_2 (i\delta_2 - \frac{T_2}{2}) = 0 \quad (3.44)$$

$$i\xi \frac{l}{2} \alpha_1 \alpha_2^* + \alpha_3 (i\delta_3 - \frac{T_2}{2}) = 0. \quad (3.45)$$

In order to obtain non-trivial solutions for this system, we must satisfy the relation

$$\delta_2 \delta_3 + \frac{T_2^2}{4} - \xi^2 l^2 |\alpha_1|^2 - \frac{iT_2}{2} (\delta_2 - \delta_3) = 0. \quad (3.46)$$

We can now assume that the signal and idler undergo the same relative phase shifts in their propagation through the cavity, such that $\delta_2 = \delta_3 = \delta$, and we obtain as a solution the following relation [Joffre, 2009]

$$|\alpha_1|^2 = \frac{\delta^2 + T_2^2/4}{\xi^2 l^2}. \quad (3.47)$$

This shows us that there exists a threshold condition in our cavity, and when we supply a pump power greater than this threshold, the cavity begins to oscillate and spontaneously produce down-converted photon pairs. We can describe this threshold as a function of the nonlinear efficiency and total cavity losses L , with the expression

$$P_{th} = \frac{(T + L)^2}{4E_{NL}}. \quad (3.48)$$

3.3.1 Below Threshold Parametric Gain

Given that our nonlinear crystal amplifies or deamplifies our signal sent through the cavity, we can define the parametric gain G for our cavity with the expression

$$G = \frac{P_{signal}^{out}}{P_{signal \text{ w/o pump}}^{out}}, \quad (3.49)$$

where $P_{signal \text{ w/o pump}}^{out}$ is the power of our injected signal beam that is output from the OPO when no pump is present, and P_{signal}^{out} is the amplified output power of our signal beam when the pump beam is present and applying a gain. We can also define a pump parameter σ , where

$$\sigma = \sqrt{\frac{P_{pump}}{P_{th}}}. \quad (3.50)$$

To evaluate this gain, we first determine the baseline amount of light power produced for our cavity output when we just send in a signal beam. We can assume that we have a low nonlinear efficiency E_{NL} , and by using Equation 3.24 which gives us an expression for the power circulating in the cavity, we obtain

$$P_S^{out} = \frac{4T_1 T_2}{(T_1 + L)^2} P_S^{in}. \quad (3.51)$$

We can then obtain an expression for the signal power when the pump is present, where θ is the relative phase difference between the pump and the signal beams [Ortalo, 2009]

$$P_S^{out} = \frac{4T_1 T_2}{(T_1 + L)^2} \frac{1}{1 + \sigma^2 - 2\sigma \cos(\theta)} P_S^{in}. \quad (3.52)$$

When we reinsert these equations into Equation 3.49, we obtain the following expression for the parametric gain of the cavity as a function of the relative phase shift θ

$$G = \frac{1}{1 + \sigma^2 - 2\sigma\cos(\theta)}. \quad (3.53)$$

As our relative phase shift can assume a maximum difference of $\theta = \pi$, we see that the parametric gain can take on maximum and minimum values given by

$$G_{max} = \frac{1}{(1 - \sigma)^2} \quad \text{and} \quad G_{min} = \frac{1}{(1 + \sigma)^2}. \quad (3.54)$$

As we increase our pump power and approach the threshold sending $\sigma \rightarrow 1$, we see in Figure 3.5 that the maximum gain diverges at the threshold, and the minimum gain approaches the value $\frac{1}{4}$.

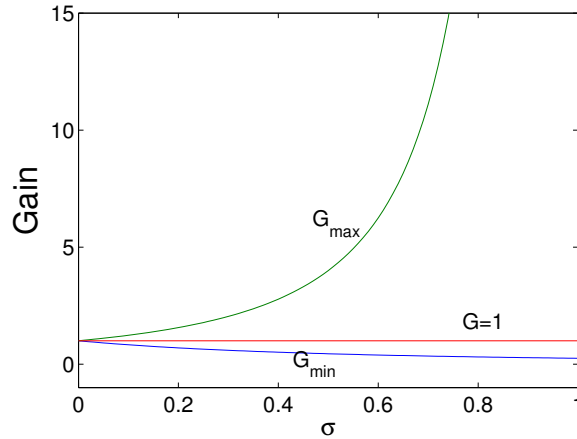


Figure 3.5: Parametric amplification and deamplification as the pump power approaches threshold. The maximum gain diverges as we approach the threshold, while the deamplification minimum approaches $1/4$.

3.3.2 Quantum Noise Below Threshold

Up until now, we have analyzed the OPO in the classical domain. Now we will show how an OPO pumped below threshold will produce squeezed states. We can begin by describing the parametric process with the following Hamiltonian

$$H = E(\hat{a}^{\dagger 2} - \hat{a}^2), \quad (3.55)$$

where E is a complex function of the pump intensity and crystal nonlinearity, and \hat{a} and \hat{a}^\dagger are the annihilation and creation operators. We can then express the dynamic equations of the OPO as [Lam, 1998]

$$\frac{d\hat{a}}{dt} = E\hat{a}^\dagger - \gamma\hat{a} + \sqrt{2\gamma_b}\delta A_b + \sqrt{2\gamma_l}\delta A_l + \sqrt{2\gamma_c}\delta A_c \quad (3.56)$$

$$\frac{d\hat{a}^\dagger}{dt} = E^*\hat{a} - \gamma\hat{a}^\dagger + \sqrt{2\gamma_b}\delta A_b^\dagger + \sqrt{2\gamma_l}\delta A_l^\dagger + \sqrt{2\gamma_c}\delta A_c^\dagger, \quad (3.57)$$

where $\gamma_i = 1 - r_i$, and r_i represents the input and output mirror reflectivities, γ_b and γ_c are the decay rates due to the input and output mirror reflectivities, γ_l the intracavity losses, and $\gamma = \gamma_b + \gamma_c + \gamma_l$. A_b represents our signal beam, where δA_c and δA_l represent the vacuum fluctuations associated with the losses. We can now take the Fourier transform of these equations and use the expressions for the quadrature fluctuations

$$\delta X = \hat{a} + \hat{a}^\dagger \quad \text{and} \quad \delta Y = i(\hat{a} - \hat{a}^\dagger), \quad (3.58)$$

which give us the following set of expressions

$$i\Omega\delta\hat{X} = (Re(E) - \gamma)\delta\hat{X} + Im(E)\delta\hat{Y} + \sqrt{2\gamma_b}\delta\hat{X}_b + \sqrt{2\gamma_l}\delta\hat{X}_l + \sqrt{2\gamma_c}\delta\hat{X}_c \quad (3.59)$$

$$i\Omega\delta\hat{Y} = Im(E)\delta\hat{X} + (Re(E) + \gamma)\delta\hat{Y} + \sqrt{2\gamma_b}\delta\hat{Y}_b + \sqrt{2\gamma_l}\delta\hat{Y}_l + \sqrt{2\gamma_c}\delta\hat{Y}_c \quad (3.60)$$

where Ω represents the detection frequency. We can then calculate the noise spectral density of our noise quadratures using

$$S^+(\Omega) = \langle \delta\hat{X}_1(\Omega)\delta\hat{X}_1^\dagger(\Omega) \rangle \quad (3.61)$$

$$S^-(\Omega) = \langle \delta\hat{Y}_1(\Omega)\delta\hat{Y}_1^\dagger(\Omega) \rangle \quad (3.62)$$

where $\delta X_1^+(\Omega) = \sqrt{2\gamma_c}X^+ - \delta X_c^+(\Omega)$ [Lam, 1998]. We thus obtain the following expressions for the quadrature noise variances on the OPO output

$$S^+(\Omega) = 1 + \frac{T}{T + L} \frac{4\sigma}{\left(\frac{\Omega}{\gamma}\right)^2 + (1 - \sigma)^2} \quad (3.63)$$

$$S^-(\Omega) = 1 - \frac{T}{T + L} \frac{4\sigma}{\left(\frac{\Omega}{\gamma}\right)^2 + (1 - \sigma)^2} \quad (3.64)$$

where σ is given by Equation 3.50, and $\frac{\Omega}{\gamma}$ is the detection frequency normalized to the cavity bandwidth. As we have asymmetric variances in our state's output fluctuations with the variance in one of the quadratures falling below the standard quantum limit, the OPO produces squeezed states when pumped below threshold. Figure 3.6 shows a plot of this behavior for a cavity with a $T=7\%$ output coupler and 2% internal losses.

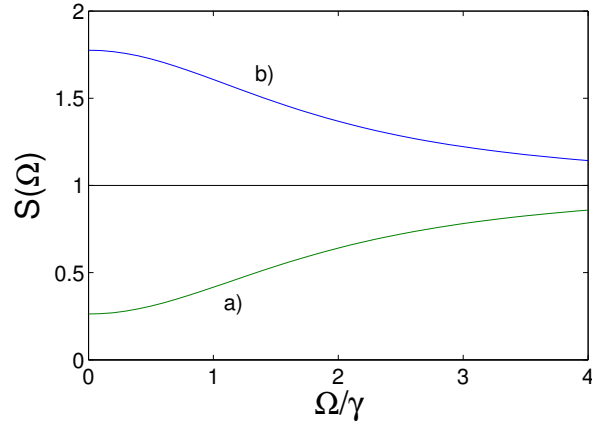


Figure 3.6: Quadrature noise a) amplification and b) deamplification for an OPO using a $T=7\%$ output coupler, $L=2\%$ intracavity losses, at 90% of threshold with a perfect detection efficiency.

In the next section, we will look at the experimental setup that we used to produce these states.

Experimental Setup of the OPO

Contents

4.1	Optical Setup	42
4.1.1	Laser Source	42
4.1.2	OPO Table	43
4.2	Nonlinear Crystal	45
4.2.1	Selection Characteristics	45
4.2.2	Implementation Parameters	48
4.3	Doubling Cavity	50
4.3.1	Intracavity Losses	51
4.3.2	Tilt Locking	51
4.3.3	Second-Harmonic Generation Results	53
4.4	OPO Cavity	56
4.4.1	Cavity Locking	57
4.4.2	Pump Matching	59
4.4.3	Classical Observations	60

In the preceding chapters, we developed the theory of optical interactions in non-linear media, and showed how the usage of parametric down-conversion can lead to the deamplification of quadrature noise, thereby producing squeezed states. In this chapter, we will discuss our experimental development of a doubly-resonant degenerate OPO, which allowed us to create squeezed light through its below-threshold operation.

4.1 Optical Setup

4.1.1 Laser Source

The laser we used to run this experiment is a Titanium-Sapphire Matisse TR Sirah laser, which is optically pumped by a Coherent Verdi V-18 laser with 10 W of 532 nm light. Pumping at this power provides us with 2.3 W of output power from the Matisse at 852 nm. We will discuss the laser setup in more detail in Appendix A.

When the light exits the laser we divide it into several beams. The primary beam of around 1.5 W is used to power the OPO and cold atom experiments. A second beam of around 40 mW is sent to a second part of the table where it is further subdivided. We inject one of these subdivided beams into a reference cavity, which we use daily to verify the alignment of the laser. A second beam is injected into another cavity, which we use to lock the laser on the resonant atomic transition. A third beam is sent into a wavemeter which allows us to monitor the wavelength in real time. We send a fourth beam to another optical table, where it serves as a frequency reference for phase-locking a second diode laser.

4.1.1.1 Optical Fibers

Although the laser source generates our light on one table, the light is used to power experiments which are spread across several other optical tables. In order to transfer this light, we use single-mode polarization-maintaining fibers purchased from OzOptics (PMJ model). The polarization-maintaining property of these fibers allows us to assure the linearity in the polarization of the beams output from the fibers.

Preserving this linear polarization is extremely important when using polarization-maintaining fibers. This is due to the fact that any polarization fluctuations that occur within the fibers will transform into power fluctuations once the beam passes through any polarizing optic. Random power fluctuations are destructive to the experiments, as they prevent us from obtaining a fixed measurement reference point, such as when we measure the shot noise in the squeezed light measurement.

There exists an alignment technique which allows us to assure that we can preserve the polarization linearity in our beams as much as possible. This requires that the polarization of our input beam be properly aligned with the core of the fiber [Aalto *et al.*, 2003]. To carry out this alignment, we glued a PBS cube to a small optical rotation mount, and placed the entire ensemble directly in front of the fiber coupler entrance, as shown in Figure 4.1. Using a cube assures that the polarization in the beam transmitted from the cube's output port is linear, and by placing it just at the fiber input, we assure that the beam polarization has not undergone any randomization due to reflections from mirrors. Finally, the rotation mount allows us to precisely adjust the polarization angle until it is properly aligned with the fiber core.

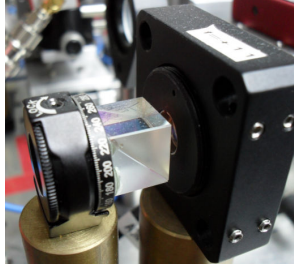


Figure 4.1: PBS Cube mounted to a rotation mount allows us to align the linear polarization to the fiber optic core.

In order to verify our alignment with the axis, we optimize the extinction ratio ζ of the output beam's polarization while subjecting the fiber to stress. We measure this extinction ratio by mounting a Glan polarizer to a rotating optical mount, and placing it at the output of the fiber. While stressing the fiber, we measure P_{max} as the power transmitted through the polarizer when it is aligned with the output polarization, and P_{min} as the power transmitted when the polarizer is turned to block the light transmission. We then calculate the extinction ratio with

$$\zeta = -10 \log \frac{P_{min}}{P_{max}}. \quad (4.1)$$

Turning the rotation mount at the input changes the output extinction ratio. Once we manage to maximize this extinction ratio, this indicates to us that we have obtained the best input polarization alignment. Using this method, we typically obtain extinction ratios ranging from 24 dB to 27 dB, approaching the specification limits for our fibers. Thus, further optimization is limited by the quality of the fiber. By using this method, we obtain a stable beam polarization at the fiber output, which is usable for the rest of the experiment.

4.1.2 OPO Table

Figure 4.1.2 shows a layout of the OPO table. The light prepared by the Matisse arrives on the table, where it is divided and sent towards the 3 main components of the table: the two optical cavities, and the homodyne detector. We typically couple 975 mW of light from the Matisse into the optical fibers and obtain 585 mW at the output on the table. Of this amount, we send 500 mW into the doubling cavity where we carry out second-harmonic generation, 10 mW is injected into the OPO which serves as a locking beam, and 16 mW continues on to the homodyne detector where it functions as a local oscillator. We also fraction off a portion which we call the seed beam, which is used as an injection beam for the OPO. This is primarily used as an aid to check for cavity alignment.

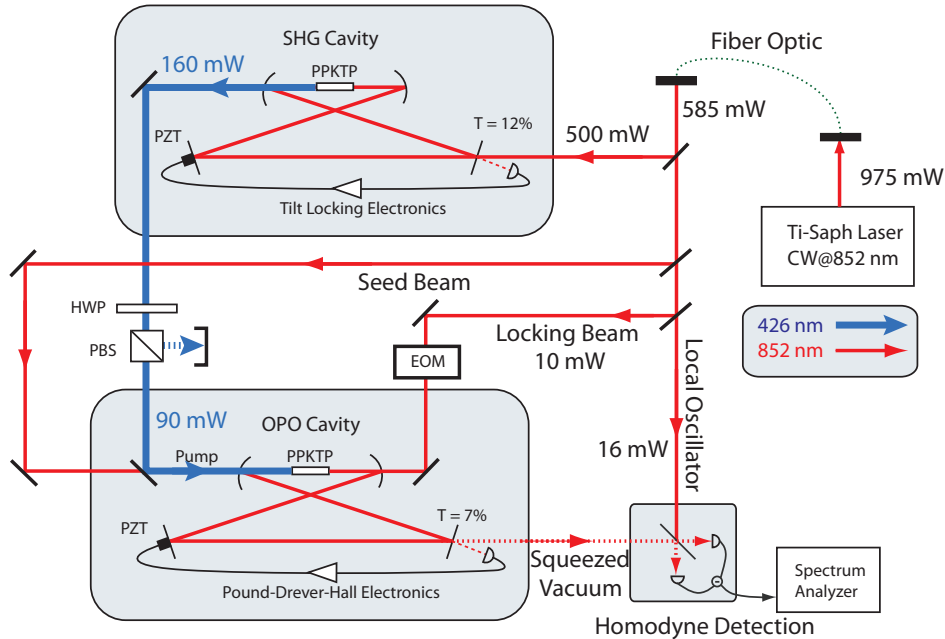


Figure 4.2: Block diagram of the main OPO components: The Matisse laser connected by a fiber optic, SHG and OPO cavities, and homodyne detector. 500 mW of 852 nm input into the doubler produces 160 mW of 426 nm light. 10 mW is used for the OPO lock beam, and 16 mW is sent into the local oscillator.

4.1.2.1 Cavity Generalities

The two optical cavities have many characteristics in common. Both contain a PPKTP nonlinear crystal, both use a bow-tie design, and both use electronic feedback systems to lock them at resonance. Each cavity is mounted on a brass breadboard which provides it with additional stability, and is housed inside of a plexiglass case which protects it from dust and air fluctuations.

We have selected the bow-tie design for these cavities for several practical reasons. We first preferred a ring cavity to a linear one, as the ring cavity would prevent the buildup of standing waves and thus allow us to avoid problems arising from interference effects [Courtilot, 2003]. As the large angles in a ring cavity typically introduce astigmatism into its beam, we chose a bow-tie design which would allow us to minimize the angles of reflection [Lam, 1998]. We also selected smaller mirrors of 1/2" diameter, which allowed us to further reduce the angles.

The mirrors chosen were purchased from VLOC, and were selected to have a high transparency for the blue second-harmonic light, which was at $\lambda = 426$ nm. Excluding the cavity couplers, the mirrors have high reflectivities for the red light at $\lambda = 852$ nm. Experimental measurements have shown us that they offer a reflectivity of $R \approx 7\%$ for

the blue light, and $R > 99.98\% \pm 0.01\%$ for the red light.

4.2 Nonlinear Crystal

We decided to use Periodically-Poled Potassium Titanyl Phosphate (PPKTP) as the nonlinear crystal inside our cavities. These were purchased from Raicol Crystals in Israel with dimensions of 1 mm x 2 mm x 20 mm, and were coated with an anti-reflection treatment of $R < 0.2\%$ for light at 852 nm and 426 nm.

4.2.1 Selection Characteristics

Historically, many types of crystals have been used for second-harmonic generation and squeezed light production. The most important criterion in selecting a crystal for nonlinear effects is assuring that the phase-matching condition can be satisfied for the experimental application. Our decision to select PPKTP as opposed to others was based on the following several factors, that suggested it would provide the most promising nonlinear response for our SHG and squeezed light production.

4.2.1.1 Quasi-Phase Matching

In Section 3.2.4, we discussed how the phase-matching of the optical waves in a non-linear medium leads to a higher overall efficiency in our nonlinear processes. The phase-matching condition is difficult to satisfy in practice. For waves propagating through a nonlinear crystal, there exists a finite *coherence length* L_c for the nonlinear interaction. Beyond this length, the waves undergo a phase inversion and the overall efficiency of our process begins to decrease. If we consider the case of second-harmonic generation, the pump wave produces the second-harmonic with increasing amplitude, supplying energy to the second-harmonic beam up until the coherence length. After this point, the energy then begins to flow back from the second-harmonic into the pump, until the waves have undergone a 2π phase inversion and the process restarts

$$L_c = \frac{\pi}{\Delta k}. \quad (4.2)$$

In order to prevent this effect from limiting our overall output efficiency, we can use the quasi-phase matching technique which will allow us to have an overall better phase-matching throughout the length of our material. This technique involves reversing the sign of the $\chi^{(2)}$ nonlinearity after every multiple number of coherence lengths. This will prevent the phase inversion from taking place, and will bring us closer to the ideal condition of a perfect phase-matching throughout the entire crystal length. Figure 4.3 illustrates the effects of applying this technique to second-harmonic generation.

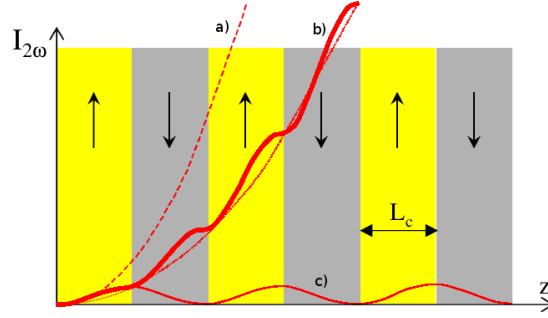


Figure 4.3: Quasi-phase matching in a nonlinear crystal for second-harmonic generation. a) Second-harmonic output with ideal phase matching. b) Output in the case of quasi-phase matching. c) Output when the phase-matching periodically reverses.

4.2.1.2 Periodic-Poling

In order to attain quasi-phase matching practically, the technique of periodic-poling is applied to the crystals. This involves applying electrodes to the crystal at certain intervals to allow a strong electric field to reverse the ferroelectric domains. We refer to these periods as the poling period. We can determine the poling period needed for our crystal by first beginning with the Sellmeier equations to determine the refractive indices at our wavelengths. We can use the expression given in [Vanherzeele *et al.*, 1988]

$$n_z^2 = A + \frac{B}{1 - \left(\frac{C}{\lambda}\right)^2} - D\lambda^2, \quad (4.3)$$

where $A=2.3136$, $B=1.00012$, $C=0.23831$, and $D=0.01679$. Applying this expression to our wavelengths, we find the indices of refraction $n_{426nm} = 1.9406$ and $n_{852nm} = 1.8401$ for KTP. We can then use the phase-matching condition to determine the coherence length over which we need to apply a poling in order to compensate for the phase mismatch

$$\Delta k = k_{426} - 2k_{852} = \frac{2\pi}{426nm}(n_{426} - n_{852}) = \frac{2\pi}{l_{poling}}. \quad (4.4)$$

Carrying out this calculation indicates that we need a poling period of $4.2 \mu m$ to compensate for the phase mismatch. For our experiment, we used crystals with a poling period of $4.15 \mu m$, where the discrepancy is likely due to our specific requests for a specific phase-matching temperature.

4.2.1.3 Phase-Matching Angle

Another consideration needed to obtain optimal phase-matching is that the angle needed to satisfy the phase-matching condition can vary depending on the crystal.

Some crystals require a *critical phase-matching*, which means that the beams are only phase-matched for a certain angle. This would force us to have a precise angular control over the crystal and beam alignment. A preferable situation is to use noncritical phase-matching with a crystal such as PPKTP, which removes this restriction.

4.2.1.4 Nonlinear Coefficient

PPKTP has one of the highest nonlinear coefficients available, which has been measured to be around $d_{33} = 14.9 \text{ pm/V}$ [Arie *et al.*, 1997]. Due to this high nonlinearity, we can expect a more efficient usage of our pump beams, and thus a higher second-harmonic generation efficiency, and lower OPO threshold.

4.2.1.5 Phase-Matching Temperature

Efficient nonlinear interactions can only take place when we satisfy the phase-matching condition. However, this condition is not satisfied for all wavelengths simultaneously, but only for a fixed wavelength at a given temperature. We thus need to ensure that we can achieve phase-matching for 852 nm light at an experimentally accessible temperature. Some crystals such as KNbO_3 allow efficient phase-matching at colder temperatures, but this adds complexity to the experiment in that it requires a cryostat and can lead to condensation on the crystal surface, thus complicating the overall setup [Biaggio *et al.*, 1992]. PPKTP allows us to use temperatures closer to room temperature, we lets us more easily exert a fine control over the temperature regulation.

4.2.1.6 Damage Threshold

When the crystal is used inside of a cavity to obtain second-harmonic generation, the large intracavity intensity buildup of our fundamental pump beam can surpass the damage thresholds of some crystals inducing optical degradation. This degradation can then translate into optical losses, which lowers our overall conversion efficiency. The damage threshold for PPKTP was rated by the manufacturer at around $1.5\text{-}2 \text{ MW/cm}^2$, which is relatively high compared to most crystals. This thus allows for higher pump powers, and as a result, a higher second-harmonic power output.

4.2.1.7 Blue Light Induced Losses

Another harmful effect that can be potentially observed is Blue Light Induced Infrared Absorption (BLIIRA) [Mabuchi *et al.*, 1994]. This takes place in crystals such as KbNO_3 when the presence of a second-harmonic beam in the crystal causes it to increase its absorption of waves at the fundamental wavelength. This effect can be translated into an optical loss for our fundamental, which has destructive effects when

producing squeezed light in the OPO. At the time of our crystal selection, no observations of BLIIRA had been reported during PPKTP usage.

4.2.2 Implementation Parameters

For the particular crystals that we used in our experiment, they satisfied a Type I phase-matching condition. In order to best adapt the crystals to our experiment and build a predictive model of their nonlinear behavior, we also needed to consider effects such as their optical losses, temperature control methods, and how we focused our beams inside of them.

4.2.2.1 Optical Losses

For our PPKTP crystals, we measured single pass absorption rate of around $2\% \pm 0.5\%$ for light at 852 nm. These losses render this crystal less than ideal for producing squeezed states at 852 nm, but they are not so elevated as to prevent the OPO operation. PPKTP is also known to have higher absorption for wavelengths below 500 nm due to its lower UV bandgap energy [Targat *et al.*, 2005], and our crystals were subject to this effect, having absorption rates 10%/cm for 426 nm light [Hansson *et al.*, 2000]. This has the effect of heating the crystal when we pump the OPO with high 426 nm pump powers. As a result, our alignment and phase-matching conditions can change at intense pump powers due to thermal effects in the crystal.

4.2.2.2 Temperature Control

We sought to maintain a temperature stability of our crystal of 10 mK. We thus inserted each crystal into copper a block which acted as an oven, and the contact points were covered in Arctic Silver thermal interface compound. The oven itself was mounted on a peltier, and another thermal interface compound was applied to the interface between the peltier and the oven. The temperatures were controlled to within 0.01°C using a homemade PID controller for the doubler, and an Innolight temperature controller for the OPO. We were able to continuously monitor the temperatures by using a thermistance which was buried inside of the oven for each crystal. We noticed that fluctuating air currents changed the temperature greatly, so we enclosed the entire cavity inside a plexiglass box in order to have a more stable atmospheric environment.

4.2.2.3 Optimal Focusing

Another important factor to determine was how to optimally focus the light into the crystals to obtain the highest nonlinear efficiency [Bourzeix, 1995]. If we recall our expression for the nonlinear efficiency given by Equation 3.21, and assume the perfect phase-matching condition $\Delta k = 0$, we can see that the efficiency is inversely

proportional to the interaction area S of our beam. This indicates to us that we should focus our beam as tightly as possible in order to obtain the highest interaction efficiency

$$E_{NL} = \frac{\omega_2^2 \chi^{(2)2}}{8n_1^2 n_2 \epsilon_0 c^3} \frac{z^2}{S}. \quad (4.5)$$

If we consider the case of second-harmonic generation in a cavity, a tighter focus will deliver a much larger beam intensity to the crystal, likely surpassing its damage threshold and destroying it. Thus, an extremely tight beam focus presents practical problems. A loose focusing does not offer solutions either however, as it causes our nonlinear-efficiency to decrease.

An additional factor arises due to the fact that when we derived our equations of motion for the nonlinear interaction, we made the simplification that our beams consisted of plane waves. In practice, the beams circulating in the cavity and interacting with the crystal are highly focused gaussian modes, which changes our estimation for the nonlinear efficiency.

As a result, we see that a more refined model is needed which offers an optimization between loose and tight focusing. Boyd and Kleinman have shown a method for finding this optimal focus [Boyd and Kleinman, 1968]. They suggest that when considering gaussian beams, we replace the factor z^2/S in Equation 4.5 by the expression

$$\frac{kl}{\pi} h_m(B, \xi), \quad (4.6)$$

where l is the length of our crystal, B represents a function linked to double refraction, and h_m is a function that depends on the phase-matching, beam waist position, and focusing strength ξ . The authors have numerically determined that h_m reaches a maximum of $h_m = 1.068$ when the focusing parameter is optimized at $\xi_{opt} = 2.84$. The focusing parameter is defined as $\xi \equiv \frac{l}{b}$, where b is the confocal parameter of our beam, such that $b = \frac{2\pi\omega_0^2}{\lambda}$. If we set the crystal length as our interaction length l , this definition provides us with a recipe for finding the optimal waist size for focusing

$$\omega_{opt} = \sqrt{\frac{l\lambda}{2n\pi\xi_{opt}}}. \quad (4.7)$$

When we substitute into Equation 4.7 the particular values for our crystal, $n = 1.84$, $\lambda = 852nm$, and $l = 20mm$, we find that our optimal waist size according to Boyd and Kleinman is

$$w_{opt} = 22.7\mu m. \quad (4.8)$$

4.3 Doubling Cavity

The Boyd and Kleinman optimum that we have just derived fixes an optimum focusing size for both the doubling cavity, and the OPO. However, due to the different functioning modes of the two cavities, we cannot simply use the result as it is. We first tried to operate the doubler with a tightly focused beam, however we noticed that it was subject to thermal lensing effects and bistability effects. These effects not only subtly altered our intended efficiency, but also weakened the cavity lock stability, which further lowered the overall conversion efficiency. We thus found it necessary to adjust the cavity geometry by optimizing the conversion inefficiency directly. The best configuration that we found produced a waist in the crystal of $w_0 = 60\mu\text{m}$

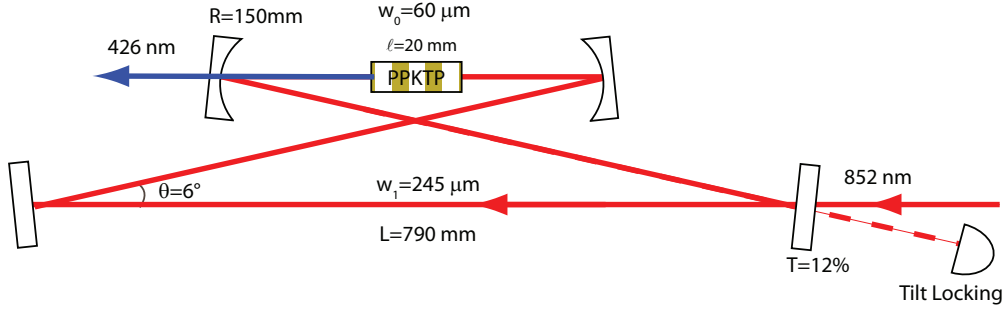


Figure 4.4: Geometry of our bow-tie doubling cavity used for second-harmonic generation. A waist of $w_0 = 60\mu\text{m}$ is produced in the center of a $l = 20\text{mm}$ PPKTP crystal by using mirrors with a radius of curvature of $R = 150\text{mm}$. A $T=12\%$ plane mirror serves as the input coupler.

The doubling cavity has the bow-tie design as shown in Figure 4.4, with angles of reflection of 3° and a total length of $l = 790\text{mm}$, corresponding to a free spectral range of 380 MHz. The two curved mirrors each have a radius of curvature of $R = 150\text{mm}$, with the PPKTP crystals mounted between them. The bow-tie geometry produces two optical waists in the cavity, and thus the second one had a size of $w_1 = 245\mu\text{m}$. We decided to use an input coupler of 12% in order to optimize second-harmonic output, according to the following expression, where $L = 0.02$, and we have a measured nonlinear efficiency of $E_{NL} = 0.02$, and $P_1 = 0.6$ [Targat *et al.*, 2005]

$$T_{opt} = \frac{L}{2} + \sqrt{\left(\frac{L}{2}\right)^2 + E_{NL}P_1}. \quad (4.9)$$

4.3.1 Intracavity Losses

We took several measures of the cavity finesse by measuring the ratio between the free spectral range (FSR) and the TEM_{00} mode peak width (FWHM) when scanning the cavity

$$\mathcal{F} = \frac{FSR}{FWHM}. \quad (4.10)$$

With this method, we obtained a finesse of $\mathcal{F} = 46 \pm 2$, which corresponds to 14% + 1% cavity losses. This confirms our single pass measurements of the crystal's 2% absorption rate, given our cavity's T=12% input coupler.

4.3.2 Tilt Locking

In many optics experiments, cavity locking systems are employed which keep the cavity length stable so that it remains fixed at resonance. These generally work by optically measuring the difference between the carrier frequency of beam and the frequency of the cavity mode, and creating an error signal from this difference. This signal is then sent into a feedback controller which adjusts the cavity length by displacing a cavity mirror loaded onto a piezo. For our doubler cavity, we use the Tilt Locking system [Shaddock *et al.*, 1999], [Shaddock, 2001] in order to create our error signal.

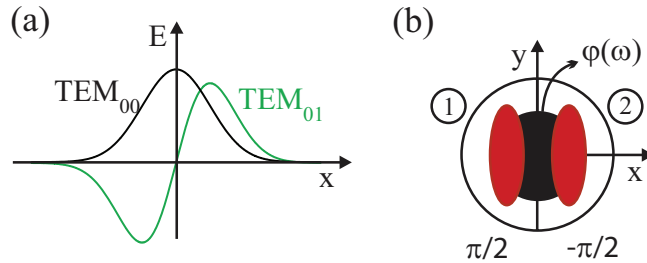


Figure 4.5: Tilt locking: a) The interference between the TEM_{00} and TEM_{01} modes results in different intensities on the photodiode surface. b) The interference is detected on a split photodetector, whose sections we subtract to obtain the error signal.

Tilt locking works by using spatial-mode interference to measure the length changes of the cavity. This works by injecting a TEM_{00} mode beam into the cavity, and then slightly disaligning it so that the input beam excites a TEM_{01} mode. Part of the reflected beam is then sent to a photodiode which is split into two sections, which we then subtract to obtain the difference photocurrent. Each section receives half of the TEM_{00} mode, and one of the lobes for the TEM_{01} mode as shown in Figure 4.5. The electric field of the TEM_{00} mode has a constant phase $\phi(\omega)$ across the detector surface

and serves as a phase reference, whereas the lobes of the TEM_{01} mode have a phase difference of π across the detector surface.

This setup can create an error signal by using changes in the cavity length to detect relative phase shifts between the modes. When the cavity is at resonance, the two modes have zero relative phase shift, and when they interfere, the photodetector surface detects equal intensity on each of the two sections. When we then subtract the two photocurrents from these sections, we obtain a zero-valued DC error signal. When the cavity mirrors are displaced from resonance, this induces a relative phase shift between the two modes, and the interference no longer produces equal intensity on both detector sections. This can thus create a positive or negative DC error signal depending on the mirror displacement direction. Tilt locking has a bandwidth coverage similar to the commonly used Pound-Drever-Hall scheme, and thus yields similar locking performance [Shaddock *et al.*, 1999].

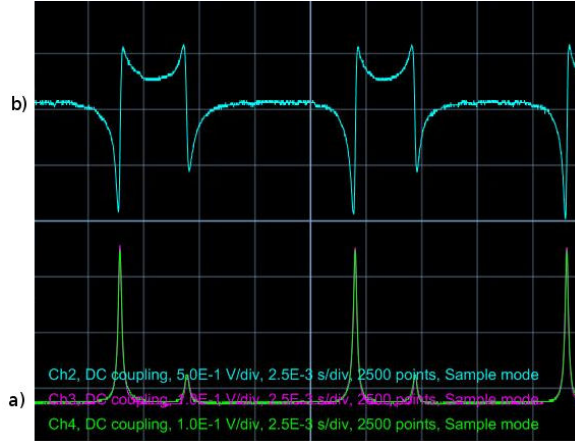


Figure 4.6: a) TEM_{00} and TEM_{01} peaks from a cavity scan that are used to create the error signal. The TEM_{01} peak has about 7% of the amplitude of the TEM_{00} peak. b) Experimental error signal generated with the tilt locking method, used to lock the doubling cavity.

For our implementation of this scheme, we purchased Advanced Photonix (SD 197-23-21-041) photodiodes from digikey.com. We selected this model for several of its technical characteristics which we found to be important when implementing a tilt lock. The photodiode has a 4.98 mm^2 area, which means that it will have a higher precision when detecting the displacement of a smaller sized $200 \text{ }\mu\text{m}$ beam. The gap between the two sections of the photodiode acts as a blind spot which cannot measure the beam, thus its preferable that it be as small as possible. For these photodiodes, the gap is only $30 \text{ }\mu\text{m}$ in width. It also has very low noise characteristics which improves the signal-to-noise ratio of our detection. Finally, it has a 75MHz bandwidth, which would allow us to more easily maintain a high detection bandwidth when amplifying

our signal with a strong gain. We developed a photodiode amplifier to use with this detector, whose circuit is shown in Appendix C, Figure 8.7.

For the beam itself, we then attenuated power from the reflected beam to about 1 mW, sent it onto the photodiode, and disaligned our beam such that the TEM_{01} mode contained 7% of the intensity of the TEM_{00} mode when viewing the scanned cavity in an oscilloscope. This setup allowed us to obtain the error signal shown in Figure 4.6 for the cavity.

We then sent the error signal to a homemade proportional-integrating controller whose circuit is shown in Appendix C, Figure 8.9, which controlled the piezo and closed the feedback loop. When there were no external disturbances in the room, we managed to obtain stable cavity locks with this setup which easily kept the cavity output at its peak for several hours.

4.3.3 Second-Harmonic Generation Results

4.3.3.1 Nonlinear Efficiency

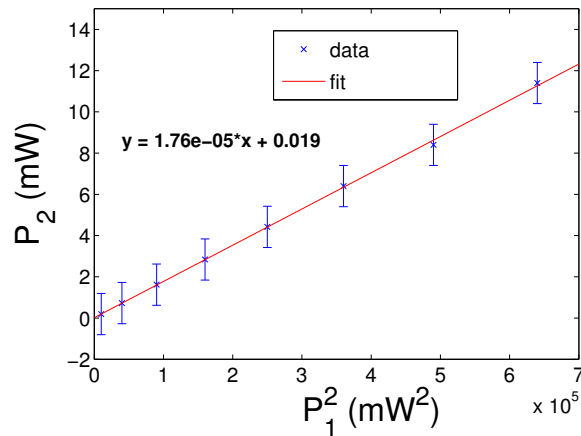


Figure 4.7: Nonlinear efficiency of 1.76%/W derived from linear fit of P_2 vs P_1^2 using Equation 3.20. We estimate a systematic error of 10 mW on the output power measurement due to the precision of the power meter.

With the cavity parameters and locking mechanism selected, we next sought to test the nonlinear aspects of the doubling cavity. The first useful measurement to obtain was a measurement for the nonlinear efficiency. This would allow us to obtain a quantitative estimation of how well the beam was focused onto the crystal. In order to carry out this measurement, we removed the input coupler from the cavity which allowed us to send in much larger light intensities. We then sent infrared light into the mounted crystal in a single passage so that the light would maintain the same

cavity mode focalization as it would have during its normal functioning. We then measured the blue power output as a function of the square of the red power input, which allowed us to trace a line shown in Figure 4.7 whose slope provided us with the nonlinear efficiency value, according to Equation 3.20. This resulted in a measured value of [Villa *et al.*, 2007]

$$E_{NL} = 1.76\%/W \pm 0.02\%/W. \quad (4.11)$$

4.3.3.2 Phase-Matching Temperature

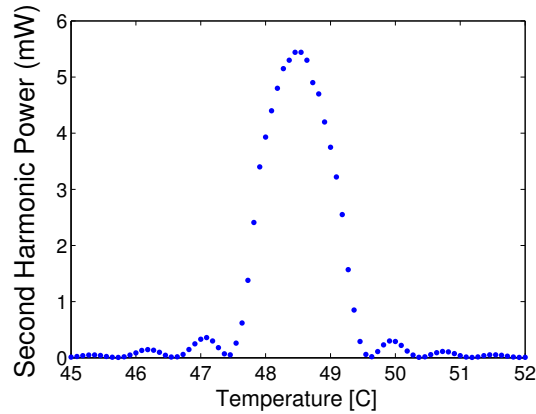


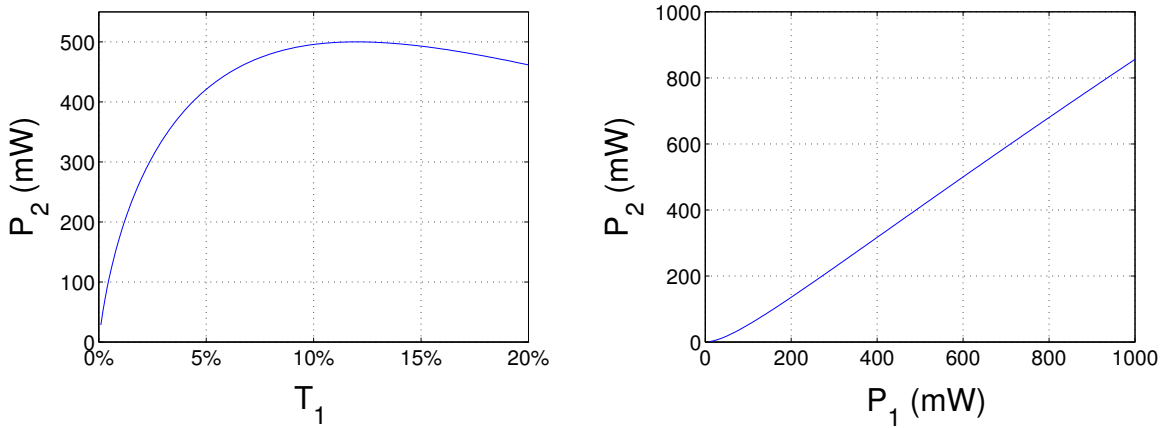
Figure 4.8: Second-harmonic power output vs. crystal temperature shows a phase matching temperature around 48.3°C, with a 1.5°C range.

The next step necessary in order to optimize the doubler output was to find the optimal phase-matching temperature. The phase matching condition for our crystal only holds for 852 nm within a certain temperature range, thus it was necessary to measure this range experimentally in order to set the temperature for optimum second-harmonic generation. In order to measure this range, we sent 600 mW of infrared light into the cavity, and measured the blue light power generated while adjusting the temperature at 0.1°C intervals. This measurement given in Figure 4.8 shows us that the phase matching follows the expected sinc^2 shape. As a result, we learned that the optimal phase matching temperature was around 48.3°C, with a 1.5°C FWHM temperature range.

4.3.3.3 SHG Efficiency

In order to estimate the second-harmonic output that should be produced by the doubler, we used the expressions developed in Section 3.2.2.2.

If we first assume an input power of 600 mW and an E_{NL} of 2%/W and intracavity losses of 2%, plotting Equation 3.25 yields us the curve shown in Figure 4.9a. We see that the SHG output efficiency levels out at coupler transmissions of around 10-13% before starting to decrease. Therefore, we can use a 12% coupler to obtain efficient performance. Next we can use the same expression to plot a theoretical curve of the SHG output for this coupler, as a function of the input pump power. This gives us the results shown in Figure 4.9b.



(a) SHG power output vs. input coupler transmission with a fixed 600 mW input pump power.

(b) SHG power output vs. input pump power using a fixed input coupler of 12% transmission.

Figure 4.9: Using Equation 3.25 to predict the SHG output based on the input coupler and pump power.

With the proper phase-matching temperature having been determined, we were able to obtain a maximum production of 330 mW of 426nm light with an input of 600 mW of 852nm light, for an overall efficiency of $\eta = 55\%$ [Villa *et al.*, 2007]. We were also able to properly measure the SHG curve as a function of input power.

As we can see in Figure 4.10, the experimental results of the doubler follow the theoretical curve up until a certain power, at which point the power output begins to slowly diverge. It is suspected that this divergence comes from birefringence effects at high pump powers preventing us from locking the cavity at its peak output. While we were able to obtain a relatively high power output, it was necessary to translate the crystal after a certain time because the output power rapidly deteriorated. This could be due to heating effects inside of the crystal, optical degradation such as gray-tracking [Boulangier *et al.*, 2000], or more likely, optical damage on the crystal which degraded its surface quality.

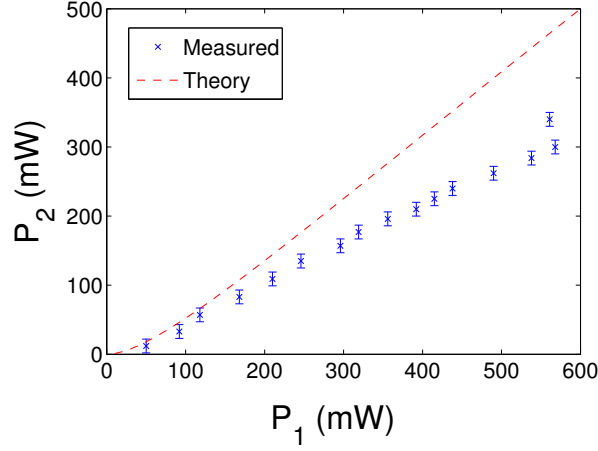


Figure 4.10: 426 nm output power measured from the doubler vs input at 852 nm, compared with theoretical prediction given by Equation 3.25. Divergence from theory at 250 mW is likely due to thermal effects in the crystal.

4.4 OPO Cavity

We can now begin to focus on the OPO, our primary instrument for squeezed light generation. The OPO cavity has a similar bow-tie design to the doubler, with a PPKTP crystal mounted between the two curved mirrors. Unlike the doubler, the OPO normally functions in a mode where we inject a vacuum state into the cavity, thus we don't have the same buildup of high intracavity power. As a result, we are not at risk from suffering from the effects of heating the crystal such as thermal lensing, or changes in the crystal size due to thermal effects. This allows us to use a slightly more tightly focused waist in the crystal of $w_o = 45\mu m$, while the cavity's second waist is at $w_1 = 200\mu m$. The curved mirrors have a radius of curvature of $R = 100\text{ mm}$, and the cavity has a total length of $l = 550\text{ mm}$. We use a slightly larger angle of reflection, of $\theta = 9.9^\circ$, and have selected an output coupler with a transmission of $T = 7\%$. The cavity has a bandwidth of around 10 MHz. Figure 4.11 shows a schematic of the cavity layout.

As optical losses play a more critical role in squeezed light generation, we measured the finesse of our OPO using the same method as for the doubler. This measurement gave us a finesse value of $\mathcal{F} = 60 \pm 4$, which corresponds to $10\% \pm 1\%$ losses. As we use a 7% output coupler, this again confirms our previously measured crystal absorption rate of around 2%. We similarly measured the nonlinear efficiency in the OPO and found a value around 2.6 %/W, which is similar to our measurement in the doubler's crystal. The slight variation is likely due to factors such as variations in the crystal sample, focusing, and surface deterioration.

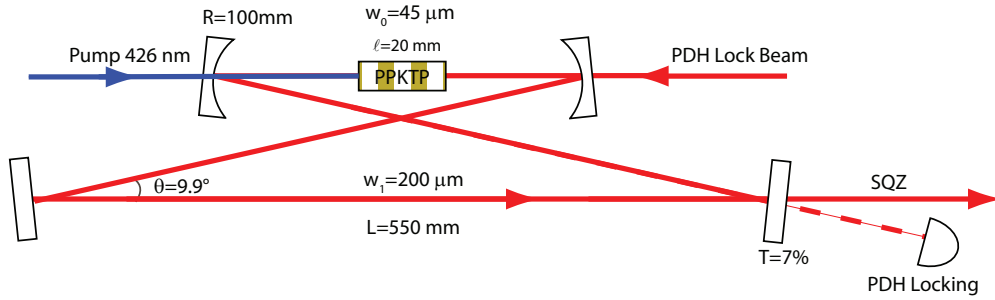


Figure 4.11: OPO cavity geometry, with lock beam propagating opposite to the squeezed light. Mirrors of radius of curvature $R = 100\text{mm}$ create a $w_0 = 45\mu\text{m}$ waist at the center of the $l = 20\text{mm}$ PPKTP crystal. The squeezing exits through a $T=7\%$ output coupler.

4.4.1 Cavity Locking

For locking the OPO, we needed a robust method which would require little daily maintenance. We furthermore wanted to allow a wide locking bandwidth in order to rapidly correct the cavity fluctuations and produce stable squeezing.

We locked the cavity by sending a lock beam through a high-reflectivity mirror, in a direction counter-propagating with respect to the squeezing. Since the mirror was highly reflective, trying to detect the reflected light would not allow us to observe any absorption peaks, as only 0.01% of the light would be transmitted into the cavity. We thus carried out all of our detection of the lock beam with the light transmitted through the cavity and exiting from the output coupler.

4.4.1.1 Tilt Locking Attempts

Due to our previous success in using tilt locking for the doubler, we initially tried to use it on the OPO as well. The implementation of this method posed several technical problems that made using it impossible. Tilt locking provides us with a method for measuring beam displacement by measuring intensity fluctuations on the photodiode. However with the OPO, we noticed that our tilt-locking photodiode detected much larger intensity fluctuations than when it was used with the doubler cavity. This is likely due to the fact that the light used to lock the OPO traveled a much larger distance before reaching the photodiode than the light used to lock the doubler. As a result, the locking for the OPO was rendered much more sensitive to any sources of displacement of our lock beam. These detection sensitivities included mechanical vibrations of the cavity, optical misalignments, as well as the effects of electronically controlling the cavity piezo. Another issue was that due to the high reflectivities involved, we had difficulties detecting both TEM_{00} and TEM_{01} modes on our photodiode. We thus measured very weak interference levels, which weakened the signal-to-noise ratio of our error signal. Furthermore, we wanted to use the weakest

beam possible for the lock beam, as this beam would still have 0.2% of its power reflected from the crystal surface. This reflected portion would then circulate in our cavity in the same direction as the squeezed light, and act as an injected signal to our crystal. As a result, we would no longer have a squeezed vacuum state at the output.

Thus we needed to balance between low reflection levels from the lock beam, and a beam with a high enough intensity to yield a strong enough detection signal to provide a stable lock. While we sent a beam of around 1 mW to the photodiode for the doubler, the OPO only left us with a beam of a few μW of power incident on our photodiode. We additionally found that this power was too weak to provide us with a usable signal. Efforts to amplify this signal did not improve our signal-to-noise ratio. Given all of these difficulties, we abandoned the tilt locking approach, and implemented a Pound-Drever-Hall (PDH) system.

4.4.1.2 Pound-Drever-Hall Locking

PDH is a more complicated scheme to implement than tilt locking due to the electronic requirements. However once its installed and working, it requires no adjustment on a daily basis, or special alignment of the beams. Due to its large modulation frequencies, it is also a high-bandwidth locking method. This method works by first taking our optical beam which we can express in the form $E = E_0 e^{i\omega t}$, and adding a phase modulation to it so that it transforms into

$$E = E_0 e^{i(\omega t + \beta \sin \Omega t)}, \quad (4.12)$$

where ω is the carrier frequency, β is the modulation depth, and Ω is the modulation frequency. This transformed beam thus contains two frequency components at $\omega \pm \Omega$. We then inject this beam into our cavity and measure the reflected beam, which has a reflection coefficient of $F(\omega)$, where $E_{ref} = F(\omega)E_{inc}$. We can then express the reflected modulation beam as [Black, 2001a]

$$E_{ref} = E_0 [F(\omega)J_0(\beta)e^{i\omega t} + F(\omega + \Omega)J_1(\beta)e^{i(\omega + \Omega)t} - F(\omega - \Omega)J_1(\beta)e^{i(\omega - \Omega)t}], \quad (4.13)$$

where the $J_i(\beta)$ are the Bessel functions. As the reflection coefficient depends on the cavity resonance, it vanishes when the cavity is at resonance. We can use this fact to create an error signal by detecting the reflected light with a photodiode, and mixing its photocurrent with our reference modulation frequency Ω . We then pass this through a low-pass filter which produces a DC output signal ϵ given by Equation 4.14, that represents the derivative of our light intensity with respect to frequency. We can use this output directly as an error signal to control our feedback loop, which is given by [Black, 2001b]

$$\epsilon = P_0 \frac{d|F|^2}{d\omega} \Omega \beta. \quad (4.14)$$

4.4.1.3 Electronic Implementation

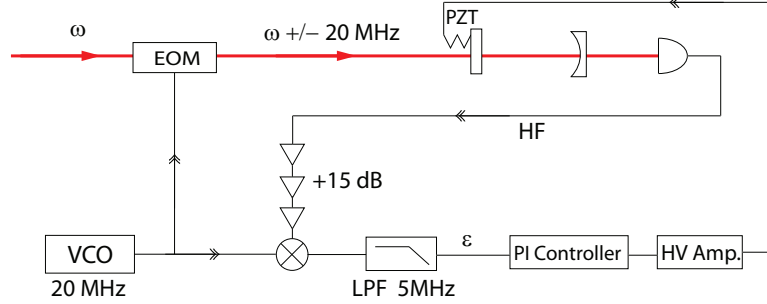


Figure 4.12: Electronic block diagram for our PHD setup. A VCO sends a 20 MHz RF signal to an EOM who phase modulates our lock beam. A photodiode detects the modulation sidebands, and its amplified output is demodulated and low-pass filtered to create an error signal.

In order to implement this for our OPO, we added phase modulations to our lock beam using a NewFocus 4001 resonant electro-optical modulator (EOM) which was modulated by a 20 MHz RF signal sent from a homemade VCO. We then sent 10 mW of this modulated light into the cavity and detected the transmitted beam with a high-frequency photodetector whose circuit is shown in Appendix C, Figure 8.6. For this photodiode, we used an infrared LED as the photodetecting element. We then sent the photodiode high-frequency output into a homemade amplifier/mixer/filter circuit, which used components from Minicircuits, which pre-amplified the signal by 15 dB, and then demodulated and filtered it with a 5 MHz low pass filter. This allowed us to produce our error signal, which you can see in Figure 4.13. We then passed this signal to a simple integrating circuit whose circuit is shown in Appendix C, Figure 8.8, and then to a high voltage amplifier which actuated the cavity piezo. This locking scheme allowed us to successfully lock the OPO for an entire day, and obtain stable measurements of squeezing.

4.4.2 Pump Matching

For the observation parametric down-conversion, we used the second-harmonic beam created by the doubler to act as an optical pump for the OPO. For the OPO to function correctly, we needed to ensure that this pump beam was properly mode-matched to the cavity mode for the OPO. Because the OPO is not resonant for the

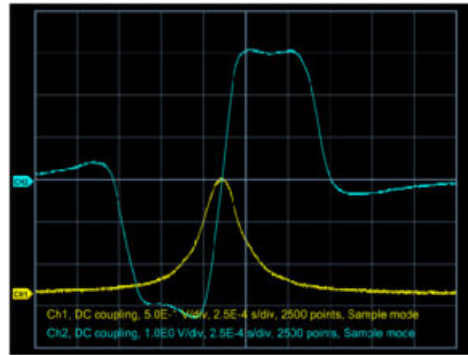


Figure 4.13: Error signal obtained with the PDH method overlaid onto the cavity peak. We see that the value of the error voltage is zero at the cavity resonance.

pump however, we did not have the visual feedback that we typically have with cavities in order to tell us if it is properly aligned. The only indication we do have in this situation, is if the OPO threshold is at the power level that we expect.

We initially tried to implement a scheme where we set up an interferometer in between the doubler and OPO. The idea was that we could temporarily operate the OPO as a doubler, and by superposing the blue light from the doubler and the OPO and applying a relative phase shift, we would be able to easily detect interference fringes, and adjust the matching and alignment as needed. We ran into difficulties properly matching the two cavities given our table space, and were forced to abandon the idea. In the end, we followed a simplified scheme where we temporarily replaced the OPO mirrors with blue-light reflecting mirrors so we could render the OPO resonant for the pump. This allowed us to have the necessary visual feedback about the matching quality, and easily match the beam to the cavity as we typically do with any other cavity. Once we determined the proper matching configuration, we fixed the mode-matching optics, and replaced the red-reflecting OPO mirrors.

4.4.3 Classical Observations

4.4.3.1 OPO Threshold

We have seen in Section 3.3.1 that the gain diverges and the squeezing approaches its maximum value as the pump power approaches the threshold. Thus we need to assure that our doubler would produce sufficient amounts of light to surpass this threshold without problem. This ability is also useful for verifying the pump alignment as described in the previous section.

Although the doubler was able to produce over 300 mW of blue light, we noticed that this performance was only short lived, and we had rapid degradation of the pump power. Typical pump powers ranged to around 160 mW, with 500 mW input into the

doubler. Thus in order to assure an easily obtainable threshold level, the threshold had to rest below this value.

As the threshold power depends on the OPO output coupler transmissivity, we tested several different output couplers in order to find one which would give us the optimal balance between a low threshold, and high squeezing. In Table 4.1, we list the thresholds measured for each output coupler. We see that our measured values are within 10% of our theoretical threshold powers calculated using Equation 3.48

Output Coupler	1%	2.5%	5%	7%	10%	12%
Measured P_{th}	14 mW	33 mW	45 mW	90 mW	125 mW	>160 mW
Theoretical P_{th}	9 mW	20 mW	47 mW	78 mW	140 mW	188 mW

Table 4.1: Output couplers and threshold pump powers tested for the OPO. Uncertainty of ± 3 mW on measured threshold values.

Although the 10% coupler provides us with a threshold value less than our maximum pump power, we found it difficult to observe the threshold when the pump beam became slightly disaligned. Additionally, the 10% coupler did not greatly change the amount of squeezing we measured from the OPO. This could be due to heating effects at high pump powers, which were exacerbated by the crystal's high absorption rate of 426 nm light. Thus we rested with the 7% coupler.

4.4.3.2 Type I OPO Degeneracy

As stated earlier, the PPKTP crystal in our OPO uses a Type I phase matching. OPOs that contain a Type I crystal have a characteristic tuning curve such as that shown in Figure 4.14, which shows their above threshold behavior. There exists a certain degeneracy temperature for the crystal, T_{deg} , such that if we pump the OPO above its threshold power while the crystal is below this temperature, the OPO will not produce any output as the phase-matching condition will not be satisfied [Eckardt *et al.*, 1991], [Lam, 1998]. We begin to satisfy the phase-matching condition by increasing the temperature to T_{deg} , at which point the OPO will output signal and idler beams which both have the same frequency and polarization. If we further increase the temperature beyond this point, the signal and idler beams will lose their degeneracy, and begin to take on frequencies such that $\omega_{signal} + \omega_{idler} = \omega_{pump}$.

4.4.3.3 OPO Above Threshold

As we require that our squeezed light be at the degeneracy frequency in order to have both signal and idler beams be resonant with the Cesium D_2 line, we can use the above threshold behavior as means of calibrating the OPO. The phase-matching condition holds for a relatively wide temperature range for our system. Once the OPO

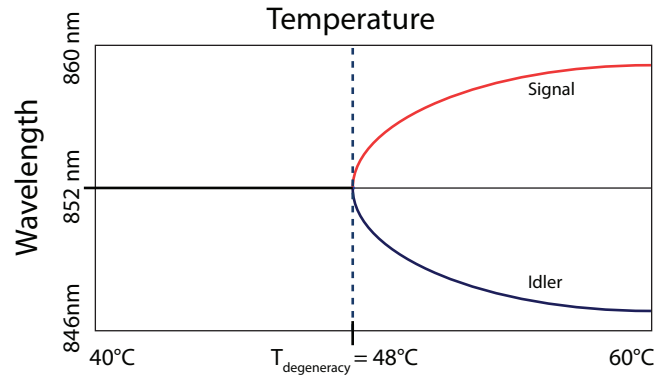


Figure 4.14: Characteristic oscillation curve for Type I crystals. No photons are emitted above threshold below a certain degeneracy temperature. Above this temperature, signal and idler photons of different wavelengths are emitted.

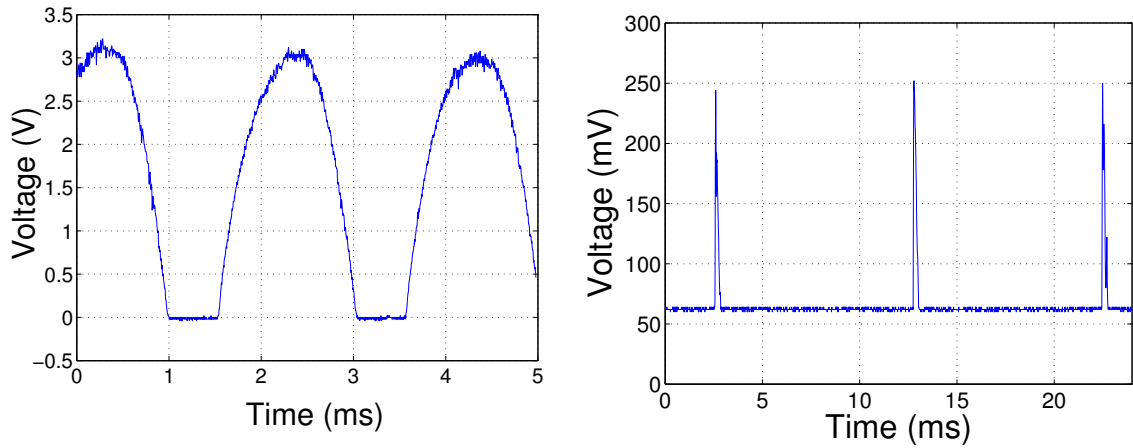
oscillation began, we noticed that there was a 2°C temperature window where we could observe the above-threshold photon emissions. In Figure 4.15a, we can see that the above-threshold photon pairs produced gives the emission a parabolic shape, as the non-degeneracy of our output produces a spread of photon frequencies.

Adjusting the phase-matching temperature allows us to adjust the frequency difference between the emitted signal and idler photons. By placing ourselves at the degeneracy temperature just before we lose our above threshold output, we can approach the degeneracy condition for the OPO and obtain frequency-degenerate signal and idler beam outputs. This resembles the trace shown in Figure 4.15b.

4.4.3.4 OPO Injected Below Threshold

We have also seen how the OPO operating below threshold leads to the phase sensitive amplification and deamplification of our input field. We can observe this effect by studying the parametric gain of our system. In order to measure the gain, we installed a piezo on a mirror on the pump beam's optical path, which allowed us to change the relative phase between the pump, and the injected seed beam. When we set our input pump to 90% of the threshold, the deamplification of the seed approached 50%, while the amplification approached a maximum of 10x.

In the next chapter, we will show how the operation of the OPO in this below-threshold configuration allowed us to produce squeezed states.



(a) OPO oscillating far from degeneracy. Signal and idler photon pairs ω_s and ω_i are emitted at random frequencies which conserve the energy relation $\omega_p = \omega_s + \omega_i$.

(b) We seek the degeneracy condition by lowering the crystal temperature to the point where the above threshold photon emission stops. This is represented by a finer frequential spread in the emitted photon pairs as illustrated in Figure 4.14.

Figure 4.15: Above threshold operation of an OPO with a 90 mW threshold pumped at 130 mW with 426 nm light, and no injected seed beam. Light emission is measured on an oscilloscope while the cavity length is swept through resonance. The OPO cavity has a 550 mm length and a 10 MHz bandwidth.

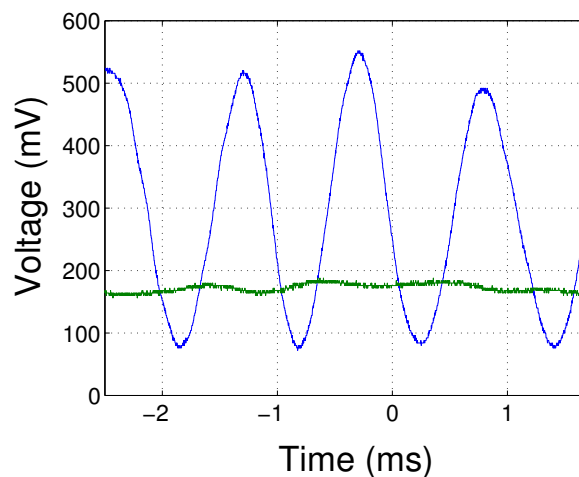


Figure 4.16: Parametric gain of the OPO with a relative phase sweep between the pump and injected beam. OPO output shown with and without pump at 50% of threshold

Detection and Characterization of Squeezed Light

Contents

5.1	Balanced Homodyne Detection	66
5.1.1	Measuring the Rejection Ratio of Subtraction	68
5.1.2	Electronic Noise Floor	69
5.1.3	Detector Balancing	70
5.1.4	Visibility	70
5.2	Continuous-Wave Squeezing Measurements	71
5.2.1	Comparison With Theory	73
5.2.2	Accounting for Losses	73
5.3	Quantum State Tomography	74
5.3.1	Homodyne Measurements	74
5.3.2	Tomographic Reconstruction	75
5.3.3	Maximum Likelihood Estimation	75
5.3.4	Experimental Implementation	76
5.4	Creation of Pulses of Squeezed Light	78
5.4.1	AOM Implementation	79
5.4.2	Optical Chopper Implementation	80

Until now, we have discussed the construction and functioning of the OPO in the classical regime. We have also seen how pumping the OPO below threshold while sending a vacuum state as input will allow us to produce squeezed vacuum states at the OPO output. The next step in our task is to measure the quantum states created, and quantify the amount of squeezing produced.

The detection of quantum states of light is based on the principle that the current fluctuations produced by light incident on a photodetector are proportional to the quantum fluctuations of the detected light itself. When we can diminish these fluctuations down to the standard quantum limit, the fluctuations detected by our detector represent what we call *shot noise*. By ensuring that our detector has the sensitivity to measure light at its shot noise limit, we become capable of also measuring squeezed states when its fluctuations go below this limit.

5.1 Balanced Homodyne Detection

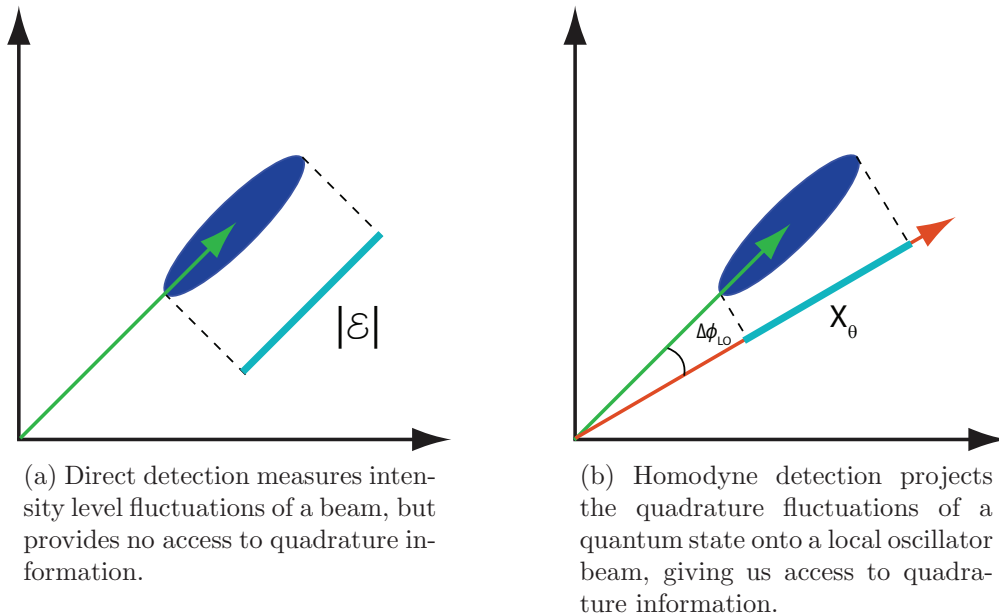


Figure 5.1: Illustration of direct photodetection vs. homodyne detection.

We have seen that generating squeezed states is a phase-sensitive process, producing states which have quadrature dependant variances. Using direct photodetection methods to measure these states however, only provides us with measurements of the intensity fluctuations of the light and offers us no information on the individual field quadratures. As it is precisely this quadrature noise that characterizes the quantum

nature of a squeezed state, we must use another method than direct detection to measure our states. The method of balanced homodyne detection as we discuss here [Bachor and Ralph, 2004], allows us to access these different quadratures of the light field, as illustrated in Figure 5.1.

To carry out a homodyne detection, we use a 50/50 beamsplitter to mix our signal beam with a mode-matched coherent local oscillator at the same optical frequency, as shown in Figure 5.2. This provides a fixed phase reference for our signal. On the condition that the local oscillator is much more intense than our signal, such that $|\mathcal{E}_{LO}| \gg |\mathcal{E}_S|$, we can treat the local oscillator classically and treat our signal quantum mechanically, linearizing our signal field into the expression $\mathcal{E}_S = \langle \mathcal{E}_S \rangle + \delta \mathcal{E}_s$. In the case of squeezed vacuum, our signal has low photon number which is approximately zero, and thus we can express our signal as a decomposition of quadrature noises $\delta \mathcal{E}_S = \delta \mathcal{E}_S^X + i\delta \mathcal{E}_S^Y$.

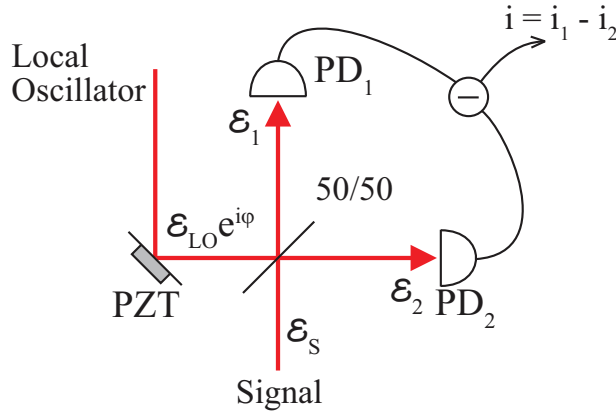


Figure 5.2: An intense phase-scanned local oscillator \mathcal{E}_{LO} mixes with a weaker signal \mathcal{E}_S using a 50/50 beamsplitter, and is sent onto two balanced photodiodes. By subtracting their photocurrents, we obtain our quadrature signal.

Upon passing our signal and local oscillator through a 50/50 beamsplitter the output fields satisfy the following relations

$$\mathcal{E}_1 = \frac{1}{\sqrt{2}} (\mathcal{E}_{LO} e^{i\phi_{LO}} + \delta \mathcal{E}_S^X + i\delta \mathcal{E}_S^Y) \quad (5.1)$$

$$\mathcal{E}_2 = \frac{1}{\sqrt{2}} (\mathcal{E}_{LO} e^{i\phi_{LO}} - \delta \mathcal{E}_S^X - i\delta \mathcal{E}_S^Y). \quad (5.2)$$

We can then separate our output signals into their real and imaginary parts to obtain

$$\mathcal{E}_1 = \frac{1}{\sqrt{2}} [(\mathcal{E}_{LO} \cos \phi_{LO} + \delta\mathcal{E}_S^X) + i(\mathcal{E}_{LO} \sin \phi_{LO} + \delta\mathcal{E}_S^Y)] \quad (5.3)$$

$$\mathcal{E}_2 = \frac{1}{\sqrt{2}} [(\mathcal{E}_{LO} \cos \phi_{LO} - \delta\mathcal{E}_S^X) + i(\mathcal{E}_{LO} \sin \phi_{LO} - \delta\mathcal{E}_S^Y)]. \quad (5.4)$$

Now we can detect the light intensity incident on each photodiode using the expression $I_i \propto \mathcal{E}_i \mathcal{E}_i^* = |\mathcal{E}_i|^2$. Each photodiode will produce a photocurrent i_i proportional to this intensity. By subtracting these photocurrents, we obtain a resulting photocurrent that is proportional to

$$i = i_{1-2} = 2\mathcal{E}_{LO} [\delta\mathcal{E}_S^X \cos \phi_{LO} + \delta\mathcal{E}_S^Y \sin \phi_{LO}], \quad (5.5)$$

with the variance of this difference given by

$$\Delta i^2 \approx 4\mathcal{E}_{LO} \left(\langle \delta\mathcal{E}_S^{2(X)} \rangle \cos^2 \phi_{LO} + \langle \delta\mathcal{E}_S^{2(Y)} \rangle \sin^2 \phi_{LO} \right). \quad (5.6)$$

This shows us that the homodyne detection provides us with a current that is sensitive to the relative phase between our local oscillator and our signal, and is proportional to a linear combination of our quadrature fluctuations. Furthermore, these equations show that the local oscillator noise term does not contribute in our measurement. We can express this combination of quadrature fluctuations as our generalized quadrature, X_θ . Thus we can consider the homodyne detector output as a direct measurement of our signal quadrature, and the photocurrent noise for a given phase can accurately represent our quadrature noise.

In practice there are several critical factors necessary however, in order to assure that the homodyne measurement illustrated here functions properly.

5.1.1 Measuring the Rejection Ratio of Subtraction

In order to verify that the classical noise of the local oscillator is properly subtracted and only the quantum noise is left behind in the photocurrent, we need to measure the rejection ratio of the subtraction circuit. We carried out this measurement by using an electro-optic modulator to create a 3 MHz intensity modulation of the seed beam passing through the OPO. We did this by passing the beam through a phase modulator which created a polarization modulation on it, and then we passed it through a PBS cube which created intensity modulations on both output ports of the cube. These intensity modulations on the two output ports have a relative phase shift of π due to energy conservation, thus when beams from both ports are sent into the homodyne detector photodiodes, the subtraction of their photocurrents should give us zero signal. When one port is blocked, we then obtain a positive signal. By comparing the ratio of

the one-port signal to the two-port signal, we were able to measure that the photodiode subtraction rejection ratio was at -27dB .

5.1.2 Electronic Noise Floor

In order to assure that our measurements were not disrupted by external noise sources, we needed to first measure the noise characteristics of our homodyne detector. The electronic noise floor of the detector provides the lower noise limit, and we needed to assure that it was far enough below the optical shot noise to provide a valid measurement of the squeezing. We sent 8 mW of light into each photodiode, which was the maximum allowed before saturating the photodiodes. By observing the photocurrent on a spectrum analyzer, we obtained the measurements shown in Figure 5.3, and observed the shot noise level to be at about -77 dBm . We then blocked the light entering the photodiodes to measure the dark noise produced by the photodiodes themselves, and found that it was 9 dBm lower than the shot noise level at -86 dBm . Finally we measured the electronic noise floor of the spectrum analyzer by disconnecting the photodiodes, and found that it had an electronic noise of -89 dBm , which was 3 dBm lower than the dark noise from the photodiodes. The 9 dBm difference between the shot noise and dark noise from the photodetectors indicates that our local oscillator was intense enough to provide a proper measurement.

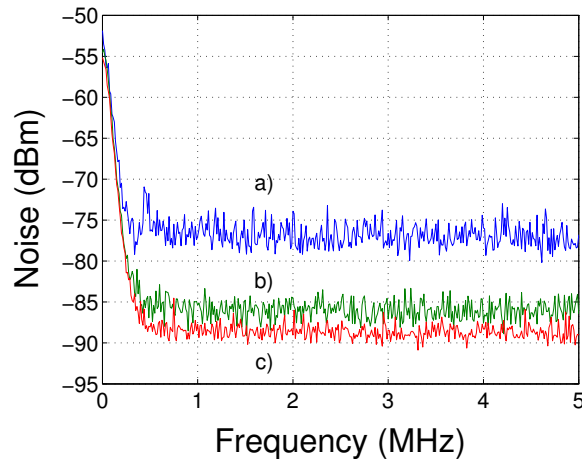


Figure 5.3: Calibration of the homodyne detector noise floors a) Shot noise from a 16 mW local oscillator at -77 dBm b) Dark noise level of the photodiodes with photodetectors blocked at -86 dBm c) Spectrum analyzer noise at -89 dBm with photodetectors disconnected.

5.1.3 Detector Balancing

In addition to being electronically balanced, the detectors needed to be optically balanced as well. We verified the optical balance by observing the AC output on the spectrum analyzer over a 0-5MHz bandwidth. As a balanced detector should properly subtract classical noise, we used the low-frequency noise level as a measure of the optical imbalance on the high-frequency outputs. By using a half-wave plate placed in front of the homodyne detector to rotate the polarization, we could control the distribution of power on the two photodiodes, and thus observe the changes to the noise spectrum on the spectrum analyzer, as shown in Figure 5.4. This allowed us to adjust the optical power distribution in order to minimize the noise traces over the largest bandwidth, thus assuring an optical balance between the two photodiodes.

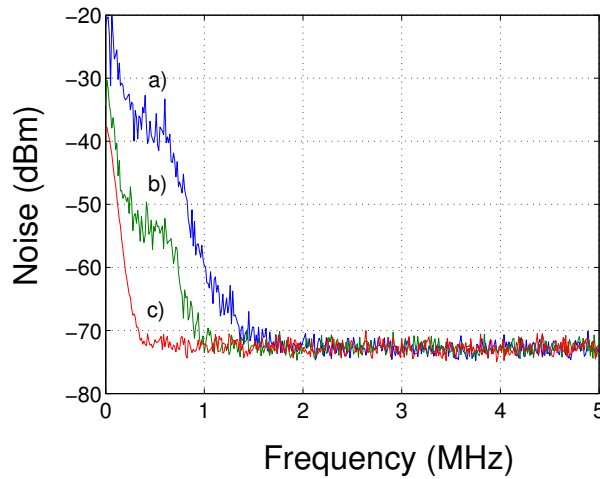


Figure 5.4: We use the noise traces to balance the subtracted AC output for the homodyne detectors while optically balancing the light incident on the detectors. a) Subtracted output with all light incident on one photodiode b) improved electronic subtraction with 70/30 optical balance c) 50/50 optical balance on photodiodes and optimal electronic subtraction.

5.1.4 Visibility

Performing a homodyne detection requires the signal have a high spatial-mode overlap with a local oscillator. A poor overlap between the signal and LO modes can be represented as losses in our detection of squeezed states, and thus diminish the amount of squeezing detected.

We performed the visibility measurements by injecting a seed beam into the OPO so that the output light would have the same spatial profile as the squeezed vacuum

mode. We then matched the LO beam power to the OPO signal power, and scanned the relative phase between the two beams by using a piezo attached to the LO path. This produced interference fringes between the signal and local-oscillator beam, whose amplitude we then measured to quantify the visibility. The following relation gives us a value of the signal visibility using this fringe measurement [Bachor and Ralph, 2004]

$$VIS = \frac{I_{max} - I_{min}}{I_{max} + I_{min}}. \quad (5.7)$$

For our OPO, we achieved a maximum visibility of up to 99% between our local oscillator and signal beams, however, typical results were around 95%. Our inability to attain more perfect mode overlap is likely due to astigmatism introduced into the signal beam by the OPO cavity angles, which limited the maximum amount of mode overlap we could obtain.

5.2 Continuous-Wave Squeezing Measurements

For the actual measurements, once we had the homodyne detector properly balanced, we sent 16 mW of power into the local-oscillator so that it would be much more intense than the OPO signal. We then locked the doubler and OPO at resonance, set the pump power to 80 mW, slightly below the 90 mW threshold, and scanned the relative phase between the local-oscillator and the OPO output. We then sent the subtracted photocurrent from the homodyne detector to an Agilent E4411B spectrum analyzer set to zero span mode, at an observation frequency of 1.5 MHz. We set the resolution bandwidth to 100 kHz, the video bandwidth to 100 Hz, and the sweep time to 80 ms. With these settings, we were able to observe the amplification and deamplification of the quadrature noise shown in Figure 5.5 with the deamplification falling below the shot-noise limit, thus signifying the production of squeezed states. We observed 3.0 ± 0.5 dB of noise reduction in the squeezed quadratures, and 9 dB of amplification in the anti-squeezed quadrature.

We then analyzed the noise spectrum over a broader bandwidth between 1 MHz and 5 MHz, and observed that the amplitude of the squeezing and anti-squeezing quadratures diminished as we moved up in frequency towards the cavity bandwidth, as shown in Figure 5.6a

We also analyzed the low frequency behavior from 0-500 kHz as shown in Figure 5.6, in order to determine the lower limit of our squeezing production. Producing squeezing at low frequencies is important because we want to use EIT for storing our state onto the atoms. The EIT transparency window is centered around the carrier frequency of our squeezed signal, and has a limited bandwidth. Thus, having low-frequency squeezing ensures that we manage to store the quantum correlations in the limited bandwidth window available through EIT. We continued to observed -3 dB of

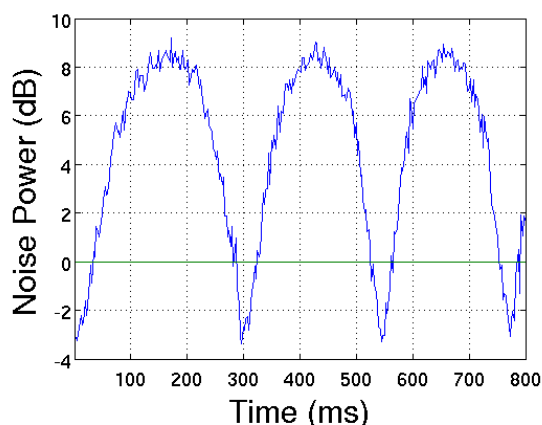
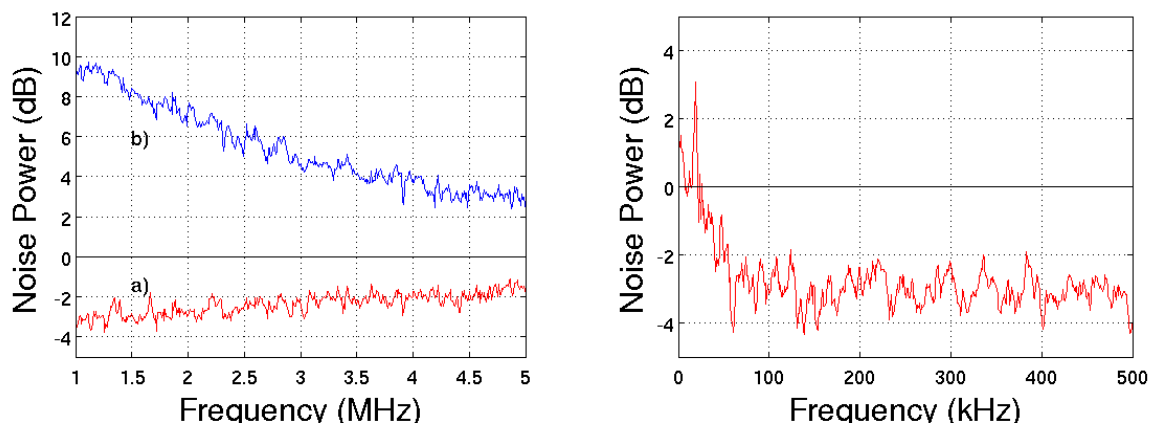


Figure 5.5: -3.0 ± 0.5 dB of squeezed vacuum detected at 1.5 MHz while scanning the LO phase. The resolution bandwidth is set to 100 kHz and the video bandwidth to 100 Hz.



(a) Normalized noise variance of the a) squeezed and b) anti-squeezed quadratures from 1 MHz to 5MHz.

(b) Squeezing measured from 0-500 kHz. We see that squeezing is preserved all the way down to 30 kHz, making the light compatible for EIT storage in our quantum memory.

Figure 5.6: Squeezing measurements over a) a broad spectrum, and b) at low frequencies.

squeezing all the way down to 50 kHz, with the squeezing completely disappearing at 30 kHz. Given that the electronic circuitry of our photodiodes imposed a 25 kHz cutoff frequency, we could not observe squeezing more precisely beyond that limit.

5.2.1 Comparison With Theory

We can calculate the theoretical amount of squeezing that should be produced at the OPO output for our OPO configuration, using the relation derived earlier

$$S_-(\Omega) = 1 - \frac{T}{T + L} \frac{4\sigma}{(1 + \sigma)^2 + \Omega^2}. \quad (5.8)$$

Here, the pump parameter σ represents the amount of pump we send as a percentage of the OPO threshold, T is the OPO output coupler transmission, L the intracavity losses, and Ω the analysis frequency normalized to the cavity bandwidth, which for us was 10 MHz. For our measurements, we took $\sigma = 0.9$, $\Omega = 0.1$, $T = 0.07$, and $L = 0.02$. This prediction showed us that around -5.8 dB of squeezing should be produced at the OPO output.

5.2.2 Accounting for Losses

This prediction of -5.8 dB squeezing production only represents the idealized case given our 2% of cavity losses, however it does not take into account the inefficiencies of the detection process.

In reality, we have several sources of detection inefficiencies whose presence reduces the amount of squeezing we detect. These inefficiencies primarily come from optical losses of the beam as it travels from the OPO to the homodyne detector η_{opt} , the mode mismatch between the squeezed-vacuum and the local oscillator η_{vis} , and the imperfect quantum efficiency of our photodiodes η_{quant} . We can thus assign a global efficiency to our entire detection process with

$$\eta_{det} = \eta_{vis}^2 \cdot \eta_{quant} \cdot \eta_{opt}. \quad (5.9)$$

For our experiments, we can set a visibility estimate of 96%, an estimate 5% for our optical path losses, and an estimate of 90% for the quantum efficiency of our photodiodes. This results in an overall detection efficiency of $\eta_{det} = 0.9 \cdot 0.96^2 \cdot 0.95 \approx 0.8$. With this value in place, we can now derive an estimate of the amount of squeezing that we will realistically measure by using our beamsplitter model for losses given by Equation 2.60

$$S_-^{det}(\Omega) = S_-^{opo}(\Omega) \eta_{det} + (1 - \eta_{det}). \quad (5.10)$$

This expression gives us the detected noise measurement of our signal as a function of the detection efficiency, and the noise at the OPO output. By using the values estimated above, we predict a detection closer to -3.9 dB of squeezing, as plotted in Figure 5.7.

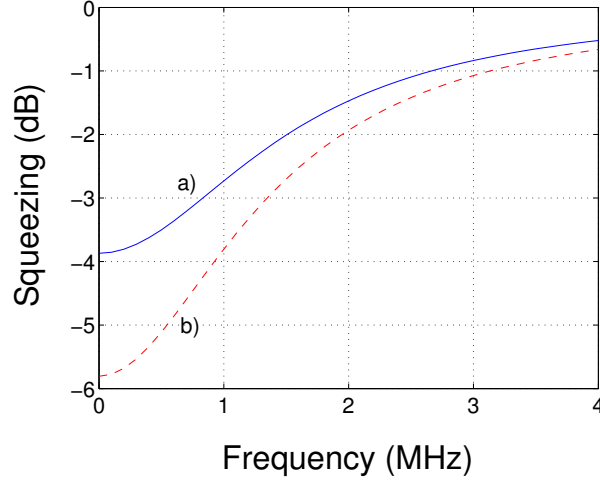


Figure 5.7: Squeezing prediction with a 7% output coupler, P_{Pump} at 90% of threshold, and 2% cavity losses with a) real detection inefficiencies of $\eta_{det} = 0.8$ and b) perfect detection efficiency $\eta_{det} = 1$.

This estimation corresponds well to the measured results once we take into account optical losses and detection inefficiencies. It thus shows that we have an accurate estimation for the operating parameters of our system.

5.3 Quantum State Tomography

As discussed in Chapter 2, the density matrix $\hat{\rho}$ provides us with the most complete representation of a quantum state, allowing us to calculate any quantity for our system that is predictable by quantum mechanics. We also saw earlier how the Wigner function provides a representation of the information contained within the density matrix. Quantum State Tomography (QST) is a technique that allows us to take the projective quadrature measurements of our system, and reconstruct the full density matrix and Wigner function for our quantum state. In this section, we will see how we carried out this task, leading to a complete characterization of our squeezed light.

5.3.1 Homodyne Measurements

The first step in QST is to build up a large amount of projective quadrature measurements. As we have seen earlier, the balanced homodyne detector provides us with a direct measurement of the quadrature fluctuations of the light

$$I_2 - I_1 = \hat{\mathcal{E}}_\phi = \frac{1}{\sqrt{2}}(\hat{a}e^{-i\phi} + \hat{a}^\dagger e^{i\phi}), \quad (5.11)$$

where ϕ represents the relative phase difference between the squeezed signal and the local oscillator. For a given local oscillator phase, the measured quadrature follows a probability distribution which is a projection of the state's Wigner function onto the linear combination of the state's two quadratures, which we can represent using the generalized quadrature x_θ . Thus the homodyne measurement provides us with direct probability distributions of quadratures of the state, and by scanning the local oscillator phase, we can measure these probability distributions for all phase angles in $[0, 2\pi]$.

5.3.2 Tomographic Reconstruction

Once we have measures for the quadratures for all of the phases, we can begin to use reconstruction techniques to estimate the density matrix for our state.

Historically, the technique of the Inverse Radon Transform [Leonhardt, 1997] was used to reconstruct the state from the measured quadrature distributions. However, this approach was shown to be prone to creating artificial artifacts in the reconstructed state, could lead to unphysical results, as well as being very sensitive to errors leading to instabilities in the data. We thus decided to use an approach which improves on some of the flaws of the inverse Radon transform.

5.3.3 Maximum Likelihood Estimation

The approach we decided to use, Iterative Maximum Likelihood Estimation (MLE), was outlined by [Banaszek *et al.*, 1999] and [Reháček *et al.*, 2001], and developed into an algorithm by [Lvovsky, 2004].

MLE works by beginning with an arbitrary starting point, and iteratively converging towards an estimation of the density matrix that would have the highest probability of producing our observed dataset [Lvovsky and Raymer, 2009]. The estimation process assures that we have a physically meaningful state at the end, without the artificial artifacts introduced by the inverse Radon transform.

We can begin to quantify this approach by starting with the definition of *likelihood*, where the likelihood of our state is given by the product of all the marginal probabilities

$$\mathcal{L}(\hat{\rho}) = \prod p(|x_\theta, \theta\rangle). \quad (5.12)$$

The individual probabilities here represent the probabilities of obtaining a given quadrature measurement x_θ at a given phase angle θ . This expression tells us that we need to record enough data to build up accurate probability histograms of each generalized quadrature, at multiple phase angles so that we can cover the entire phase space. The algorithm then introduces an operator $\hat{R}(\hat{\rho})$

$$\hat{R}(\hat{\rho}) = \sum_{i=1}^N \frac{\Pi(x_{\theta_i}, \theta_i)}{p(x_{\theta_i}, \theta_i)}, \quad (5.13)$$

where $\Pi(x_{\theta_i}, \theta_i)$ are the projectors constructed from a set of basis states $|x_{\theta_i}, \theta_i\rangle$. We can then use the following update relation to estimate the density matrix that is incrementally more likely to have produced the dataset.

$$\rho' = \frac{\hat{R}(\hat{\rho})\hat{\rho}\hat{R}(\hat{\rho})}{\text{Tr}\left(\hat{R}(\hat{\rho})\hat{\rho}\hat{R}(\hat{\rho})\right)}. \quad (5.14)$$

By iterating over Equation 5.13 and Equation 5.14 many times, we can eventually converge towards a reasonable estimation for our state $\hat{\rho}$.

5.3.4 Experimental Implementation

The first step in performing the tomography involved acquiring a digital representation of the photocurrent from the homodyne detector, which contained all of the information necessary to reconstruct our state.

We sent the homodyne difference photocurrent to a ZFL-500LN-BNC Low Noise amplifier, which amplified our signal by 5 dB, allowing us to slightly increase our signal-to-noise ratio. We then sent the photocurrent to a computer-hosted NI PCI-5122 digitizer containing 256 MB of RAM, which we used to perform a running acquisition of the photocurrent at 100 MHz, with 14-bit resolution. We triggered the beginning of the card acquisition on the rising edge of the TTL controlling the local oscillator sweep, and arranged the sweep frequency so that we could obtain a 2π phase rotation during the acquisition window. Using this card, we recorded 1 million data points of shot noise by blocking the OPO output, and 1 million data points of squeezed quadrature noise while sweeping the local oscillator phase. This allowed us to obtain the digital representations of the photocurrents shown in Figure 5.8.

With these photocurrent acquisitions, we then normalized the squeezing points to the shot noise, and manually associated phase reference points to the squeezed data in order to create x_{θ}, θ pairs for all of the data points. We then divided the $0 - 2\pi$ phase points into 100 bins, sorted the quadratures by phases, and calculated the average quadrature value for each phase bin. Next, we needed to reconstruct our projectors $\Pi_{nm}(x_i, \theta_i)$ from the quadrature data, and thus needed to select a set of basis states to represent them. We selected the Fock basis, with the infinite Fock space truncated to 10 photons. We then used the quadrature data to construct the projectors using the expression [Lvovsky, 2004]

$$\Pi_{nm}(x_i, \theta_i) = e^{i(n-m)\theta_i} \left(\frac{1}{\pi}\right)^{1/2} \frac{1}{\sqrt{2^{n+m}n!m!}} e^{-x_i^2} H_n(x_i) H_m(x_i), \quad (5.15)$$

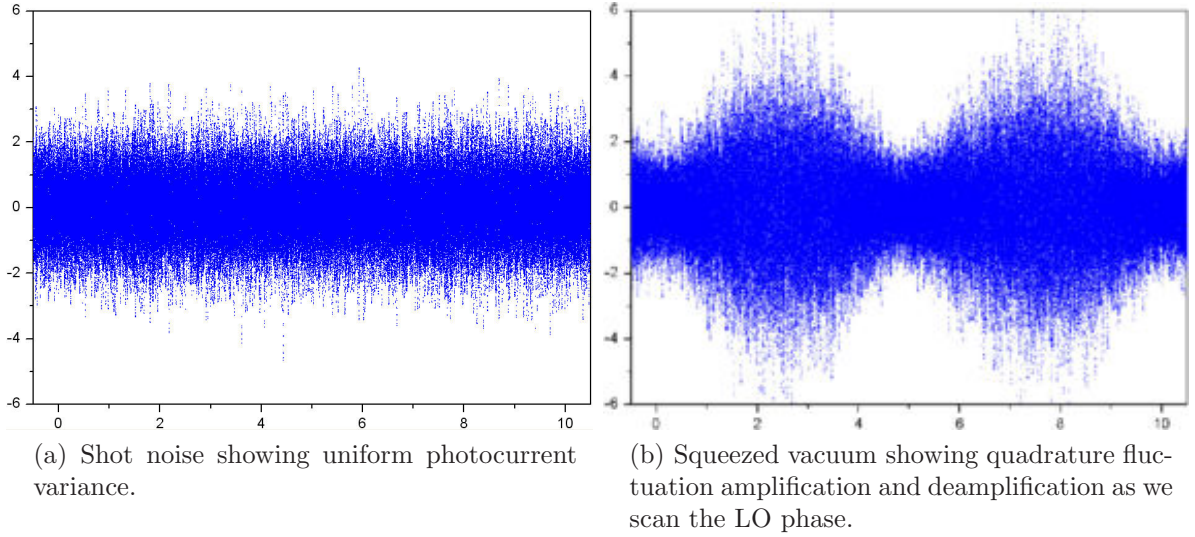


Figure 5.8: Digitized photocurrents of a) shot noise and b) squeezed vacuum recorded at 100 MS/s using a NI PCI-5122 digitizer.

where the $H_n(x_i)$ are the n^{th} order Hermite polynomials, and the x_i and θ_i are the quadrature and phase data. With these projectors, we then ran the MLE algorithm for 100 iterations, and obtained a reconstruction of the state's density matrix.

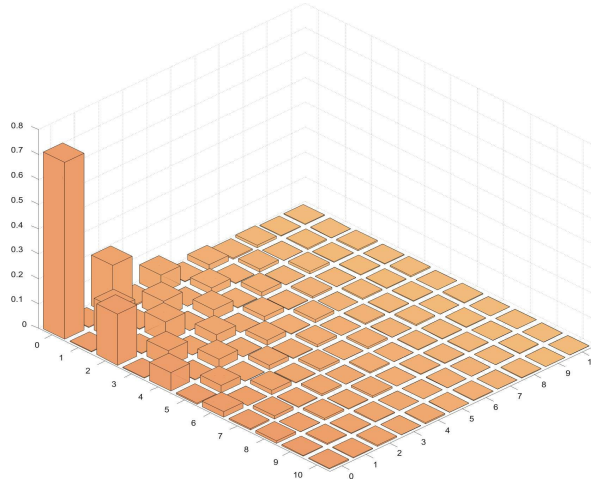


Figure 5.9: Density matrix of up to 10 photons estimated using iterative MLE method.

We see from Figure 5.9 that 10 photons are enough to perform our reconstruction, as there appears to be an almost zero probability of higher numbers of photons appearing. The noise calculations for this state indicate a measure of $1.97 \text{ dB} \pm 0.05 \text{ dB}$

of squeezing for this acquisition, which shows consistency with our spectrum analyzer measurements.

We also generated the Wigner functions for our state as shown in Figure 5.10, which show visually that we have managed to produce and reconstruct a state with asymmetric noise variances in its two quadratures, with one quadrature having a sub shot noise variance.

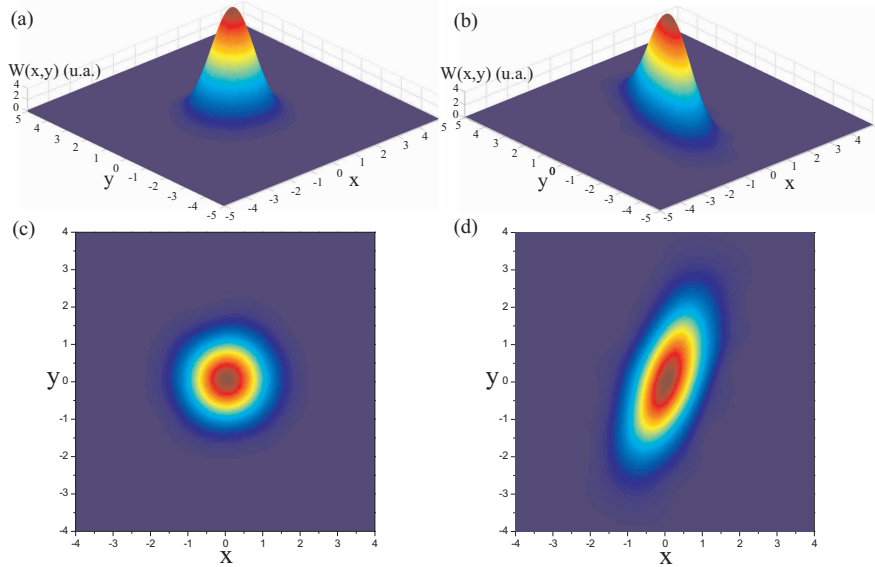


Figure 5.10: MLE reconstructed Wigner functions for a) shot noise and b) squeezed state. This corresponds to around 2.4 dB of squeezing.

5.4 Creation of Pulses of Squeezed Light

Once the tools for the generation and characterization of squeezed light were put into place, we needed to properly interface the light with the atomic system for storage. The atomic storage medium itself imposed a set of constraints on the means of storing the light. Firstly, we wanted to carry out many repetitions of the storage in a finite sized atomic medium, thus we needed to create pulses of squeezed light from the continuous OPO-generated source. The limited EIT storage lifetime also required that we create short pulses, thus we sought to create pulses sized between $1 \mu\text{s}$ - $5 \mu\text{s}$ in length. In creating such short pulses, we also needed to verify that the frequency components which were contained in the pulse would still preserve the squeezing. Because we would be sending pulses of squeezed vacuum, we would not be able to directly detect the pulse arrival. Yet, knowledge gained from prior experiments [Cviklinski, 2008] had shown us

that the EIT would require a precise timing of pulses to within 100 ns precision, thus the system that created the pulses would have to be stable, and have extremely low jitter, allowing us to predict the pulse arrival time to within 100 ns. Additionally, we wanted to run the experiment as quickly as possible, thus we sought to have a high repetition rate for the pulse creation. We predicted that the MOT would need around 18 ms to properly prepare the atomic cloud in between each storage run, thus we wanted to present a squeezed pulse to our MOT every 25 ms, which set another constraint on our pulse generation rate.

Another aspect that we needed to carefully consider was the fact that the squeezing in our pulse would be destroyed by any losses or inefficiencies in the pulse generation or detection process. Thus, we need a system to create the pulses which would minimize the losses, and we needed to properly time our detection as to maximize the measurement of squeezing, and minimize the measurement of the vacuum contributions.

Given our restrictions concerning the timing precision and optical losses, we considered two different techniques to generate the squeezed light pulses. AOMs are typically used to generate light pulses and offer a timing precision of around 100 ns, but often create optical losses of 20% on each passage of the beam through the AOM. Optical choppers add no losses to a beam as they either completely block, or completely allow the passage of a beam of light, however as they are mechanical devices, they offer much less timing precision. In the following sections, we will discuss our efforts to create optical pulses using these two approaches.

5.4.1 AOM Implementation

We initially wanted to avoid using an AOM to create the pulses, as we expected from measurements on similar AOMs that in the optimistic case, we would add 20% losses to our beam per AOM. After searching for high-performance models, we found an upgraded model of the AOMs that we previously used (MT110-A1-IR) from AA Optoelectronics. This upgraded model had a specification for 99% transmission at our wavelength, and 92% beam diffraction into the 1st order mode, as well as a rise time of less than 200 ns for our pulse edges, thus we could minimize our losses during the pulse measurements. Our measurements confirmed we could obtain characteristics with our system that approached these specifications, with 96% transmission and 93% diffraction per AOM. Thus, we decided to use two of them in a 0-order configuration as illustrated in Figure 5.11, where activating them would diffract the light away from our pathway leaving only $7\% \cdot 7\% \approx 0.5\% - 1\%$ of the original squeezed light in the optical path. We considered that this would be effective, as the 99% losses would effectively destroy the squeezing in the small amount of light that passed when we diffracted the beam, and we would only experience 8%-10% losses when the beam was transmitted.

The AOM offered the timing precision and repeatability of pulse creation and triggering that we had come to expect with previous AOM usage from other experiments.

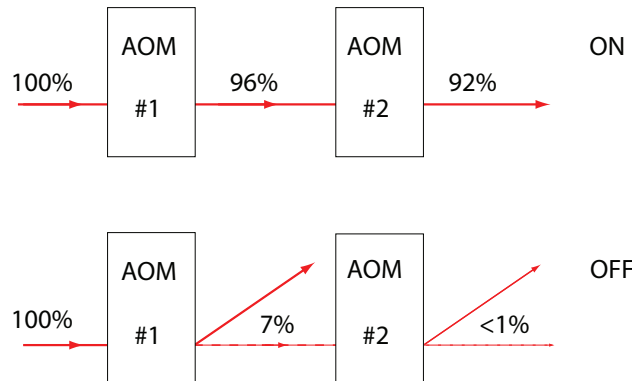


Figure 5.11: We send a TTL signal each AOM's RF driver to alternate between the on and off states, deviating the optical path to create an optical pulse.

The optical pulses were created only when we sent a TTL signal to the AOMs, and thus created a simple mechanism for creating the experimental timing sequence.

5.4.2 Optical Chopper Implementation

As we wanted to attempt to minimize losses as much as possible, we also explored usage of an optical chopper. One issue that we needed to consider when using an optical chopper were the pulse edges created by the mechanical operation of the chopper.

5.4.2.1 Optical Detection Losses Due To Pulse Edges

One problem that arises in the measurement of squeezed light pulses is that by creating the pulses using a chopper, we create sections of the pulse where the normalized light intensity is less than 1 during the pulse rise and fall times. We can consider these segments as periods when vacuum noise mixes with our squeezing, thereby increasing the amount of noise in our measurement. Thus, we can simulate these periods as undergoing optical losses. As we want to minimize the losses experienced during the detection of our squeezing, we would ideally keep the pulse rise and fall times to a minimum.

We can begin modelling these losses with a simplified model of our pulse passing through our optical chopper. Suppose that we have a slit of width l rotating at speed ω at a distance of r from our disc center. We can approximate that $r \gg l$, and we have a uniform intensity over our beam cross section instead of gaussian. This allows us to express the pulse as composed of the segments shown in Figure 5.12

where

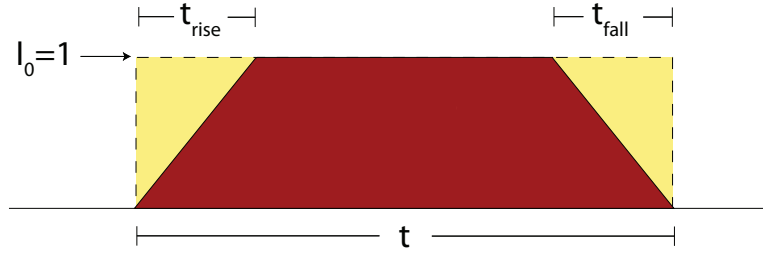


Figure 5.12: Model of a pulse generated by chopper with long rise and fall times. The normalized intensity I_0 falls below 1 for the periods t_{rise} and t_{fall} .

$$t_{rise} = t_{fall} = \frac{\omega_0}{\pi r f} \quad \text{and} \quad t = \frac{l + 2\omega_0}{2\pi r f}, \quad (5.16)$$

where f is the chopper rotation frequency and ω_0 is the beam radius. If we consider our optical losses experienced through the rise/fall times as time averaged losses over the entire detection period, we can derive a simple model of the losses by considering them as the difference between the time averaged intensity of an ideal pulse, and that of a real pulse

$$\text{losses} = I_0 \frac{t - \int_0^t \rho(t') dt'}{t}, \quad (5.17)$$

where the real pulse intensity envelope is given by a time dependent function $\rho(t)$. Now by normalizing our intensity to 1, and using our assumption of uniform cross section intensity, we can see that the losses evaluate to

$$\text{losses} = 1 - \frac{t - t_{rise}}{t} = 1 - \frac{l}{l + 2\omega_0} \quad \text{or} \quad \eta_{trans}^2 = \frac{l}{l + 2\omega_0}, \quad (5.18)$$

which shows that the losses only depend on our spot size relative to the aperture width. We can then use our loss expression in the beamsplitter model for losses to evaluate the loss effect on a given level squeezing using Equation 2.60

5.4.2.2 Real Pulse Envelope

With respect to using an optical chopper, preliminary calculations showed us that if we wanted to produce a pulse of 1 μs light, we could accomplish that by passing the light through a 50 μm slit, attached to a disc rotating at around 200 rotations per second.

We can develop a more realistic model for our pulse envelope $\rho(t)$ by dropping our assumption of a uniform beam intensity over the cross section. We can begin by expressing the intensity as a gaussian profile normalized to 1

$$I_0(r) = \sqrt{\frac{2}{\pi\omega_0^2}} e^{-\frac{2r^2}{\omega_0^2}}, \quad (5.19)$$

where r describes our distance from the beam center. We can then define the intensity of a beam after passing through the chopper, as I_{chop} , which is given by integrating our gaussian profile over our chopper slit width

$$I_{chop}(x) = \int_{x-l/2}^{x+l/2} I_0(r) dr. \quad (5.20)$$

We can then plot Equation 5.20 from the points before the beam enters the slit, until after it passes, to obtain a realistic profile of the effect of the chopper. Simulating this with a spot radius of $\omega_0 = 10\mu m$, a chopper frequency of 200 Hz, a disc radius of 46 mm, and a slit size of $50\mu m$ produces the pulse profile shown in Figure 5.13 with a $1\mu s$ width, conforming to our requirements.

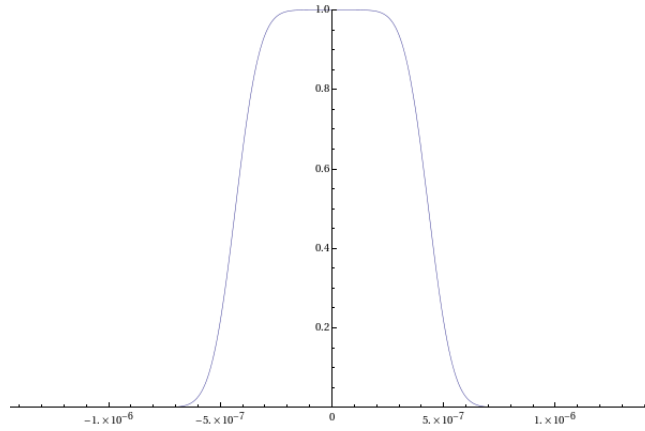


Figure 5.13: $1\mu s$ pulse modeled using gaussian intensity profile. Created by sending a $10\omega_0 = 10\mu m$ beam through a $50\mu m$ aperture on a $r=46$ mm disc rotating at 200 Hz.

5.4.2.3 Slit Selection

We thus choose to use a Thorlabs Fixed Vertical Slit, model S50R, similar to that shown in Figure 5.14. As these slits had a fabrication size of $50\mu m \pm 3\mu m$, they provided a much more reliable aperture size than we could produce on our own.

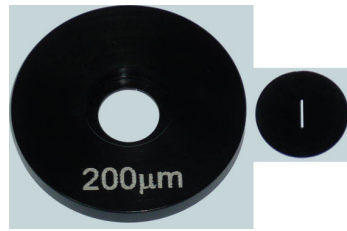


Figure 5.14: An example 200 μm Thorlabs slit, removed from its steel housing

5.4.2.4 Beam Focusing

In order to properly fit the beam through the slit, it needed to be highly focused. One danger of passing squeezed light through an aperture is that an improperly sized beam can have its squeezing destroyed due to diffraction losses. Given that we wanted to use a 50 μm slit, in order to lose less than 1% of power from diffraction losses, we calculated the waist size of the beam that could be passed through the slit of width D using [Siegman, 1986]

$$D = \pi\omega_0. \quad (5.21)$$

This indicated that a waist with a 10 μm radius would be sufficiently small. We purchased a high quality doublet lens from Newport with a focal length of $f = 38.7$ mm, which we used to focus the beam down to this size. We picked the doublet shape as to minimize the amount of aberrations that we would introduce onto the beam as any aberrations would make it difficult to obtain a high mode overlap upon recombination with the local oscillator. We mounted these lens onto a Newport M-UMR5.11 translating stage, so the could have micrometric control over the beam waist position. This proved critical, as the beam's waist had a sensitivity of a few mm.

5.4.2.5 Chopper Selection

With the slit selected, we needed to mount it to a rotating disc in order to create our optical chopper. We selected the Scitec instruments 310CD optical chopper, shown in Figure 5.15, which could rotate a disc up to 400 rps, thus twice our required speeds. Its specifications for stability indicated a $< 0.02\%$ variation in the chopper speed, which suggested that jitter would not be a problem for our experiment. The company provided solid un-machined discs, which we used to create our own custom disc design. Another important aspect, is that the chopper contained an integrated optical fork which output a TTL signal every time the disc would pass. This would allow us to signal the creation of an optical pulse, and prepare our experiment.

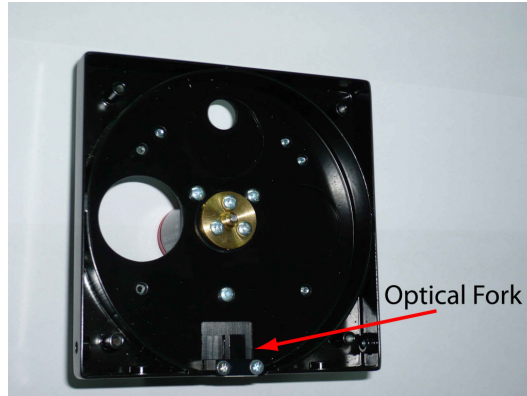


Figure 5.15: Scitec 310CD chopper with protective case opened to show optical fork.

5.4.2.6 Rotating Disc

We then sought to mount the slits onto the discs provided. For the memory experiment, we wanted the light to follow a particular on/off sequence. During a long period A, we wanted the squeezed beam to pass into the atoms, which would allow us to track the relative phase between the squeezed beam and the local oscillator. Then for a shorter period B, we wanted to cut off the squeezing creating a *dark time* in order to finalize the preparation of the MOT. Finally, we would present the actual pulse in C, after which the sequence would relaunch.



Figure 5.16: Optical squeezed vacuum pattern needed for storing a pulse in the quantum memory. We track the phase at A (25 ms), prepare the memory at B (100 μ s), and store the pulse at C (1 μ s).

Our proposed solution to create this sequence was to construct a slotted disc with protruding teeth. By placing the Thorlabs slit into the disc, the light could pass by the disc for the majority of the time, be blocked by the protruding tooth, and reappear when aligned with the tiny slit, producing the pulse.

5.4.2.7 Disc Balancing

As the disc was rotating at 200 rps, the slightest imbalance could introduce instabilities into its rotation, and thus create jitter. Thus, we constructed a symmetric disc having protrusions on both sides in order to maintain the balance.

Introducing a second slit to the disc preserves its balance, however because no two slits are exactly identical, the size of the pulse created from the second slit has no relation to the first, which means that we can't use both pulses for the experiment. The simplest solution that we developed was to just ignore the TTL produced from the second slit, so that it would not trigger the experiment. In Chapter 7, we will discuss the FPGA techniques used to create a TTL decimator, which allowed us to selectively ignore certain signals. As we only used one of the slits, we placed a $200\ \mu\text{m}$ slit into the second side in order to have a more versatile disc for experimenting with different pulse sizes.

5.4.2.8 Disc Geometry

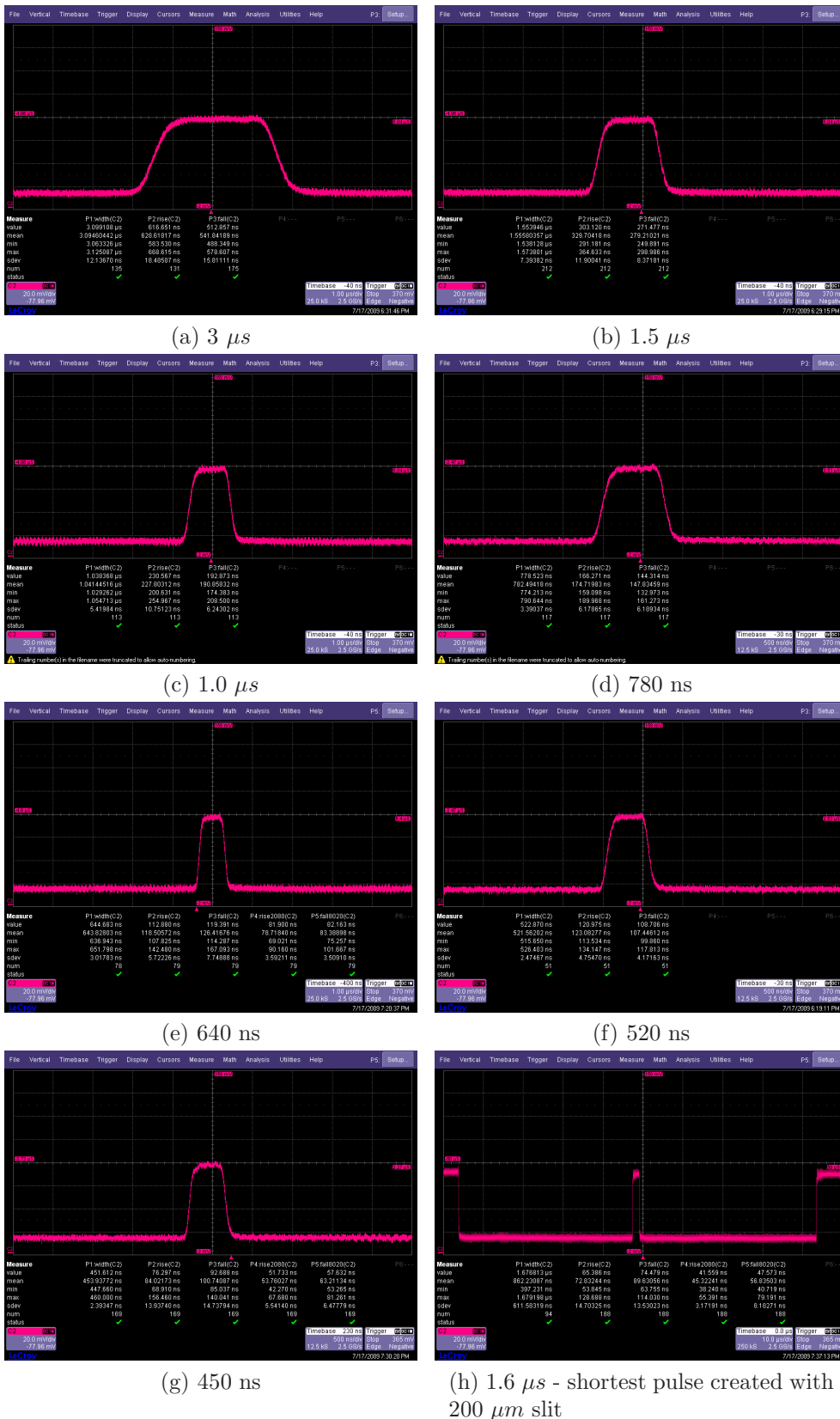
We determined that the slit needed to be placed at a 46 mm radius from the disc center, and that the tooth needed to cover an angle of 12.45° . This would allow us to produce pulses of around $1\ \mu\text{s}$, and dark periods of around $100\ \mu\text{s}$ for a 4 ms rotation period at 200 rps. We had the disc cut from our design shown in Appendix B by a commercial agency, and the end result produced the disc shown in Figure 5.17.



Figure 5.17: Customized disc designed to hold both $200\ \mu\text{m}$ and $50\ \mu\text{m}$ Thorlabs slits.

5.4.2.9 Pulse Measurements

We then mounted the chopper assembly and securely fastened it to the table, and locked the OPO with a seed beam injected so that we could directly observe the pulses produced on the squeezed light path. As the chopper's rotation speed and stability exceeded our initial estimated requirements, we managed to produce well-formed pulses with widths down to 450 ns. Furthermore, by comparing the pulse amplitude to the amplitude of the light not passing through the slit, such as in Figure 5.18h, we can see that our tight focusing allowed us to avoid any diffraction losses. The pulses shown in Figure 5.18 illustrate our results.

Figure 5.18: Optical pulses created using the $50 \mu\text{m}$ (a) - (g) and $200 \mu\text{m}$ slits (h)

Thus, the chopper did manage to create the stable short pulses that we required, however there were a few critical drawbacks.

5.4.2.10 Noise

Due to the chopper's high rate of speed, it created a large amount of noise which filled the entire room, disrupting other sections of the experiment. We tried to minimize this noise by using smaller holes to inject the light into the chopper, and we installed the entire apparatus in the plexiglass box shown in Figure 5.19 that was lined with lead and foam. This completely removed the noise at rotational speeds up to 600 Hz.

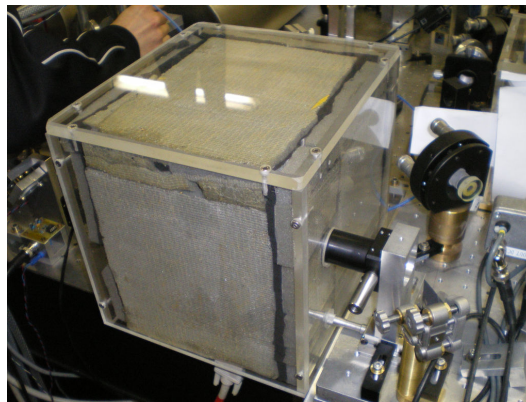


Figure 5.19: Plexiglass box used to attenuate the acoustic noise from the chopper. The interior of the box was coated with a foam/lead material to absorb the sound. Silent performance up to 600 Hz.

5.4.2.11 Vibrations

A more critical problem however, arose from the vibrations transmitted from the chopper to the table. This would be expected since the chopper was securely fastened to the table, however as a result, these vibrations prevented us from maintaining the OPO locked at resonance. We thus attempted to attenuate the vibrations by placing a sandwich of isolating material underneath the chopper as shown in Figure 5.20. Through trial and error, we chose a mixture of aluminum, lead, styrofoam and sorbothane, as well as placed sheets of lead beneath the OPO itself for increased attenuation.

5.4.2.12 Jitter

When using the chopper, the entire experiment needed to be triggered from the chopper pulse because the exact time when the pulse would be created was uncertain. This posed a problem because as stated earlier, EIT storage required us to have a



Figure 5.20: Isolation sandwich used to attenuate chopper vibrations, consisting of aluminum, lead, styrofoam, and sorbothane.

100 ns predictability of the pulse arrival time. Despite our successes in removing the acoustic noise and attenuating the chopper vibrations, problems of pulse jitter re-rose and proved to be a final problem. When we fixed the chopper rigidly to the table, the jitter was on the order of several ns. However, when we used the isolation to attenuate the mechanical vibrations, we could no longer securely fasten the chopper to the table, and thus its movement created pulse jitter of 500 ns. This uncertainty was much too large for us to properly use the EIT protocol, and it made it impossible for us to predict to within 100 ns when the next pulse would arrive - thus ruining the timing for the pulse detection and triggering the experiment.

Publication

Reproduction of article published in Optics Express:

S. Burks, J. Ortalo, A. Chiummo, X. Jia, F. Villa, A. Bramati, J. Laurat, and E. Giacobino, "Vacuum squeezed light for atomic memories at the D_2 cesium line," Opt. Express 17, 3777-3781 (2009).

Vacuum squeezed light for atomic memories at the D_2 cesium line

Sidney Burks, Jérémie Ortalo, Antonino Chiummo, Xiaojun Jia,
Fabrizio Villa, Alberto Bramati, Julien Laurat, Elisabeth Giacobino

Laboratoire Kastler Brossel, Université Pierre et Marie Curie, Ecole Normale Supérieure,
CNRS, Case 74, 4 place Jussieu, 75252 Paris Cedex 05, France

elg@spectro.jussieu.fr

Abstract: We report the experimental generation of squeezed light at 852 nm, locked on the Cesium D_2 line. 50% of noise reduction down to 50 kHz has been obtained with a doubly resonant optical parametric oscillator operating below threshold, using a periodically-poled KTP crystal. This light is directly utilizable with Cesium atomic ensembles for quantum networking applications.

© 2010 Optical Society of America

OCIS codes: 270.0270 Quantum Optics, 270.6570 Squeezed states, 190.4970 Parametric oscillators and amplifiers.

References and links

1. H. Vahlbruch, M. Mehmet, S. Chelkowski, B. Hage, A. Franzen, N. Lastzka, S. Goler, K. Danzmann, R. Schnabel, "Observation of Squeezed Light with 10-dB Quantum-Noise Reduction", *Phys. Rev. Lett.* **100**, 033602 (2008).
2. P. Zoller *et al.*, "Quantum information processing and communication, Strategic report on current status, visions and goals for research in Europe", *Eur. Phys. J. D* **36**, 203-228 (2005).
3. N.J. Cerf, G. Leuchs, E.S. Polzik eds, *Quantum Information with Continuous Variables*, (World Scientific Publishing, New Jersey, 2007).
4. H.J. Kimble, "The quantum internet", *Nature* **453**, 1023-1030 (2008).
5. T. Tanimura, D. Akamatsu, Y. Yokoi, A. Furusawa, M. Kozuma, "Generation of squeezed vacuum resonant on a rubidium D_1 line with periodically poled KTiOPO₄", *Opt. Lett.* **31**, 2344-2346 (2006).
6. G. Hetet, O. Glockl, K.A. Pilypas, C.C. Harb, B.C. Buchler, H.A. Bachor, P.K. Lam, "Squeezed light for bandwidth-limited atom optics experiments at the rubidium D_1 line", *J. Phys. B: At. Mol. Opt. Phys.* **40**, 221-226 (2007).
7. K. Honda, D. Akamatsu, M. Arikawa, Y. Yokoi, K. Akiba, S. Nagatsuka, T. Tanimura, A. Furusawa, M. Kozuma, "Storage and Retrieval of a Squeezed Vacuum", *Phys. Rev. Lett.* **100**, 093601 (2008).
8. J. Appel, E. Figueroa, D. Korystov, M. Lobino, A. I. Lvovsky, "Quantum memory for squeezed light", *Phys. Rev. Lett.* **100**, 093602 (2008).
9. E.S. Polzik, J. Carri, H.J. Kimble, "Spectroscopy with squeezed light", *Phys. Rev. Lett.* **68**, 3020 (1992).
10. F. Villa, A. Chiummo, E. Giacobino, A. Bramati, "High-efficiency blue-light generation with a ring cavity with periodically poled KTP", *J. Opt. Soc. Am. B* **24**, 576-580 (2007).
11. D.A. Shaddock, M.B. Gray, D.E. McClelland, "Frequency locking a laser to an optical cavity by use of spatial mode interference", *Opt. Lett.* **24**, 1499 (1999).
12. R. W. P. Drever, J. L. Hall, F. V. Kowalski, J. Hough, G. M. Ford, A. J. Munley and H. Ward, "Laser phase and frequency stabilization using an optical resonator", *Appl. Phys. B* **31**, 97 (1983).
13. C. Fabre, S. Reynaud, in *Fundamental Systems in Quantum Optics*, Les Houches 1990, J. Dalibard, J. M. Raimond, J. Zinn-Justin, Eds. (Elsevier, Amsterdam, 1992)
14. H.J. Kimble, in *Fundamental Systems in Quantum Optics*, Les Houches 1990, J. Dalibard, J. M. Raimond, J. Zinn-Justin, Eds. (Elsevier, Amsterdam, 1992)

During the last two decades, a great effort has been dedicated to the generation of non-classical states of light in the continuous variable regime. Very recently, 10 dB of noise reduc-

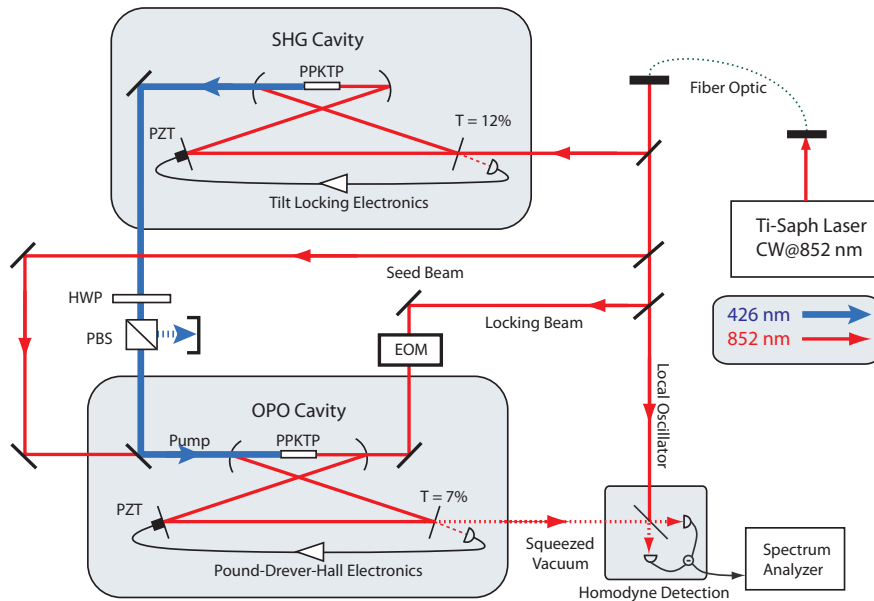


Fig. 1. Experimental Setup. A Ti:sapphire laser locked on resonance with the Cesium D_2 line is frequency doubled. The second harmonic is then used to pump a doubly resonant optical parametric oscillator below threshold. The seed beam is used for cavity alignment and blocked during measurements. HWP: Half-wave plate. EOM: electro-optic phase modulator. PZT: piezo-electric transducer. PBS: polarizing beam-splitter.

tion was obtained with the goal of surpassing the standard quantum limit for sensitive measurements such as gravitational wave detection.¹ Driven by the prospect of interfacing light and matter for quantum networking applications,²⁻⁴ ongoing efforts have also focused on the generation of squeezed light at atomic wavelengths and reaching low noise frequencies to be compatible with bandwidth-limited interfacing protocols. Results have been obtained on the rubidium D_1 line^{5,6} and squeezed light has been recently stored.^{7,8} Squeezing resonant with the cesium D_2 line was demonstrated already in 1992 but not at low frequency sidebands.⁹ We describe here the generation of such squeezing compatible with cesium-based bandwidth-limited networking protocols.

The experimental setup is sketched in Figure 1. A continuous-wave Ti:Sapphire laser (Spectra Physics-*Matisse*) locked on the cesium D_2 line is frequency-doubled in a bow-tie cavity with a type-I 20 mm long periodically-polled KTP crystal (PPKTP, Raicol Crystals Ltd.),¹⁰ and locked by tilt-locking.¹¹ By supplying 600 mW of light at 852 nm, we obtain 200 mW of 426 nm cw-light. Higher doubling efficiency can be obtained but with lower stability due to thermal effects. This beam pumps a 550 mm long doubly-resonant optical parametric oscillator (OPO), based on a 20 mm long PPKTP crystal. The OPO is locked at resonance using the Pound-Drever-Hall technique¹² (20 MHz phase modulation), thanks to a 8 mW additional beam injected through a HR mirror and propagating in the opposite direction of the pump beam. The crystal temperatures are actively controlled, with residual oscillation of the order of few mK. Both cavities have the same folded-ring design. The crystals are placed between high-reflecting mirrors with a radius of curvature $R=100$ mm for the OPO, and $R=150$ mm for the doubler while the other mirrors are flat. The input mirror for the doubler has a transmission of 12%, and

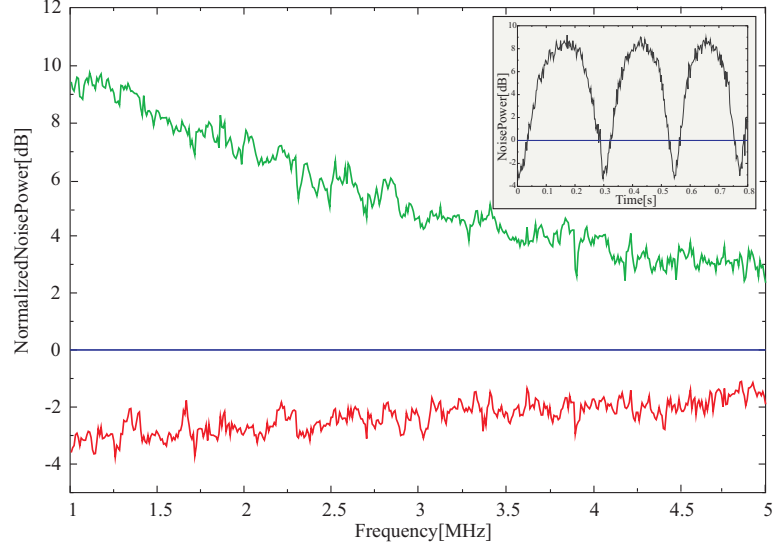


Fig. 2. Normalized noise variance for the squeezed and anti-squeezed quadratures, from 1 MHz to 5 MHz. The inset gives the noise variance at 1.5 MHz while scanning the phase of the local oscillator. The resolution bandwidth is set to 100 kHz and the video bandwidth to 100 Hz.

the output mirror for the OPO of 7%. The folding angles are around 10° , with a cavity length of 55 cm. The waist inside the crystal is around $46 \mu\text{m}$. In this configuration, the OPO threshold is measured to be 90 mW, with a degeneracy temperature at 46.3°C . The homodyne detection is based on a pair of balanced high quantum efficiency Si photodiodes (FND-100, quantum efficiency: 90%) and an Agilent E4411B spectrum analyser. The light from the Ti:Sapphire laser is used after initially being transmitted into a single mode fiber, which improves the matching of the cavities and enables a high contrast for the homodyne detection interference. The fringe visibility reaches 0.96. The shot noise level of all measurements is easily obtained by blocking the output of the OPO. Let us emphasize that the pump is matched to the OPO cavity by temporarily inserting mirrors reflective at 426 nm and thus creating a cavity resonant for the blue pump. This solution turns out to be very efficient.

Figure 2 gives the noise variances of the squeezed and anti-squeezed quadratures for a frequency spectrum from 1 to 5 MHz. The inset shows the noise variance while scanning the local oscillator phase for a fixed noise analysis frequency of 1.5 MHz. For these measurements, the blue pump power was set to 75 mW. 3 dB of squeezing is obtained, with an excess noise on the anti-squeezed quadrature around 9 dB. This noise reduction value has to be compared to the theoretical value V given by^{13,14}

$$V = 1 - \frac{T}{T+L} \frac{4\sigma}{(1+\sigma)^2 + 4\Omega^2} \quad (1)$$

where T is the output coupler transmission, L the additional intra-cavity losses due to absorption or scattering, Ω the analysis frequency normalized to the cavity bandwidth (10 MHz) and σ the amplitude pump power normalized to the threshold. By taking $\sigma = 0.9$, $\Omega = 0.1$, $T = 0.07$ and $L = 0.03$ (determined by measuring the cavity finesse and mirror transmissions), the expected value before detection produced at the OPO output is -5 dB. Let us note that L is mostly due to absorption in PPKTP at this particular wavelength, as no pump-induced losses were measured.

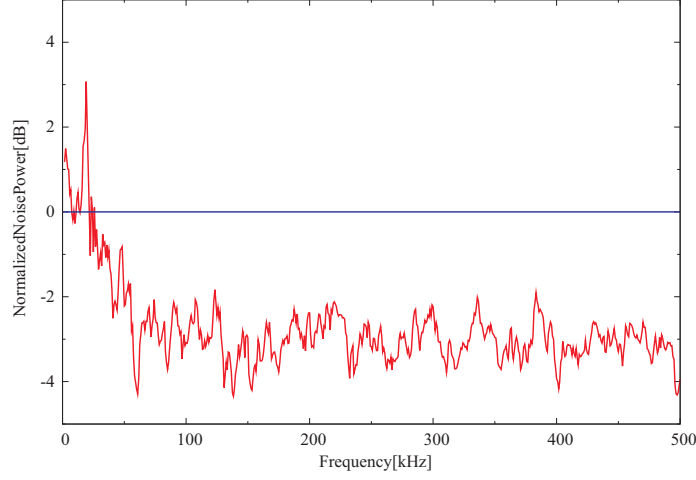


Fig. 3. Normalized noise variance up to 500 kHz after correction of the electronic noise. The resolution bandwidth is set to 30 kHz and the video bandwidth to 36 Hz.

The detector quantum efficiency is estimated to be 0.90, the fringe visibility is 0.96 and the propagation efficiency is evaluated to be around 0.95. These values give an overall detection efficiency of $0.9 \cdot 0.96^2 \cdot 0.95 \simeq 0.8$. After detection, the expected squeezing is thus reduced to -3.5 dB, in good agreement with the experimental values.

Figure 3 shows the broadband noise reduction similar to the Figure 2 insert, but now for a lower frequency range, between 0 and 500 kHz. Squeezing is expected to be higher in this range, but technical noise results in its degradation. The stability of the setup and noise of the laser are important parameters here. In particular, the seed beam power needs to be decreased as much as possible to avoid noise coupling into the device. In our setup, squeezing is finally detected down to 25 kHz, and 3 ± 0.5 dB are observed for the 100-500 kHz frequency range. Measurements are corrected from the electronic dark noise. The presence of low-frequency sideband squeezing is a requisite for future quantum networking applications such as the storage of squeezed light by EIT, where the transparency window width is a limiting factor.^{7,8}

In conclusion, we have demonstrated the generation of squeezed light locked on the D_2 cesium line. More than 3 dB of noise reduction has been obtained and the squeezing is preserved for sideband frequencies down to 25 kHz. This ability opens the way to further investigations of light-matter interface using cesium atomic ensembles, like EIT or Raman storage of non-classical state of light in the continuous variable regime.

Acknowledgments

This work was supported by the French ANR under the PNANO contract IRCOQ and by the EU under the projects COVAQIAL and COMPAS. Xiaojun Jia acknowledges support from La Ville de Paris. We would like to thank J. Cviklinski for useful discussions in the early stage of the experiment.

Part III

Preparation of a Quantum Memory With Cold Atoms

Experimental Tools for the Storage of Squeezed Light

Contents

6.1 Introduction	98
6.1.1 Optical Storage Through EIT	98
6.2 Phase Lock	99
6.2.1 Theory	100
6.2.2 Experimental Setup	102
6.2.3 Analysis	107
6.3 The Magneto-Optical Trap	107
6.3.1 Basic Trapping Principles	108
6.3.2 MOT Characteristics	109
6.3.3 Laser Sources	110
6.3.4 Controlling the Magnetic Field	112
6.3.5 Timing	118
6.4 Optical Layout	120
6.4.1 Beam Displacers	123
6.4.2 Signal Beam	124
6.4.3 Local Oscillator	124
6.4.4 Control Beam	124
6.4.5 Auxiliary Beam	125

6.5	Optical Density Measurements	125
6.5.1	Implementation	126
6.6	Raman Scheme for the Compensation of the Magnetic Field	127
6.6.1	Raman Spectroscopy	129
6.6.2	Labview Interface	130
6.7	Conclusion	131

6.1 Introduction

Over the last several years, our group has focused on the development of a quantum memory in Cesium. The idea is based on using EIT to carry out a reversible transfer of the quantum fluctuations of light onto the transverse spin components of an ensemble of Cesium atoms. The theory describing this approach was developed during the thesis of Aurelien Dantan [Dantan, 2005]. During the work carried out afterwards by Jean Cviklinski [Cviklinski, 2008] and Jeremie Ortalo [Ortalo, 2009], a memory was developed using warm Cesium vapor where the Zeeman sublevels served as the fundamental levels for EIT. This work resulted in showing that we could carry out a noiseless storage and retrieval of coherent states. As the Zeeman sublevels are closely spaced in frequency, we have focused our next memory implementation on using the hyperfine transitions for EIT, which will allow us a much finer frequential resolution for the signal and control transitions.

In this chapter, we will discuss our development of this new implementation of a quantum memory, and describe the experimental elements needed to store squeezed light onto a cold Cesium vapor. Our main goal for this implementation of the memory is to show that we can achieve the storage and retrieval of squeezed vacuum states using the cold atomic medium. Once we accomplish this, we can create entangled beams from our squeezed vacuum, and store these entangled states into separate regions of our ensemble. Accomplishing this goal will show that it is possible to create a quantum memory which can function as the core component in a quantum repeater network.

As this work takes a departure from our previous experimental approaches, it requires us to develop new tools and techniques before we will have system that is usable for storage. In the following sections, we will discuss the individual components that were assembled in order to advance our progress towards a working quantum memory.

6.1.1 Optical Storage Through EIT

As stated earlier, the storage mechanism that we will use for this experiment is EIT [Harris, 1997]. For this method, we use the 3-level Λ system shown in Figure 6.1,

where the fundamental levels are the $F=3$ and $F=4$ hyperfine states, and the excited level is the $F'=4$ state. Our atoms will be initially prepared by pumping them into the $F=4$ state. We will then use the $F=3 \rightarrow F'=4$ transition for our control beam to dress the $F'=4$ level. We then tune our signal pulse on the $F=4 \rightarrow F'=4$ transition, and as it is not resonant with the dressed $F'=4$ level, this leads to a transparency for our signal. Once the signal pulse has entered the atomic ensemble, we extinguish the control beam to trap the signal pulse for a small time period, which is the memory storage time. We then reactive the control beam to release the signal pulse, and read the stored state from the memory.

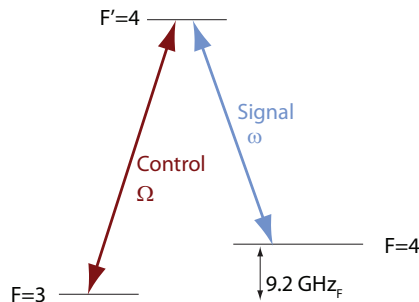


Figure 6.1: Transitions used to carry out EIT in Cesium for the quantum memory. The $F=3$ and $F=4$ hyperfine levels serve as the ground states, with an $F'=4$ excited state. A control beam $F=3 \rightarrow F'=4$ controls the transparency of the atomic ensemble, while a signal is encoded onto the $F=4 \rightarrow F'=4$ beam.

6.2 Phase Lock

When carrying out experiments with atoms involving atomic coherence effects, it is necessary that the lasers used to probe the atomic transitions possess a narrow linewidth and a high optical coherence with each other [Hockel *et al.*, 2009]. Specifically with EIT, changes in the laser linewidth can affect the EIT transparency and our ability to slow down and store light [Lu-Ming *et al.*, 2008].

Typically when performing EIT, if we are studying the coherence effects between transitions having a small frequency difference, such as the Zeeman sublevels, the frequency range is small enough to allow us to probe the levels using one main source laser. We can accomplish this by passing a fraction of the laser through an AOM or EOM, and thus create a second frequency shifted beam on output. This shifted beam will have the highest possible degree of coherence with the original beam, as they both originate from the same laser source.

For probing the hyperfine levels of Cesium however, the 9.2 GHz frequency separation is far too large to achieve efficiently using an AOM. Large band EOMs are

available, but their high costs and low efficiencies prevent us from using this option to directly create an intense frequency shifted beam.

For this case, it is simpler to use two separate lasers to explore the two transitions. For our experiment, we decided to tune the Matisse laser to the $F=4 \rightarrow F'=4$ signal transition, and use a separate diode slave laser for the $F=3 \rightarrow F'=4$ control beam. In order to preserve the coherence between the two lasers, we need to develop a way to lock them in phase such that the relative change of phase between the master laser and the slave laser rests locked at a fixed beat frequency. To accomplish this phase lock, we have developed an Optical Phase Locked Loop (OPLL) as a feedback system to lock the diode laser to the Matisse.

6.2.1 Theory

In order to understand how the OPLL functions, we can begin by analyzing the simpler electronic PLL on which it is based [Curtin and O'Brien, 1999]. We begin by sending our PLL a signal frequency from a voltage-controlled oscillator (VCO), and a reference frequency to which we wish to lock the VCO and reduce its linewidth. We take these two signals and compare them using a phase-frequency detector (PFD), which outputs an error signal based on their phase and frequency difference. We then filter this error signal using a low-pass loop filter, which must be properly tuned to the system [Abramovitch, 2002], and we use the output from this filter as feedback to control the VCO frequency. We can optionally pass the VCO feedback through a frequency divider if we need to run the VCO at a much higher rate than the reference frequency. When the circuit is activated, the VCO locks its frequency to the reference frequency at a reduced linewidth. The block diagram in Figure 6.2 illustrates this operation.

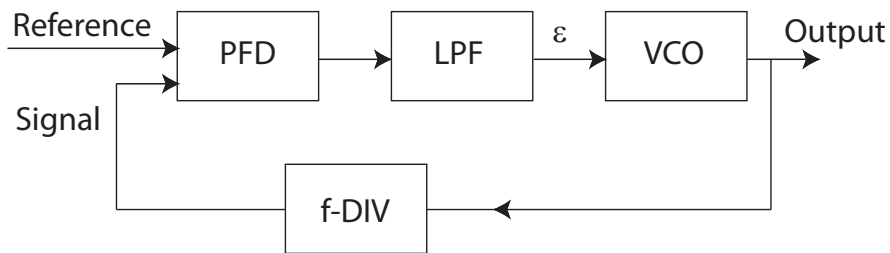


Figure 6.2: A typical PLL is composed of a phase-frequency detector (PFD), low-pass filter (LPF), voltage-controlled oscillator (VCO), and frequency divider (f-DIV). The VCO signal is fed back into the PFD for comparison to the reference signal

$$S(t) = A_1 \sin(\omega_1 t + \phi_1(t)) = A_1 \sin(\Phi_1) \quad (6.1)$$

$$R(t) = A_2 \sin(\omega_2 t + \phi_2(t)) = A_2 \sin(\Phi_2) \quad (6.2)$$

If we imagine our signal and reference as two periodic signal $S(t)$ and $R(t)$, engaging the phase lock assures a fixed relationship between our signal arguments, such that

$$\Phi_1 = \Phi_2. \quad (6.3)$$

Given this description of a PLL, there are two core components which must be properly adjusted in order to optimize the system - the phase-frequency detector, and the loop filter.

6.2.1.1 Frequency Division

The PLL response is limited to its reference signal's input frequency, but often we wish to run a VCO at a much higher frequency. We can accomplish this by adding a frequency divider to the VCO output. By dividing the VCO signal frequency to a lower value closer to the reference frequency, we can compare the reference and signal frequencies without artificially slowing down our VCO.

Additionally, we can consider this division as a type of *gain* on our PLL control signal. By dividing the VCO output by n , the PLL can use the same voltage to correct for a range of n times the reference frequency, as opposed to only correcting for a range around the reference frequency without a divider. This can potentially increase the loop performance by allowing us to use small control signal voltages for a large response.

6.2.1.2 Phase-Frequency Detection

There are several methods of creating phase detector for signal comparison. For our design, we use an all-digital PFD. This system is composed of a set of digital flip-flops which execute the logic shown in Figure 6.3 [On Semiconductor, 2006].

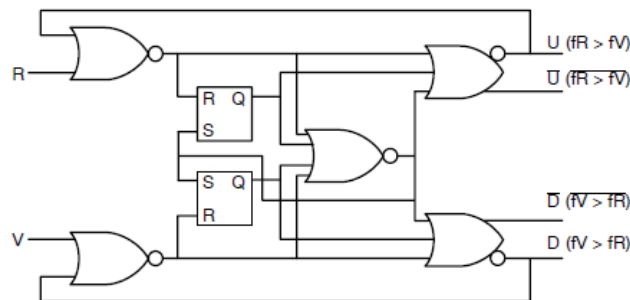


Figure 6.3: Logic diagram for the all-digital phase-frequency detector used in our PLL. Phase and frequency changes in the reference (R) and signal (V) inputs cause digital state changes on the U, \bar{U} , D, and \bar{D} outputs, allowing us to create an error signal.

A digital PFD takes a reference (R) and VCO (V) signal as input, and outputs four signals based on their phase or frequency difference. By subtracting either the positive (U-D) or negative ($\bar{U}-\bar{D}$) signals, we can receive an error signal on the output, as is shown in Figure 6.4 [On Semiconductor, 2006]. The error signal output from the PFD is proportional to the frequency and phase error of our input.

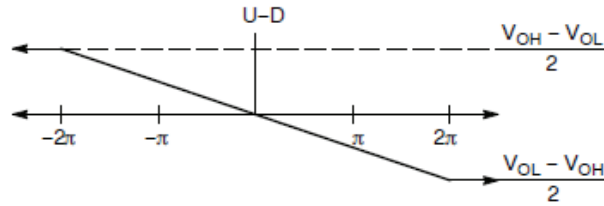


Figure 6.4: Output voltage as a function of phase Φ from a PFD after subtracting the $U - D$, or $\bar{U} - \bar{D}$ outputs.

6.2.2 Experimental Setup

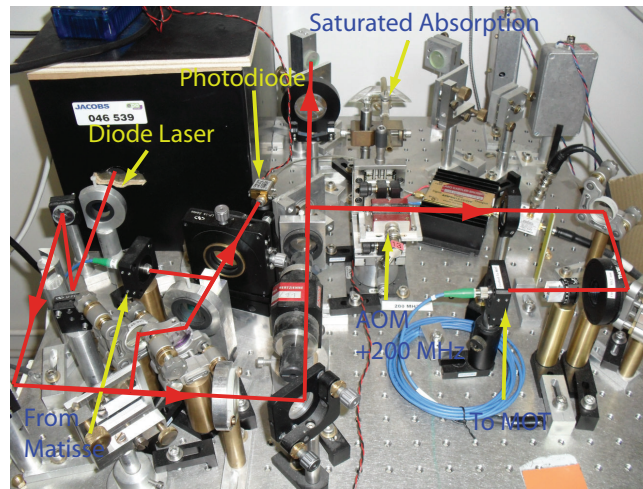


Figure 6.5: Photo of optical table used for the OPLL.

Creating an Optical PLL follows the exact same procedure as a traditional PLL. Instead of using a VCO, we use the beat signal generated from the optical interference of our slave and master lasers, and we use the filtered error signal to adjust the frequency tuning of the slave laser. We have three main methods to adjust the frequency of a slave laser: changing the cavity length, changing the diode temperature, or modulating the injection current. The current modulation approach has the fastest response and allows for the largest loop bandwidth, so we use this approach.

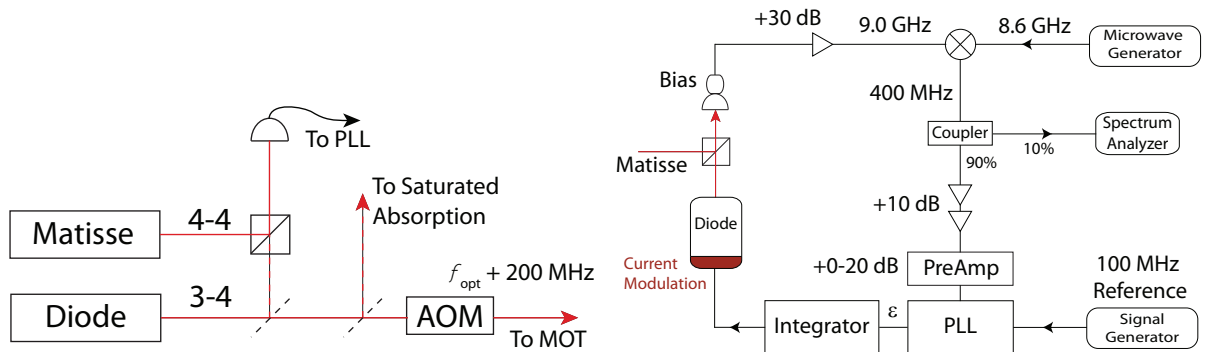


Figure 6.6: Optical and electronic block diagrams for our OPLL implementation

Figure 6.6: Optical and electronic block diagrams for our OPLL implementation

Figure 6.6a shows the optical layout of our phase-locking system pictured in Figure 6.5. Our setup begins with us creating a beat signal from the interference of the Matisse and diode lasers. To accomplish this, we combine a few mW of light from the Matisse with an equal amount of light from the diode on a non-polarizing beam splitter. The two light sources are aligned to have the same matching and polarization. We then send the light into a Hamamatsu photodiode which is powered by a 9V battery, and biased with a Minicircuits ZX85-12G-S+ Bias Tee with a 12 GHz bandwidth. The usage of a battery allows us to minimize the electronic noise in the photodiode.

Next, we lock the Matisse to the 4-4 transition, and manually adjust the diode laser so that it is near the 3-4 transition, and separated by approximately 9.0 GHz. We lock at 9.0 GHz instead of 9.2 GHz because we pass our diode laser through an AOM before sending it on to the MOT. The AOM adds the remaining 200 MHz offset we need to reach 9.2 GHz, and allows us to easily create pulses of this light.

The optical interference of the two lasers creates a beat note which is detected by the biased photodiode, as shown in Figure 6.6b. By adjusting the optical power, we amplify the beat note power up to around 0 dBm. We then send the photodiode output to an Amplicial AMP8G12-33 amplifier where it is amplified by 30 dB and then sent to a Minicircuits ZMX-10G+ mixer. We demodulate the note with a microwave 8.6 GHz signal generated by a HP 8672A signal generator. This allows us to mix down the optical beat note to 400 MHz, allowing us to observe it on our low-frequency spectrum analyzer as shown in Figure 6.7. This is convenient because we can from this point on, avoid using high-frequency RF components in our electronics chain, and use a simpler

low-frequency setup.

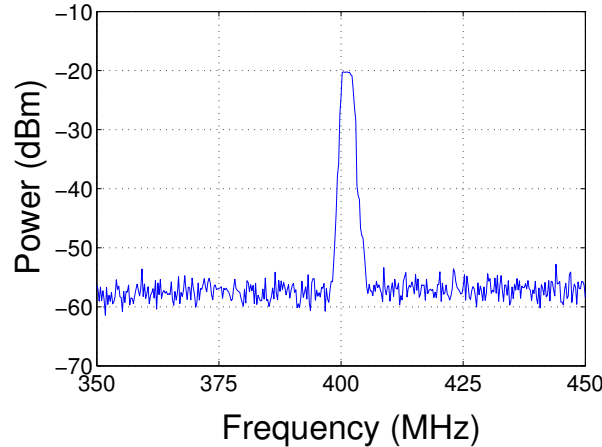


Figure 6.7: Optical beat note between Matisse and diode lasers demodulated to 400 MHz.

Once we have the 400 MHz beat note, we use a Minicircuits ZFDC-10-2 directional coupler to extract 10% of the signal and send it to a spectrum analyzer which permits observation of the lock. The remaining 90% continues on to two ZFL-500LN-BNC amplifiers, which give a total amplification of 10 dB, and then on to a homemade wideband 0-400 MHz preamplifier circuit which amplifies the signal by up to an additional 20 dB. We then send the beat note to our phase-frequency detection circuit, which creates the error and modulation signal that we then use to lock the diode. The last step in our chain involves passing the modulation signal through the integrating circuit shown in Figure 6.10a, which acts as our loop filter. We then send this integrated output directly into the current modulation input for the diode laser.

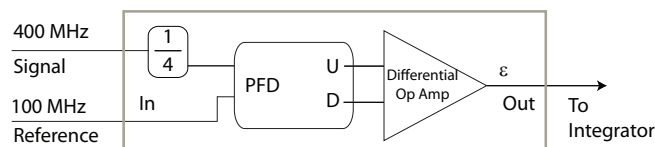


Figure 6.8: Block diagram showing our PLL functionality. The 400 MHz signal is divided by 4, and compared to a 100 MHz reference with the PFD. A differential op-amp subtracts the PFD outputs to create the error signal.

Figure 6.8 depicts the operation of our PLL circuit pictured in Figure 6.9. For our reference signal, we use a 100 MHz signal generated by an Agilent E4420b generator. Our 400 MHz beat note enters the PLL circuit where it is divided by 4 using an ON Semiconductor MC12093 divider, and the divided signal and our reference are compared using an ON Semiconductor MCH12140 PFD. The PFD outputs signals on its U and

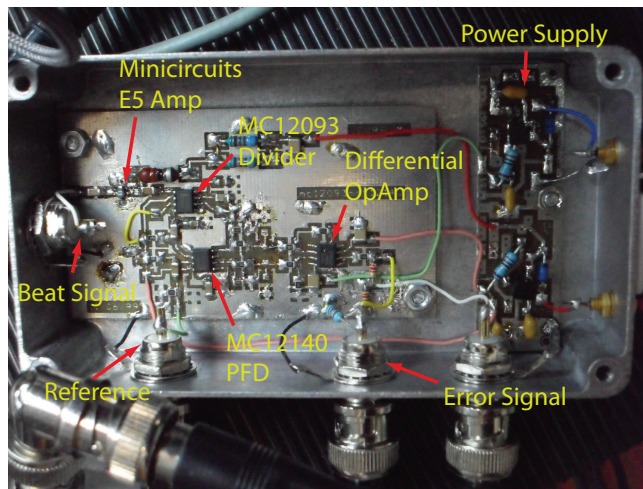
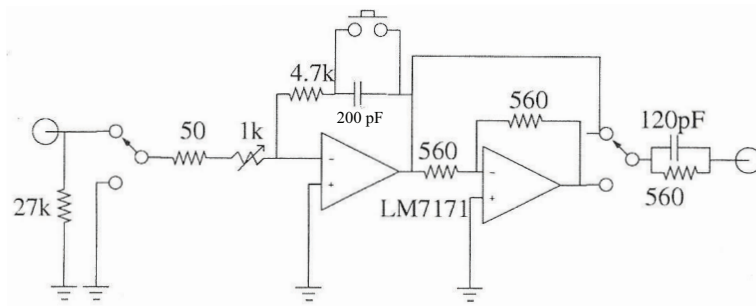


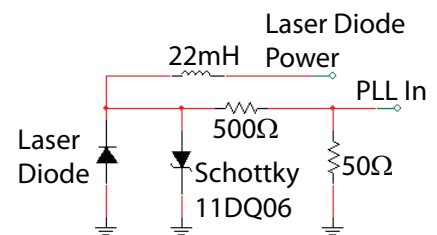
Figure 6.9: Photo of actual OPLL circuit with notable features marked.

D outputs which we then subtract using a differential operational amplifier (opamp). The opamp then outputs the error signal, which we send directly to the integrator circuit for low-pass filtering.

In order to interface the filtered modulation signal with the laser diode, we use the current divider circuit shown in Figure 6.10b to limit the current applied by our PLL circuit. This allows us to avoid destroying the laser by applying too much modulation current.



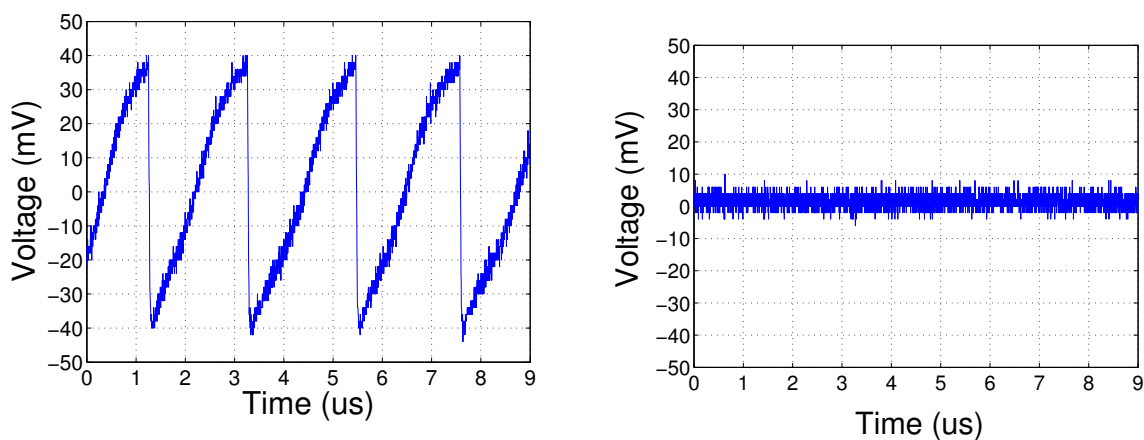
(a) PLL integrator circuit.



(b) Diode current modulation interface.

Figure 6.10: (a) Circuit Diagram for PLL Integrator (b) Current modulation circuit to interface PLL with diode laser. The current divider protects the diode from too much modulation current.

Using this setup, once we tune the diode laser to place the beat signal near the reference frequency, we can observe the error signal take the form in Figure 6.11a, which resembles the logic diagram output in Figure 6.4.

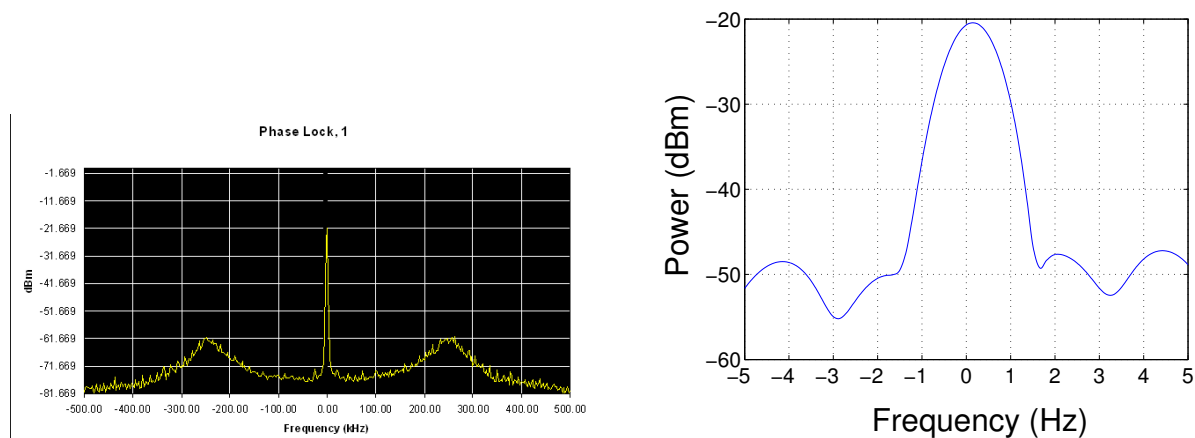


(a) OPLL error signal as the beat signal approaches the lock point. We see that this resembles the output shown in Figure 6.4.

(b) Error signal goes to zero when we engage the OPLL lock.

Figure 6.11: PLL error signal as we a) approach the lock point and b) engage the lock.

At this point when we engage the phase lock, the slave laser locks to the Matisse and the optical beat note produces the noise trace shown in Figure 6.12.



(a) Diode laser phase-locked to the Matisse at a 9.0 GHz frequency offset. The majority of the power is held within the central peak. This system maintains a lock for over 10 hours, and is only sensitive to the slow long-term stability drifts.

(b) Zoom of central peak with 10 Hz span, 1 Hz VBW and RBW. This zoom shows that our system maintains a frequency lock with a precision of better than 1 Hz. Our resolution of the ultimate lock precision is limited by the spectrum analyzer.

Figure 6.12: Phase lock results

6.2.3 Analysis

In order to quantify the quality of the phase lock, we can use the mean-square error of the phase noise. This quantity is defined as the ratio of power in our beat signal at its center frequency, and the power integrated over all frequencies. We take the center frequency power as simply the height of our central peak given by the spectral analyzer.

We can derive this quantity by defining the noise density as was done earlier for the electric field, and as is seen in [Zhu and Hall, 1993]. We begin by defining the E field of our laser as

$$E(t) = A(t)e^{-i\omega_0 t - i\phi t}, \quad (6.4)$$

where $A(t)$ is the instantaneous field amplitude, and $\phi(t)$ is the phase modulation. We have an instantaneous angular frequency given by

$$\omega(t) = \omega_0 + \frac{d\phi(t)}{dt}. \quad (6.5)$$

We can write the autocorrelation function of our field as

$$R_\epsilon(\tau) \equiv \langle E(t)E^*(t + \tau) \rangle, \quad (6.6)$$

and by taking the Fourier transform, we can obtain

$$P_\epsilon(\tau) = \frac{1}{2\pi} \int_{-\infty}^{\infty} P_\epsilon(\omega) d\omega \quad (6.7)$$

We can find the mean square noise error by measuring the fraction of the power contained at our lock frequency with respect to the total power

$$\exp(-\langle \Delta\phi^2 \rangle) = \frac{P_0}{\int_{-\infty}^{\infty} P(\omega) d\omega} \quad (6.8)$$

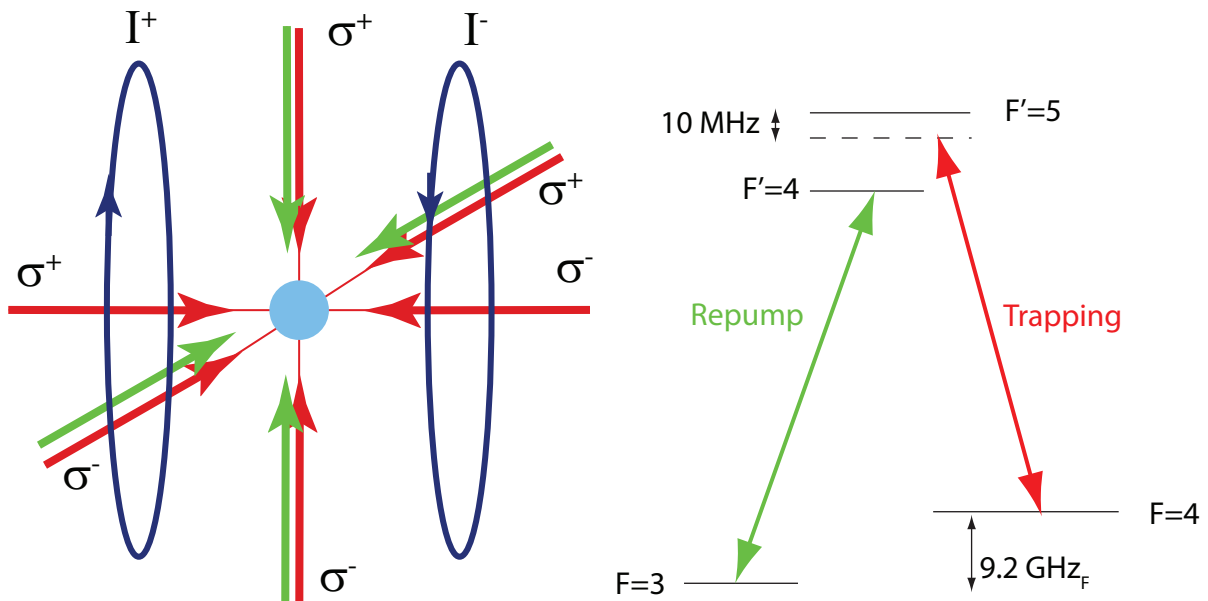
Equation 6.8 allows us to establish a quantitative measure of the phase noise contained in the lock by using a spectrum analyzer to measure the power contained in the peak, and the total integrated power [Appel *et al.*, 2009].

6.3 The Magneto-Optical Trap

The principle component of this experiment is the MOT itself which contains our trapped atoms. We will begin by describing the characteristics of the MOT, and the experimental elements that allow us to prepare a dense atomic cloud inside of it.

6.3.1 Basic Trapping Principles

In order to trap our atoms inside the MOT, we need to create a system for cooling and confining the atoms in a small region. We first require three pairs of counter-propagating beams, where one pair of beams is aligned with each spatial axis. The beams are circularly polarized such that two pairs take a σ^+ polarization, and one pair takes a σ^- polarization. These trapping beams are detuned from the $F=4 \rightarrow F'=5$ Cesium cycling transition by 10 MHz. This detuning from resonance allows us to use the Doppler effect to apply a velocity-dependant braking force to the atoms, and thus create an optical molasses at the point where the beams meet at the center of the MOT.



(a) We require three circularly polarized beams to create the optical molasses, and a magnetic field gradient to confine the atoms. A repump beam is superposed with the trapping beam along two axes.

(b) Optical transitions used for the trapping and repumping beams in the MOT. The trapping beam is detuned by 10 MHz from the $F=4 \rightarrow F'=5$ transition. The repumping beam is resonant with the $F=3 \rightarrow F'=4$ transition.

Figure 6.13: Requirements for building a MOT. Converging beams and magnetic field gradients trap the atoms when we use the $F=4 \rightarrow F'=5$ trapping transition.

As some of the atoms relax into the $F=3$ state, we also require a repump beam for the $F=3 \rightarrow F'=4$ transition, so that we can repump these atoms into the $F=4$ state allowing us to retrap them. We overlap two of these repump beams with two of the trapping beams described earlier. Figure 6.13b depicts the 3-level diagram that shows the relevant transitions needed for creating the molasses.

Once the optical molasses is created, we also need to apply a magnetic field gradient so that we can confine the atoms to a small region. We supply the MOT chamber with the necessary beams via fiber optic, which prevents the beams from disaligning on a day-to-day basis.

In the following sections, we discuss the experimental setup that we developed in order to fulfill these requirements and create our atomic ensemble.

6.3.2 MOT Characteristics

For the trap itself, we selected a glass chamber with 7 viewports on its sides, as shown in Figure 6.14a. This allows us a large flexibility in how we inject our beams into the chamber. We inject the trapping beams through the opposing windows to create an optical molasses in the chamber center. In order to create the magnetic field, we wound 120 loops of copper wire into coils around circular Teflon frames, which had a radius of 10 cm. The coils were positioned at each side of the trap and fixed to the table with brass posts. Brass was selected for the post material as it does not respond to magnetic fields. We typically sent 5A of current into the coils to create the fields. The chamber's glass composition also aids with respect to the magnetic field as it prevents the creation of Foucault currents when we cut off the field.



(a) Glass chamber used to create the MOT with multiple input ports.



(b) Atoms trapped at the center of the chamber

Figure 6.14: MOT Chamber used to trap the atomic ensemble.

We create an initial vacuum in the chamber by pumping the pressure down to 10^{-7} torr. At this point, we activate an ion pump which further decreases the pressure to 10^{-9} torr or lower.

Cesium atoms are injected into the chamber by means of a set of getters, which are Cesium filled wires that were installed inside of the chamber during its construction.

When we pass a strong current through these getters, they heat up to around 400°C , and begin to release their Cesium. We typically send around 5A of current through the getters, which yields the largest MOT with the highest density of atoms. Using this configuration, we have managed to trap an estimated 10^9 atoms.

6.3.3 Laser Sources

To create the beams at all of the necessary transitions, we developed a set of diode lasers and used them along with a Toptica Photonics BoostA Master Oscillator Power Amplifier (MOPA) to produce a high optical output for our trapping beam. The diodes used to create the laser transitions were constructed from designs developed at the Paris Observatory [Baillard *et al.*, 2006]. Figure 6.15b shows an example of one of the diodes. Their bodies consist of a monolithic aluminum alloy, inside of which we fix two mirrors to create a linear cavity. An interferential filter placed between the mirrors serves as the frequency selecting element, and has a transmissivity of 90% and a FWHM of 3 nm. The output mirror of the cavity has a transmissivity of 30% and is mounted to a piezo which controls the cavity length.

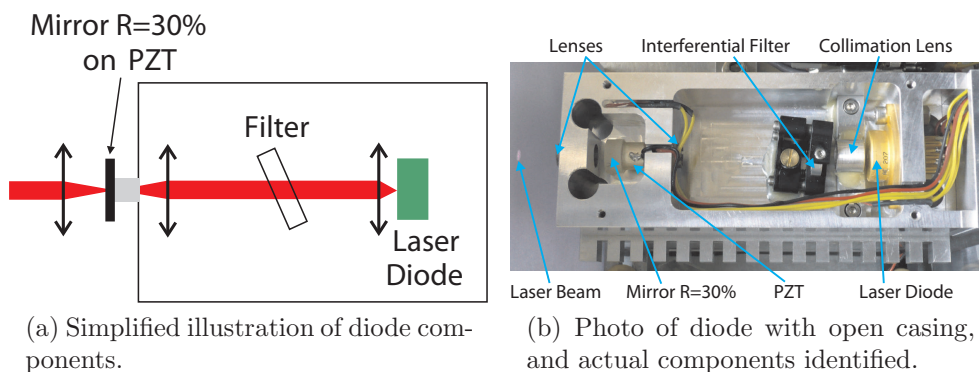


Figure 6.15: Laser diode constructed from models developed at the Paris Observatory.

This design offers several benefits in comparison to the Littrow design that we previously used for our other diodes [Ortalo, 2009]. First, the frequency selecting element and the cavity mirrors are decoupled, which grants us the possibility to tune the cavity frequency while independently optimizing it for stability. The usage of a linear cavity also allows us to change the wavelength by rotating the interferential filter, without changing the direction of the output beam. Finally, the output mirror is placed in a *cat's eye* configuration, in which the mirror is located in the focal plane of the focusing lens. This allows us to preserve the cavity stability by nullifying the effects of any changes in the cavity beam direction.

With each of these lasers, we manage to obtain roughly 40 mW of output power at 852 nm. Initially, the output beams have a highly elliptical shape, thus we use a set of

anamorphic prisms with a 3:1 ratio to render them Gaussian and usable for the rest of the experiment.

We use two of these diodes to trap the atoms in the MOT and repump them into the $F=4$ state. The diode “Shaddok” produces a beam which is tuned to the 3-4 transition, which pumps the atoms from $F=3$ to $F=4$. We send this beam into a fibered beam splitter, which provides us with two repump beams at its output near the MOT chamber. We then apply a circular polarization to these beams and attenuate their output so that they each have around 2 mW of power.

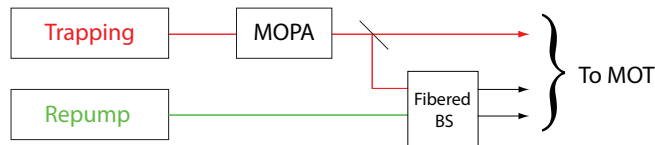


Figure 6.16: Trapping and repump beams mix in a fibered beamsplitter to provide 3 trapping beams, and 2 repump beams at the MOT.

Next, we use a diode called “Zeus” to create the trapping beams for the MOT which are tuned to the 4-5 transition and red-shifted by 10 MHz. We use three trapping beams that enter the MOT chamber from orthogonal directions, and recombine at its center. The beams then exit the chamber, where they reflect off of fixed mirrors and return along their original path, thus trapping the atoms from 6 directions. The beams have circular polarizations such that two of them are left circularly polarized, and the third is right circularly polarized. We require around 25 mW of power in each of these three beams. As our diode is only capable of producing a total output power of around 40 mW, we first pass the light through a MOPA which amplifies the power up to 600 mW. After alignment and coupling losses inside of the MOPA, we have about 300 mW at the MOPA output that is usable for the experiment. We then divide this beam into two segments, sending one segment directly to the MOT chamber, and sending the other through the second input port of our fibered beam splitter, as shown in Figure 6.16. This allows us to obtain a total of three trapping beams at the MOT chamber.

6.3.3.1 Locking

In order to lock each diode to its respective transition, we use the saturated absorption spectroscopy technique to measure the Doppler and transition peaks. We then use a lock-in detector to create the error signal which then passes through to an integrator circuit. The integrator applies the feedback control to the piezo mounted in each diode to lock the cavity. The diodes are also temperature controlled using a homemade controller which provides us with a temperature regulation having 10 mK stability. The frequencies of the diodes are fixed by locking them onto the crossover resonances which arise due to the closely-spaced excited states. We then pass each beam through an

RF-tuned AOM which allows us to precisely adjust its frequency. Table 6.1 identifies the crossovers and AOM frequencies that we use for each laser. This method allows us to easily adjust the beam around the transition frequency, as well as extinguish it with a digital command.

Laser	Transition	Lock Point	AOM
Repump	$F=3 \rightarrow F'=4$	3-4 Crossover	Order -1: 100 MHz
Trapping	$F=4 \rightarrow F'=5$ -10 MHz	4-5 Crossover	Order +1: 115 MHz

Table 6.1: Transitions and lock points for MOT lasers

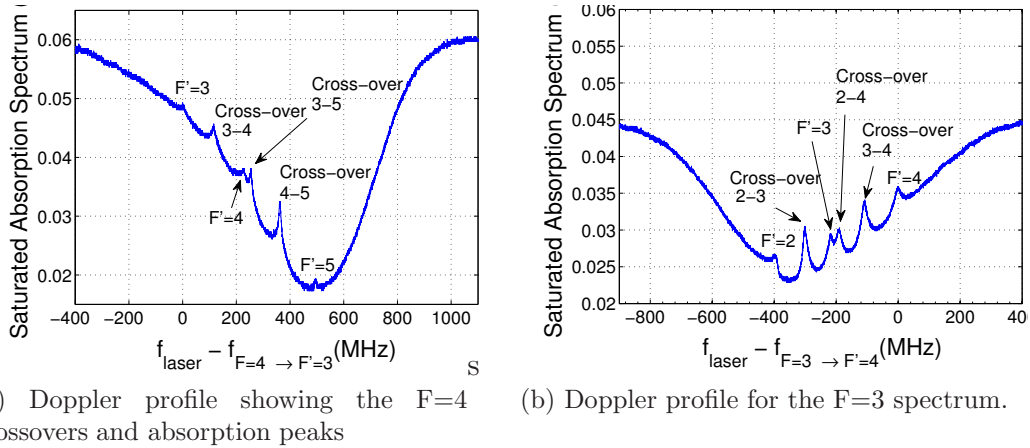


Figure 6.17: Saturated absorption Doppler measurements of the Cesium $F=3$ and $F=4$ lines.

6.3.4 Controlling the Magnetic Field

While it is necessary to use a magnetic field to create our atomic cloud, the presence of a field during the memory storage can introduce huge limitations to the memory performance. As the magnetic field in the chamber has an inhomogeneous distribution throughout the atomic cloud, the atoms in different regions of the cloud experience different degrees of Zeeman level splitting. This results in an inhomogeneous broadening and eventual dephasing of the atoms in different sections of the cloud as the system evolves, finishing with a loss of the collective coherence between the atoms in our ensemble. When magnetic fields are present, this process can take place within a few hundred nanoseconds [Felinto *et al.*, 2005]. Thus, the decoherence effect fixes an upper limit on the storage time that we can expect with our memory.

By cutting off the magnetic field, we can preserve the coherence between our atoms for a much longer time, and thus expect larger storage times. Once we begin to cut

the magnetic field, the atoms of our cloud immediately begin to disperse. Thus it is in our interest to cancel out the magnetic field as quickly as possible, so that we can nullify it while maintaining a high atomic density.

In order to control the magnetic field created by the coils, we use a current driver circuit based on a design published in [Garrido Alzar *et al.*, 2007]. This design allows us to control the amount of current flowing through the MOT coils by applying an analog voltage signal to a control box. A network of transistors in the circuit controls the current flowing through to the coils by acting as a sink, and allows us to create a magnetic field that is proportional to the applied analog voltage. This circuit is useful in that it not only allows us to use low control voltages of around 10V, which are easily producible, but we can also supply it with a relatively low current of 10 A, which is also easily produced using a commercial generator. A critical factor to take into consideration when selecting the circuit components is the choice of the transistor breakdown voltage. When we cut off the current flow by setting the control voltage to 0V, this can create a high voltage back-electromotive force (emf) which can potentially overload and destroy the transistors. As this emf is determined by the cutoff time, the current flow, and the coil inductances

$$Emf = -L \frac{dI_L}{dt}, \quad (6.9)$$

we have to take these properties into account during our transistor selection.

The details of the circuit construction and characteristics will be described in more detail in the future Ph.D thesis of Lambert Giner. Here, we focus on describing the optimization of the timing and control mechanism associated with this circuit.

6.3.4.1 Control Signal

Switching off the magnetic field induces eddy currents in nearby magnetic materials, which can create time and spatially varying magnetic fields around our atoms [Garrido Alzar *et al.*, 2007]. In order to minimize the effects of these currents, and reduce the magnetic field experienced by the atoms to zero as quickly as possible, it is useful to reverse the current direction before cutting it off completely. This allows us to cancel out these induced transient fields.

Usage of this technique introduces several technical consequences. First, any electronic system that we develop will have a unique response which depends on the coil construction, the nearby environmental fields, and the components in the electronic circuits. Thus we must try to experimentally observe when our field has been properly cut off. Furthermore, the time needed to cut the field to zero depends on the amount of current flowing through it at a given time. Thus when we reverse the current flow, we introduce time as a second factor as we must determine how long we need to apply the reversed current.

These factors mean that we must empirically determine how to optimize the current flow so that we can completely cancel out the field as quickly as possible. As we control the current with an analog voltage, this means that we have to carry out an optimization procedure on our voltage signal.

One option for optimizing the signal is to use an arbitrary waveform generator, and manually program it with our desired signals. While this works, it is a slow and expensive solution as programming in each waveform can be a time consuming process.

We thus decided to use a spare NI analog acquisition and generation card to generate our signals. By using a Labview based computer interface, we could change all of the necessary parameters for our signal within seconds, and find an optimal waveform within a day. This proved particularly useful when we had to rebuild the circuit several times, as each circuit required different signal parameters.

6.3.4.2 Labview Interface

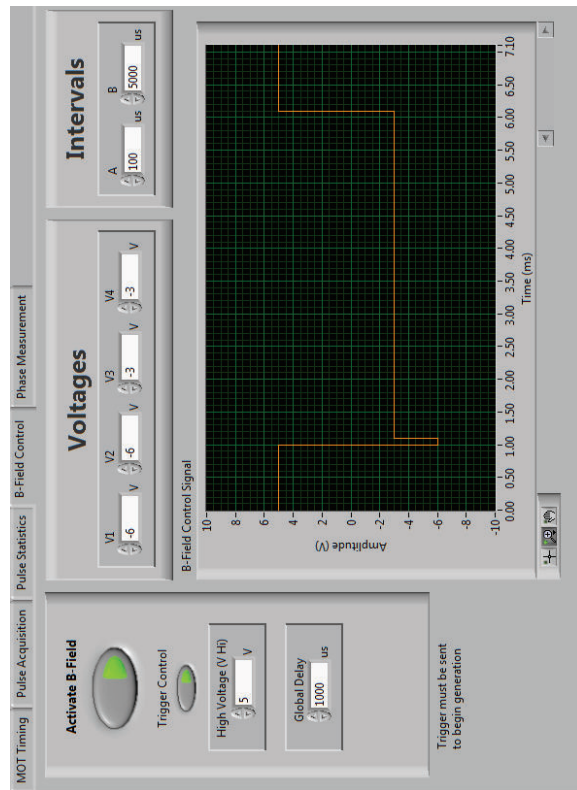
The interface for our program was that shown in Figure 6.18. We used it to specify the positive and negative voltages of our control signal, as well as the time for which we wanted to apply the reversed current (interval A), and the duration of time when wanted to keep it at zero (interval B). We used an FPGA generated TTL signal as an input trigger to launch the generation of this signal. Our hardware consisted of an National Instruments PCI-6733 high-speed analog output card connected to a BNC-2110 connector block. This BNC connector allowed us to send the analog output from the card directly to the voltage control input of the driver circuit.

6.3.4.3 Program Operation

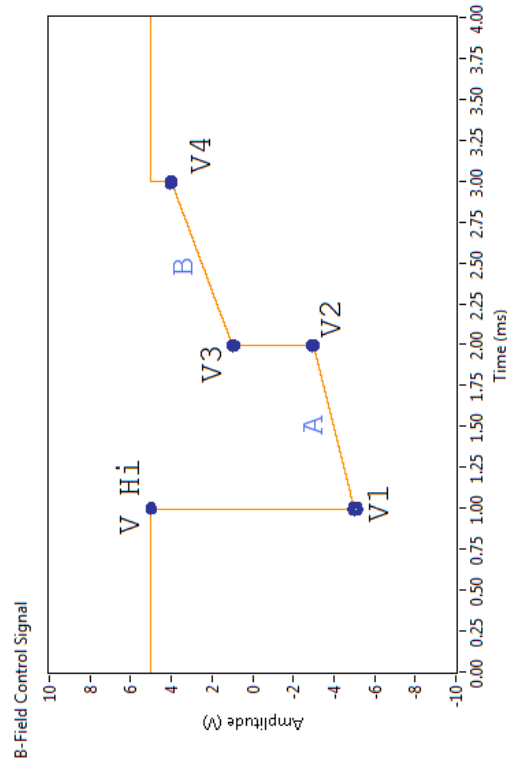
In order to understand the code that allowed us to carry out this generation, we must first understand the program's intent, which is to generate arbitrary analog voltages for a fixed time period after receiving a trigger.

We can begin by describing our analog signal as a function composed of two variable intervals A and B, and a fixed high voltage V_{HI} as shown in Figure 6.18b. The interval A varies between the voltages V_1 and V_2 , and B varies between voltages V_3 and V_4 . When the card receives a trigger signal, it outputs V_{HI} for a small amount of time, and then outputs the voltages specified for intervals A and B. When these intervals have passed, the voltage output level returns to V_{HI} until the next trigger is received.

Our card is capable of generating output at up to 1 MS/s, however in order to reduce the distortion of our signal, we limited our output generation rate to 250 kS/s. The generation process works by writing voltage levels to a large array buffer for every sample of our generation period, where each voltage is represented as a double precision float. Because we specify the type of signal we want to create and all of its properties are well-defined, we can prefill the entire array of voltages during the configuration of



(a) Labview control panel used to generator the analog signal.



(b) Illustration of user-configurable variables to optimize the signal.

Figure 6.18: Labview interface and analog signal generated by DAC used to optimize the time to cut the B-field.

our card, and write them to the card to be executed by the hardware when it receives our trigger.

The voltages that we output during the intervals A and B have the possibility of taking on increasing or decreasing values over time. Due to this, we can specify the voltage values to insert in our array for these intervals with the expression

$$V_{out} = V_i + i \frac{V_f - V_i}{t}, \quad (6.10)$$

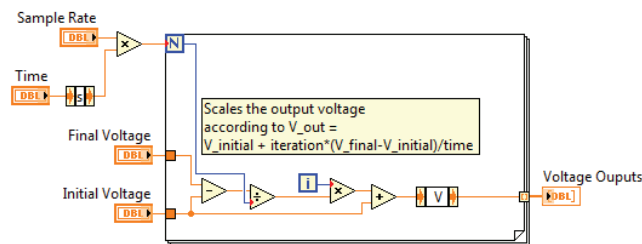


Figure 6.19: Code used to create the analog voltage values. This block takes two voltage ranges as inputs, and calculates and fills an array of voltage values for each time segment for the control signal.

where t represents the duration of each interval A and B, and i represents the index of their respective array buffers. The Labview implementation of Equation 6.10 is shown in Figure 6.19.

Once we have generated the array buffers for each segment of our signal, we simply concatenate these arrays together, and send the entire array to the card's hardware buffer, so that it will begin the generation of our signal on command. The Labview diagram for this program is shown in Figure 6.20.

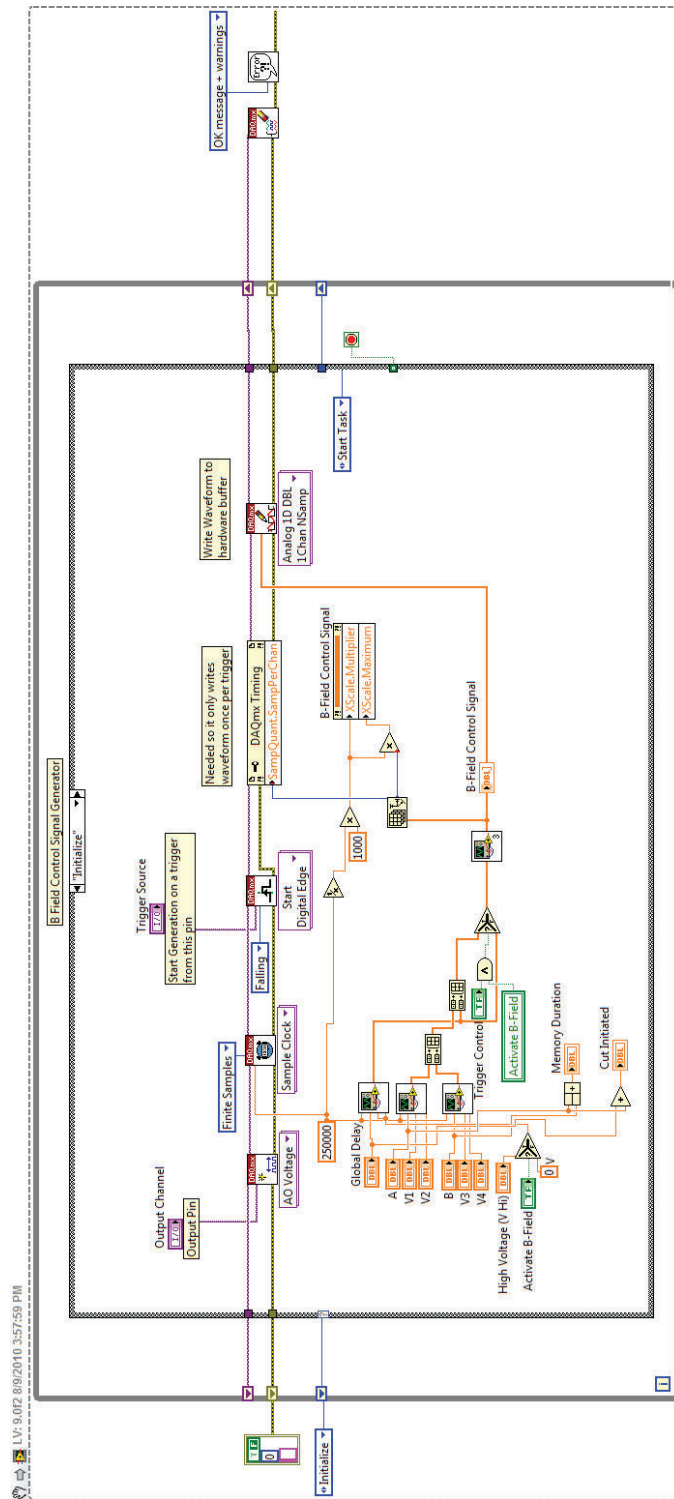


Figure 6.20: Block diagram for Labview interface to used to generate the control signal

6.3.4.4 Results

By using this current driver and control signal generator, we were able to cut the coil currents by at least 16 dB to 2% of its original value within $700 \mu\text{s}$ of sending our TTL trigger, which is a short enough time to allow us to carry out the storage before the atoms begin to dissipate, as the plots in Figure 6.21 show.

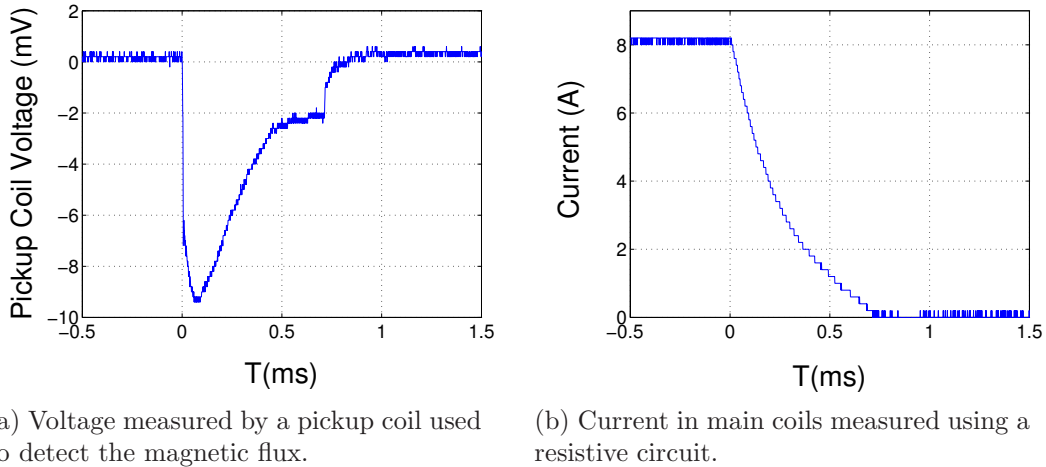


Figure 6.21: We can cut the magnetic field quickly by reducing the coil current by 16 dB within $700 \mu\text{s}$, using the optimized control signal.

6.3.5 Timing

Once we created the MOT, we needed to introduce a timing mechanism in order to allow us to send pulses of light into it while cutting off the magnetic field. The synchronization requirements oblige us to have a precise control over the lasers, the timing for the OPO pulse creation, as well as the circuitry to cut the magnetic-field for the MOT. In Chapter 7, we will discuss how we developed an FPGA program to implement this timing control.

In order to extract reliable statistics regarding the operation of our memory, we need to carry out multiple storage and retrieval runs of a large number of optical pulses. For each run, we prepare the MOT by creating a dense atomic cloud and pumping the atoms to the $F=4$ state for about 18 ms. After the atoms have been sufficiently pumped, we then cut the magnetic field. While the field strength decreases, we leave the trapping beams activated for about 1 ms to preserve the optical molasses, along with the repumping beam who will continue to repump any depumped atoms. Shortly after the field reaches zero, we then cut the trapping beams and the repump beams. Figure 6.22 outlines the timing relationship between the magnetic field and the beams

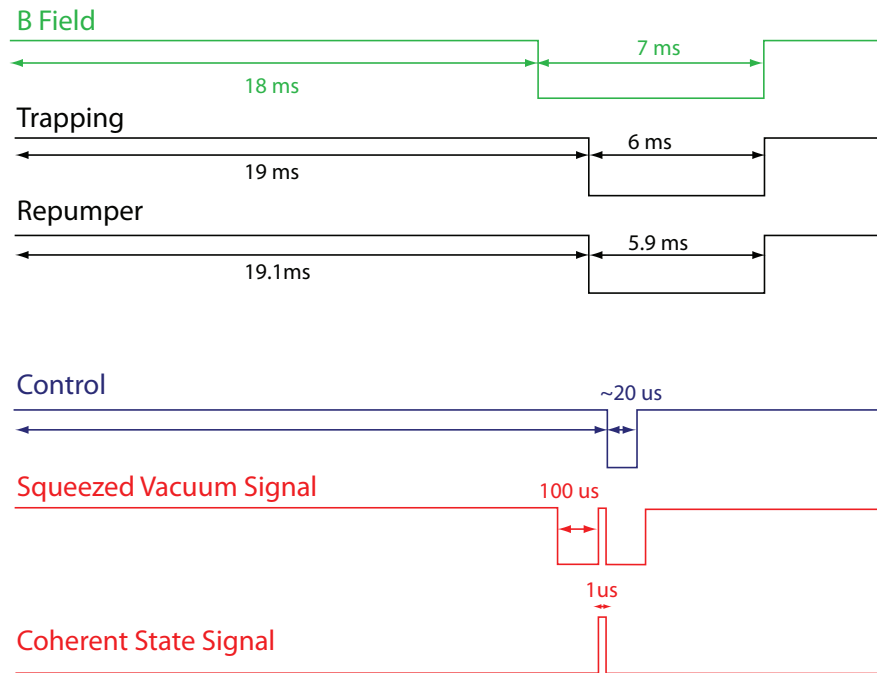


Figure 6.22: Timing diagram for the quantum memory. We trap the atoms for 18 ms to obtain a high density, and after cutting the magnetic field, cut the trapping and repump beams 1 ms later. The signal beam stays active when using a squeezed vacuum, as it allows us to track the quadrature phase evolution. It is mostly inactive when using a coherent state.

used for the experiment. We define the *memory sequence* as the time period from when we send the trigger to switch off the magnetic field, up until it is reactivated. We allocate about 18 ms for the preparation phase of each run, and about 7 ms for the memory sequence where we store the pulse. Thus the storage should occur every 25 ms, allowing us a 40 Hz repetition rate for the experiment.

The control and signal beams are active throughout the entire experiment except for certain periods during the memory sequence. Once we cut the trapping and repumping beams, we cut the wait for a few hundred μ s and then cut signal beam. We then send a small pulse of the signal beam, and once the pulse is inside of the atoms, we cut the control beam to close the transparency window and store the pulse. After a short time, we reactivate the control beam to release the pulse, and then reactivate other beams along with the magnetic field, which begins the process again for the next run.

6.4 Optical Layout

Now that we have discussed the system used to generate the EIT control beam, the MOT and B-field driver, we can begin to examine the optical elements needed in order to carry out storage of our state. Firstly, we require a system that allows us to measure the optical density of the atomic ensemble in order to ensure that our light has the highest interaction efficiency. Next, as we will use EIT for storage, we need to send in our control beam to open the transparency window, as well as pulses of our signal beam that we wish to store. Before attempting to store squeezed states in the memory, we will first attempt the storage of coherent states in order to optimize the system. Therefore, we also need a system which allows us to create pulses of coherent light to use as the signal to be stored. Also, as we want to store entanglement in two atomic ensembles, we will need a system to allow us to create the two atomic ensembles within the MOT. Finally, we will need to carry out the detection of the squeezed states and monitor the control and signal beams to calibrate our quantum memory. Figure 6.24 shows the optical layout that we have built around the MOT in order to satisfy these requirements.

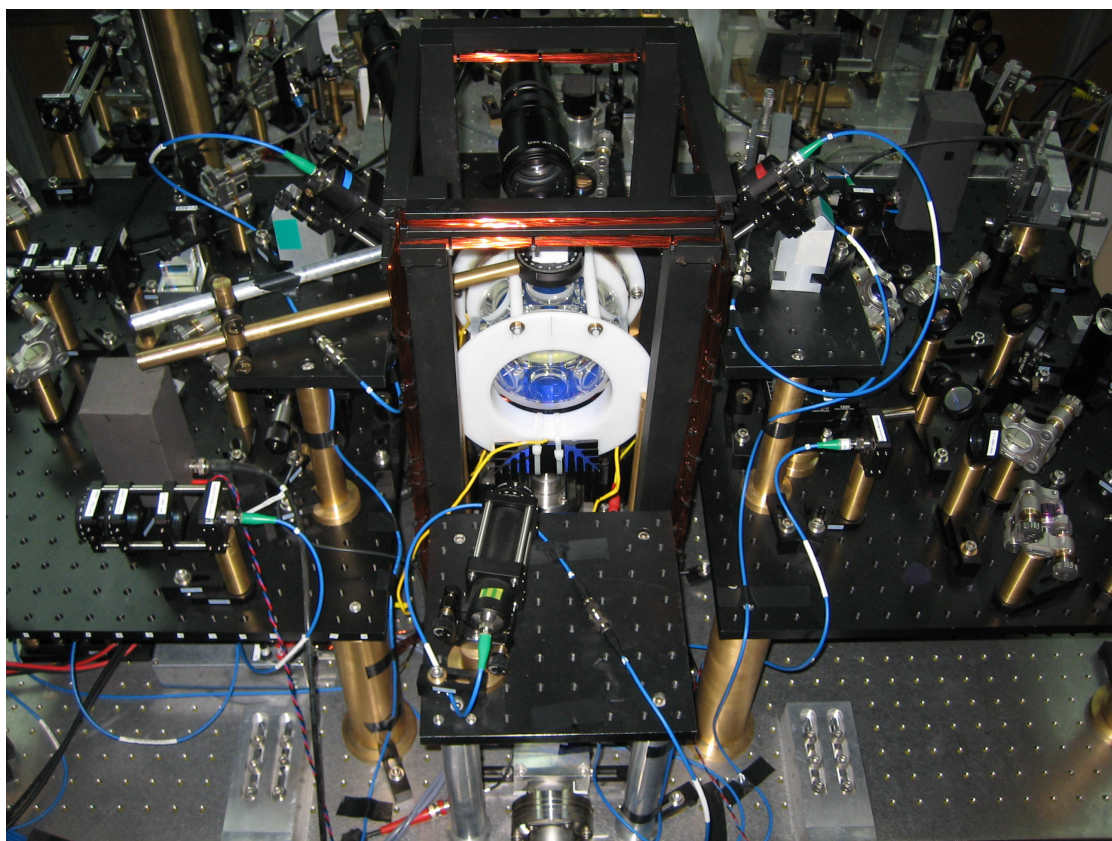


Figure 6.23: Photo of optical setup around the MOT used to implement the quantum memory.

6.4.1 Beam Displacers

As we wish to store entanglement in two atomic ensembles, we use a set of beam displacers to create two memory ensembles within the MOT [Choi *et al.*, 2008]. This gives us the versatility to send the light into separate regions of the atomic cloud, and effectively create two MOTs. Once the beam displacers are installed, we can either send in a squeezed vacuum state which can be separated into two entangled beams, or we can send in EPR entangled beams generated directly from a Type II OPO [Laurat, 2004] and use the beam displacers to send a different polarization into each ensemble.

The beam displacers are a set of calcite crystals ordered from the Karl Lambrecht Corporation, having a 10 mm x 20 mm aperture and cut to a customized thickness. If we adjust the half-wave plates placed along the path of the signal and control beams, we can rotate their polarizations to 45° and the beam displacers separate them into their horizontally and vertically polarized components. By placing a beam displacer before and after the MOT, we can recombine the separated beams after they interact with the atoms. The beam displacers were cut to provide us with a $750 \mu\text{m}$ separation distance between the two beams, as depicted in Figure 6.25. In order to avoid optical losses which would destroy the quantum properties, we requested a transmission of at least 98%, which corresponds to our measured values.

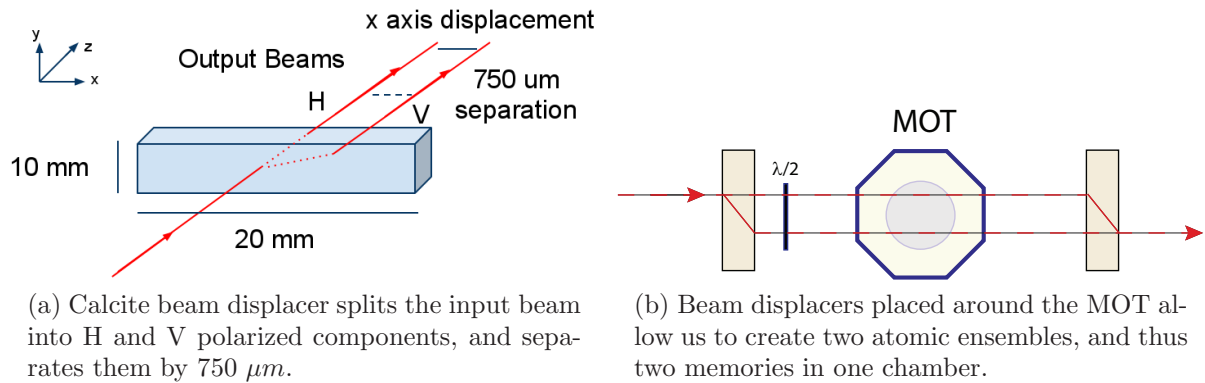


Figure 6.25: Beam displacers used to create two memories.

While a low transmissivity acts as a source of optical losses, we can also experience losses when using the second beam displacer to recombine the two beams after the MOT. Thus, it is critical that we obtain a high recombination visibility. Therefore we requested that each beam displacer be cut from the same crystal in order to maximize their optical compatibility, and we mounted each one on an 1800 3-axis prism mount from Melles Griot, and replaced the angular adjustment screw of one mount with a PE4 piezo actuator from Thorlabs. This allows us to adjust the relative angle between

the beam displacers with micrometric precision, and optimize the recombination visibility. By modulating the piezo with a triangular waveform, we can sweep the relative phases between the two recombining beams, and thus recreate visibility fringes for easier optimization.

6.4.2 Signal Beam

We begin by locking the Matisse laser onto the 4-4 transition, and sending a portion of it to the main table via a fiber optic. It then either passes through the OPO to create our squeezed vacuum state, or arrives at the MOT directly in the form of a coherent state. We will use the coherent signal for optimizing the memory before replacing it with the squeezed vacuum. As we want to store pulses of light, we create these pulses by first passing the continuous beam through to a separate breadboard which transmits the light through two AOMs arranged in a serial +1/-1 order configuration. This allows us to deviate the optical path of the beam without changing its frequency when we drive the two AOM's at the same frequency. These AOMs are controlled by a TTL pulse from the FPGA, and we have the possibility of shifting the output signal frequency if desired by driving each AOM with a different RF signal. These coherent pulses then enter into another fiber, and re-exit at the MOT where their optical path recombines with the mode-matched path of the squeezed vacuum from the OPO.

As the coherent and squeezed vacuum beams have the same matching, we can easily optimize the storage with the coherent pulses and then use the same timing parameters to store the squeezed pulses. The signal beam is focused onto a $50\ \mu\text{m}$ waist size at the center of the MOT chamber. Once the signal leaves the MOT, it passes by a flip-flop mirror which allows us to send it to a fiber optic coupler. As a first step in determining our memory efficiency, we will connect the output of this fiber coupler to an avalanche photodiode detector (APD) which will allow us to measure the memory efficiency in the pulse counting regime. After achieving the desired efficiency, we can then remove the flip-flop mirror allowing the signal to propagate on to the homodyne detector, where we can carry out the quantum tomography.

6.4.3 Local Oscillator

A local oscillator from the Matisse arrives on the table via fiber optic, where it is mode-matched and recombined with the signal beam as it leaves the MOT, and then proceeds on towards the homodyne detector.

6.4.4 Control Beam

The control beam that we use to open and close the EIT transparency window in the atoms comes from a separate diode laser that is phase locked to the Matisse at a 9.2

GHz frequency offset. This light arrives from the diode via a fiber optic, and is focused onto the atoms with a $200 \mu m$ waist. The control beam and signal beam combine at the atoms with a 1° angle between them. We chose a small angle so that we would avoid diminishing the memory storage time [Zhao *et al.*, 2008]. Once the control beam leaves the MOT, its path continues on to another fiber optic coupler which allows us to send it to a remote photodetector for observation.

6.4.5 Auxiliary Beam

We also provide an auxiliary beam at the red-shifted 4-5 transition which allows us to measure the optical density. This beam is brought directly from the MOPA output via a fiber optic. When measuring the optical density, we hook the beam's fiber up to the coherent signal path in order to measure the density as it will be seen by our signal pulse.

6.5 Optical Density Measurements

As stated earlier, an important property that determines the efficiency of our storage is the optical density of the atomic ensemble as seen by our signal pulse, which tells us the fraction of light absorbed by the atomic ensemble with respect to the total amount of light incident on it. As the density of the atoms increases, more of our signal is absorbed and stored in the atomic cloud, and the overall efficiency of storage increases.

We measure the optical density by sending a weak probe beam into the atoms on the 4-5 transition detuned by $\delta = 10$ MHz, and measuring the amount of absorption experienced by the beam compared to when the atoms are not present. When we pass our probe beam through the atoms, the atomic linewidth will undergo a spectral enlargement given by

$$\Gamma' = \Gamma \sqrt{1 + \frac{I}{I_{sat}}}, \quad (6.11)$$

where $I = \frac{P}{4\pi\omega^2}$, $I_{sat} = 2.7 mW/cm^2$, $\Gamma = 5.2$ MHz, and P is the beam power. We can define the attenuation f of the pulse by

$$f = \frac{V_{sig}}{V_{ref}}, \quad (6.12)$$

where V_{sig} is the photodetector voltage measured from the attenuated beam, and V_{ref} that for the referenced beam. Once we have measured this attenuation factor, we can then determine the optical density using the expression

$$OD = -\frac{\delta^2 + \Gamma'^2/4}{\Gamma'^2/4} \ln(f), \quad (6.13)$$

where δ is our 10 MHz detuning from resonance. With this technique, we can measure the optical density at several time points after extinguishing the magnetic field to observe how the density of the atomic cloud evolves in time before dispersing.

6.5.1 Implementation

To carry out these measurements, we need to measure the absorption of the light when atoms are present, and compare this to the amount of light detected when the MOT is empty. We could simply place a photodiode at the MOT exit, take a reference measurement, empty the MOT, and take a second measurement, however the fluctuations of laser intensity over the course of many measurements could give us a false measure when we average the data. Therefore to avoid this possibility, we set up photodiodes before and after the MOT and divided the probe beam so that it simultaneously illuminated both detectors, as shown in Figure 6.26. This allowed us to simultaneously measure the amplitude of both the reference and signal beams, and obtain a more stable measurement by avoiding any effects from intensity fluctuations in our laser.

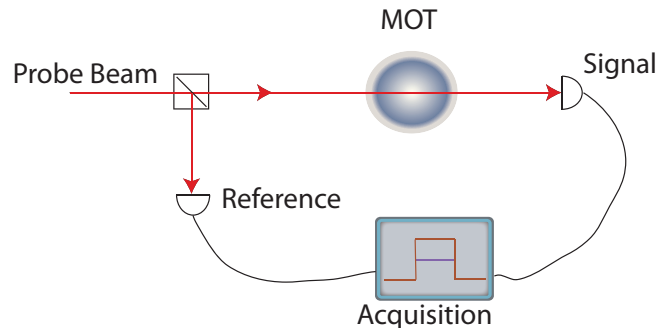


Figure 6.26: Schematic of the layout for the optical density measurement. A signal and reference photodiode are digitally calibrated in Labview, and provide the optical density and eliminate laser intensity fluctuations.

We sent $400 \mu W$ of light from the probe laser along the optical path of the signal for a pulse duration of $10 \mu s$ for the density measurement. We needed to adjust the photodetectors to have a high gain and high bandwidth in order for them to detect a clear square signal, as the pulses had a low power, and only lasted for such a short time. Once we were able to detect clean square pulses, we sent the reference and signal photodiode outputs to an NI PCI-MIO-16E-4 acquisition card, where we were able to numerically adjust the offsets, and gains of the acquired trace. This allowed us to

calibrate the light passing through the empty MOT to the light detected directly with the reference photodiode. Attempts to simply take the maximum and minimum points of our acquisition trace resulted in too noisy data, thus we numerically set thresholds at 120% of the minimum, and 95% of the maximum, and averaged all of the points beyond those thresholds in order to more cleanly determine the absorption. This process was done for each pulse, and 40 pulses were averaged together in order to give a running average for the optical density. Figure 6.28 shows that Labview interface that we used to control this measurement.

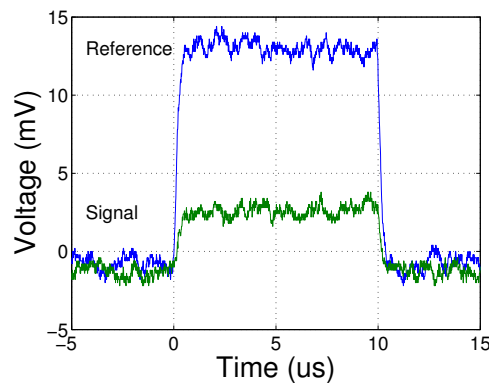


Figure 6.27: 10 μs pulses used to measure optical density show an attenuation by 2/3 corresponding to an optical density of 20. Single pulse acquisition shown.

With this setup, we managed to observe a maximum optical density of 20 with magnetic field active, as plotted in Figure 6.27. This level of optical density should allow us to achieve a memory storage efficiency of 10-20% [Gorshkov *et al.*, 2007].

6.6 Raman Scheme for the Compensation of the Magnetic Field

Although we can measure the current flowing through the MOT coils to try to evaluate if the B field near the atoms is zero, we are still subject to stray fields that come from the environment that can have strengths of up to several hundred milligauss. In order to completely remove the effects of these parasitic fields, we installed a set of compensation coils around the MOT which allow us to correct for these environmental fields. These coils allow us to apply a magnetic field in 3 dimensions independently, with strengths of up to 1 G. To use these compensation coils, we must be able to determine how exactly we need to apply the field to correct for the magnetic parasites. Using the atoms themselves as indicators turns out to be the best means of accomplishing this.

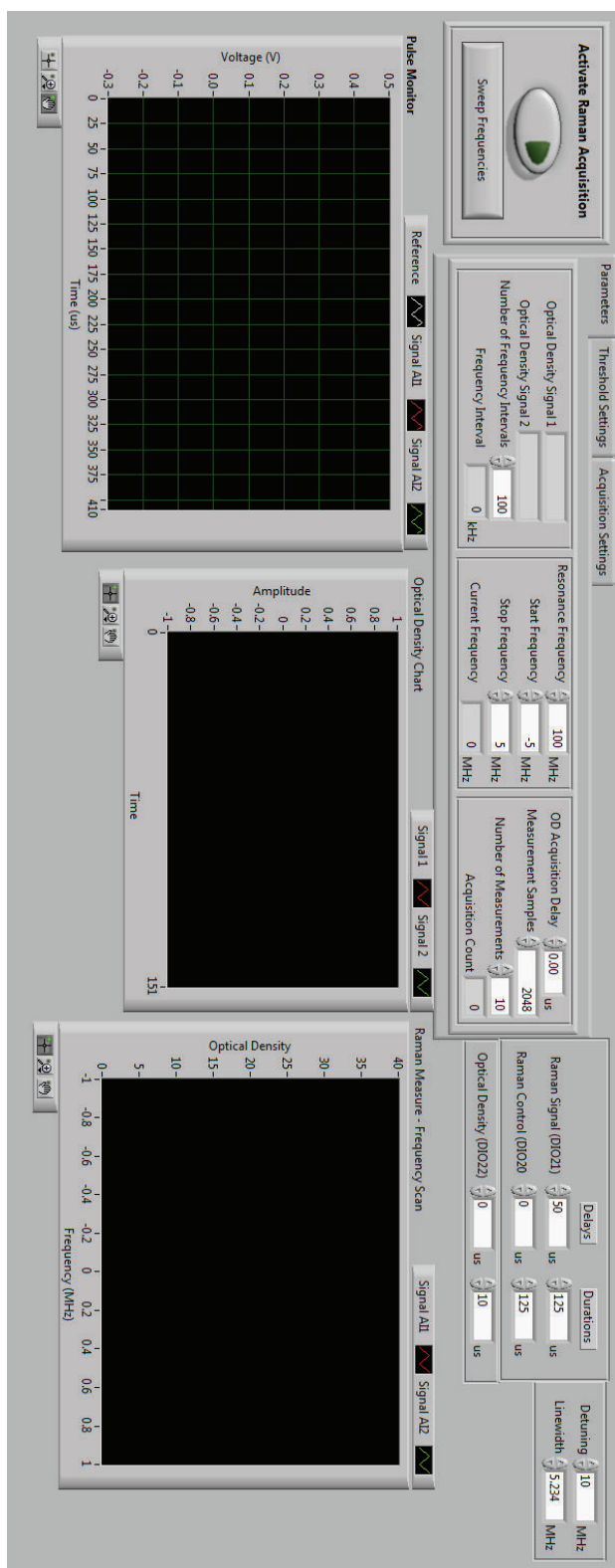


Figure 6.28: Labview interface used to program the optical density and raman spectroscopy pulses.

6.6.1 Raman Spectroscopy

In order to determine if a magnetic field is present near the atoms, we will use the technique of Raman Spectroscopy which is insensitive to Doppler broadening, but very sensitive to broadening caused by magnetic fields [Ringot *et al.*, 2001]. This technique connects the hyperfine ground states $F=3$ and $F=4$ by means of a virtual excited level. This transition is far detuned from the $F=4$ level so that we can prevent any resonant transitions to and from the excited $F=4$ level. Figure 6.29a depicts this transition diagram. We can also define the Raman detuning as

$$\delta_R = \omega_1 - \omega_2 - \omega_{HF}, \quad (6.14)$$

where ω_{HF} is the frequency of the hyperfine transition, 9.2 GHz, and ω_1 and ω_2 are our laser frequencies. Depending on the Raman detuning, we can drive atoms from the state $F=3$ into $F=4$ via stimulated emission at frequency ω_1 . When magnetic fields are present, the Zeeman levels are split, and atoms are transferred for several different values of the detuning δ_R . In the absence of magnetic fields, this transfer only occurs at resonance $\delta_R = 0$.

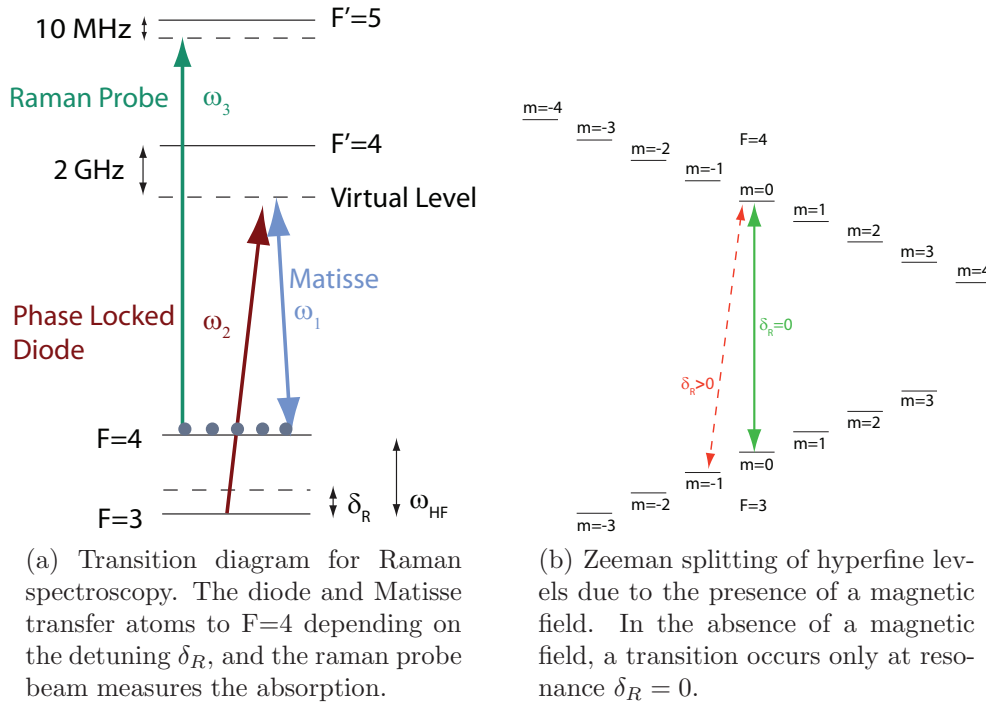


Figure 6.29

By sending a probe beam detuned by 10 MHz from the $F=4 \rightarrow F'=5$ transition into the atoms, we can measure the absorption of our probe for different detuning values.

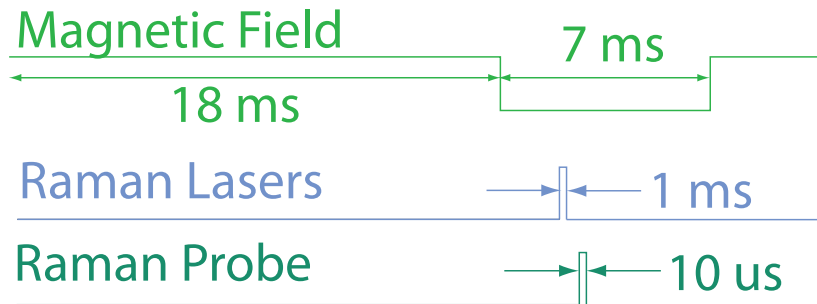


Figure 6.30: Timing diagram for Raman pulses and probe beams. The pulses first transfer the atoms after canceling the B-field,, and the probe measures the absorption.

The number of resonances that show absorption and the frequency spacing between them tells us the strength of the magnetic fields present [Felinto *et al.*, 2005]. When we succeed in completely canceling out the magnetic field, we only observe one absorption peak at resonance. Figure 6.30 depicts the timing diagram for this measurement.

6.6.2 Labview Interface

As we require a phase coherence between our two Raman beams, we use the phase-locked diode and the Matisse laser to probe for the Raman transitions. Scanning the laser frequency requires repeated measurements in order to extract the signal from the noisy data, thus we developed a Labview program to control the scanning rate of our laser and average the results. It changes the Raman detuning by digitally changing the reference frequency for our OPLL. The interface for this program is the same as that used for the optical density measurements, as shown in Figure 6.28.

Figure 6.31 shows a portion of the block diagram that we use to scan the Raman laser. This code is implemented using a Labview instrument driver, which is a downloadable preprogrammed interface to our E4420b signal generator. We enter into the front panel the frequency range we would like to scan for the Raman detuning, and the number of increments we desire. The program creates an array for each frequency increment, and it iterates through the array sending the desired frequency to the Configure Frequency instrument driver at each point. The driver then communicates with the signal generator via a GPIB cable, who then changes the OPLL reference frequency to the desired point. Once we have scanned the entire frequency range, the program resets the reference frequency to its original position.

While scanning the frequency, we measure the attenuation of the Raman pulses using the same reference and signal photodiodes as used for the optical density measurements. This allows us to determine if a certain frequency setting leads to a stimulated Raman emission. The program acquires the density settings using an acquisition card, and plots the density as a function of frequency at the end of the scan.

6.7 Conclusion

The development of this experiment is currently underway, however in this section, we have shown the major advances made in order to carry out the storage and retrieval of squeezed states in cold Cesium atoms. Now that the major components have been developed, there remains the process of optimizing the MOT, before proceeding to test the memory in the classical domain.

In the next chapter, we will discuss the details of the timing system developed to synchronize and trigger the different aspects of this experiment.

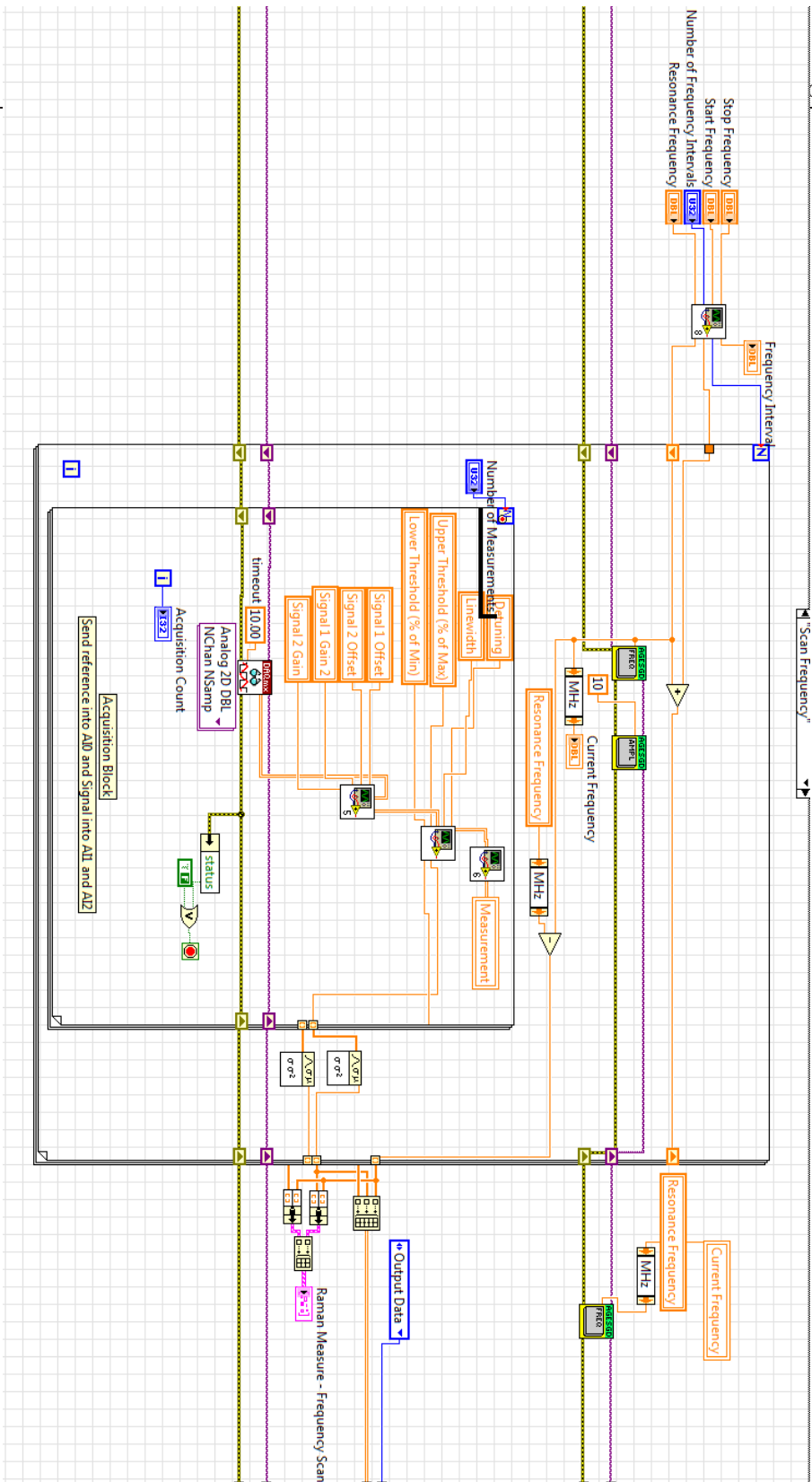


Figure 6.31: Block diagram for program to scan the phase lock frequency and adjust the detuning δR

Usage of an FPGA for Timing Applications

Contents

7.1	Digital Timekeeping	134
7.1.1	Software Based Clocks	135
7.1.2	Hardware Based Clocks	136
7.1.3	Digitizing the Oscillator	137
7.2	FPGA Digital Circuits	138
7.2.1	Programming an FPGA	139
7.2.2	The Labview FPGA Programming Model	142
7.3	Basics Concepts in Digital Logic	145
7.3.1	Data Representation	145
7.3.2	Digital Input and Output (DIO)	145
7.3.3	Integers	146
7.3.4	Floating Point Numbers	146
7.4	Basic Building Blocks for Timing Applications	147
7.4.1	Describing a Pulse	147
7.4.2	Labview Timer Implementation	148
7.4.3	Labview Implementation	151
7.4.4	Implementing the Pulse generator	151
7.4.5	Putting the Blocks Together	153
7.5	Experimental Application	153
7.5.1	Laser Timing via Pulse Delay Generation	155

7.5.2 Chopper Period Measurement	156
7.6 Where to find Source Code	157

Timing precision is an important requirement in many aspects of atom optics experiments. Due to the fact that we work with processes that occur at microsecond timescales or below, we need a way to precisely determine when to launch the preparation of our quantum states, as well as the procedures to appropriately measure them. In this chapter, we will discuss the solution we implemented to control the memory experiment using a National Instruments PXI-753R FPGA along with the Labview FPGA development environment. We will first begin with an overview of the necessary digital concepts, and then discuss the experimental applications of these concepts in the specific cases of our experiment.

7.1 Digital Timekeeping

Although we perceive the passage of time in a continuous manner, we are limited to measuring it discretely using tiny intervals. This fact makes it easy however, to use digital techniques for keeping track of time.

We can describe a time span digitally as the sum of a number of fixed-sized intervals. The size of the interval relative to the time span fixes our precision in measuring the span, thus the smallest size of our interval gives us a more precise measurement.

$$T = \int dt \rightarrow \sum_{\delta t \rightarrow 0} \delta t \quad (7.1)$$

With this way of describing the flow of time, we can now conceive the idea of a digital clock, as a device which marks a starting point in time t_0 , and keeps a running count of the number of ticks δt which have occurred since this starting point. Using this definition, we can easily develop an algorithm such as that in Listing 7.1 which describes the operation of a digital clock.

```

1  clock_counter = 0
2  clock_running = true
3  while(clock_running)
4    clock_counter = clock_counter + 1
5    print clock_counter time has passed
6    do_something_else
7  end

```

Listing 7.1: Digital Clock Algorithm

Here, we execute the algorithm instructions in a sequential manner. First we create a *clock_counter* variable which stores the number of time intervals that have passed, and initialize it to 0 before measuring our time span, effectively marking our t_0 . We then start our clock with the while loop in line 3, and lines 4-6 are executed once for every loop iteration, where the loop repeats for as long as our *clock_running* variable holds true. For each loop iteration, we increment our counter in line 4, thus adding δt to our running sum, display the currently measured time span in line 5, and carry out an arbitrary action based on the current time in line 6.

We will see in a later section how this overly simple description can translate directly into a useful programmatic implementation. The generality of this description allows us to implement it using software, or hardware-based techniques. Our choice of implementation however, has critical consequences on the precision and reliability of our time measurement.

7.1.1 Software Based Clocks

If we take our algorithm and write it in a standard imperative language such as C, we can compile it and run it on a computer running an operating system such as Windows, Linux, or Mac. Once we ran the program, it would increment our clock counter, and display our time as we expect, and thus appear to function as expected.

A crucial problem however, is that the passage on time experienced by the computer program, what we call *CPU time*, is not the same as the passage of time in the real world, or *wall time*. When computer program runs, it sequentially executes the instructions of our algorithm as fast as possible. We must keep in mind however, that the processor is not only executing the instructions listed in our timekeeping algorithm, but also instructions from other programs that are needed to display information on the screen, read and write to files, and other operations necessary to run the operating system itself. Thus in writing and executing our program, we simply propose a set of instructions to the processor to execute. Our processor will execute those instructions however, at a time when it determines is the most convenient. It is often the case that our instructions will be preempted by other instructions which the processor has placed at a higher priority than those in our program.

As a result, the intervals at which the code executes in our algorithm are not fixed, and do not always correspond to real wall time intervals. This can result in the computer program thinking that 25 ms have passed, when in reality 1 second has passed.

Another limitation to using a software based clock is that all of the instructions executed on an operating system take a finite amount of time. At any instant, a processor can have millions of instructions scheduled for execution which are unrelated to our algorithm. Thus while our software-based clock runs, millions of instructions can be carried out between 2 iterations of our main timing loop. If we consider that we

run our program on a 2 GHz processor which can execute 10^9 instructions per second, if we have 10^6 instructions to execute between our loop iterations, that means that our software clock's loop can run no faster than once every millisecond. Therefore, our software-based approach gives us no ability to measure timescales smaller than this. Thus, we have two major obstacles in using software-based clock implementations. The overhead of running an operating system imposes a non-trivial time interval in between each iteration of our loop, and the execution priority of our instructions prevents us from being able to make any real correspondence between CPU measured time, and events taking place in real time. The usage of a *real-time* operating system could potentially address these issues, but using a hardware based timing system is a more commonly used alternative. We have considered here the special case of using a software-based clock on a computer with a standard operating system. We could also conceivably program our algorithm directly into a microcontroller using the C language, and bypassing any operating system overhead. Although this would improve the performance allowing us to measure smaller time intervals, the fundamental problem concerning the uncertainty of our instruction execution remains.

7.1.2 Hardware Based Clocks

While software-based clocks depend on properly-timed code execution to measure a time interval, hardware based clocks can provide a much more stable and reliable method of timekeeping as they are limited only by their physical properties and the environment. The hardware-based clock uses as its fundamental element an *oscillator*, which outputs a fixed-frequency voltage waveform. We can construct an oscillator using several different techniques, such as those seen in the following sections.

7.1.2.1 RC Oscillators

RC Oscillators can be made with a network of resistors and capacitors that use the phase shift of a signal propagating through the circuit, combined with a voltage amplification and feedback mechanism to output an oscillating DC waveform. If we consider that the circuit has a characteristic resistance R and capacitance C , the frequency of our output waveform will be given by the expression

$$F = \frac{1}{2\pi RC} \quad (7.2)$$

RC oscillators are often simple to create, and can create output voltages with frequencies up to the MHz range. The drawback of using an RC oscillator is that the output frequency depends on the values of the circuit components, which drift over time. These drifts often arise due to the component's sensitivities to moisture and

temperature changes in its surrounding environment. Thus, RC oscillators do not possess a long-term stability.

7.1.2.2 Crystal Oscillators

A more stable type of oscillator can be made using crystals such as quartz, which possesses piezoelectric qualities. If we cut the quartz into small wafers and apply a voltage to it, it begins to vibrate at a resonance frequency that is determined by the thickness of the crystal. The vibrating crystal functions electrically in the same manner as an RLC circuit, and creates an oscillating DC voltage at the crystal's resonance frequency. Because the crystal's oscillation frequency is determined by its thickness, it is much less sensitive to environmental fluctuations. Crystal oscillators can be made to function at frequencies up to several 100 MHz.

7.1.3 Digitizing the Oscillator

The oscillators described in the previous section serve the purpose of establishing a fixed frequency reference which is represented as an analog and continuously changing DC voltage waveform. Thus in order to use this waveform for digital timekeeping, we must digitize it. We can accomplish this by simply sending our waveform through an analog comparator combined with a stable DC reference voltage, as represented in Figure 7.1. If for example, our DC waveform oscillates between 0-5V at frequency f , we can send it to the comparator along with a 2.5V reference voltage. The comparator will output 5V when our signal has a higher voltage than the 2.5V reference, and output 0V when it has a lower voltage. We thus manage to create a stable digital oscillator from our analog reference oscillator.

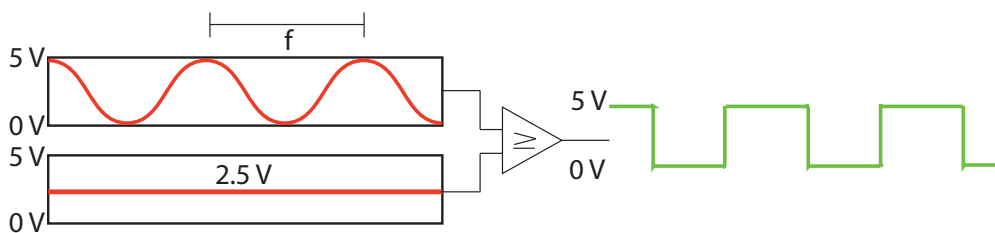


Figure 7.1: We can use a comparator to transform a continuous valued analog signal into a two state signal.

Once we have a digitized oscillator, we can interface it with digital logic circuitry to act as timebase, which represents the flow of time. This is necessary because digital circuits can only represent data as binary values, which we typically interpret as values of True or False. Thus when a circuit detects our digitized oscillator, it can read the

5V values as True, and read the 0V values as False. Each time a True value is read by the circuit, this can signify the passage of one time interval.

7.2 FPGA Digital Circuits



(a) Example Xilinx FPGA before mounting onto a circuit.

(b) FPGA mounted on National Instruments PXI-7853R card with 96 digital input/output ports, and 8 analog inputs and outputs.

Figure 7.2: Pictures of FPGA chips.

The type of digital circuit that we use for our timekeeping applications is a Field Programmable Gate Array (FPGA). An FPGA is a chip composed of millions of transistors arranged into blocks, and tiny interconnects which we can use to route signals. We can combine the transistors to create simple logic gates, and then use the interconnects to create more complex logic circuits. Due to the small size of an FPGA, the propagation of a signal through the interconnects can terminate within nanoseconds. Thus the FPGA can perform functions equivalent to many analog electronic circuits used with traditional components. Unlike analog circuits, logic circuits of an FPGA can be repeatedly reprogrammed onto the chip by the circuit designer. Thus we can configure a chip to function as an integrator circuit one minute, and later reprogram it to function as a filter, PID controller, or data acquisition system. The ability to reprogram our electric circuit on demand gives FPGAs a versatility that is unparalleled by analog circuits. This allows us to develop a logic circuit once, and once we have verified its operation, we can reuse it indefinitely. As FPGAs have tight operating parameters, we can be reasonably certain that once we create a working circuit on one chip, we can easily duplicate it on another chip and expect the exact same functionality. These

characteristics add extraordinary value in a lab environment where change occurs frequently, and it is usually difficult to produce two analog circuits with an exact duplicate functionality. Furthermore, once a digital circuit has been conceptualized, it can be easily shared with other users. This thus accelerates the overall pace of development for an experiment.

7.2.1 Programming an FPGA

In order to create a digital logic circuit in an FPGA, we need to program it using a Hardware Description Language (HDL) such as VHDL or Verilog. Unlike iterative programming languages such as C, an HDL describes the logical functioning of the circuit as a black box. We then specify the inputs, outputs and a combinatorial logical function which maps the inputs to the outputs.

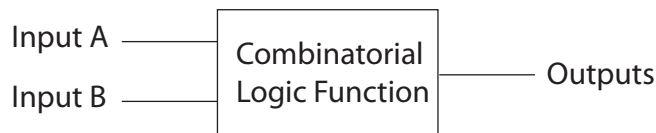


Figure 7.3: We can represent our HDL modules as black boxes with specified inputs, outputs, and combinatorial logic functions.

In Figure 7.4, we show an example logic diagram which describes a half-adder circuit, and the same circuit expressed in Verilog HDL in Listing 7.2. This circuit adds two bits together from the A and B inputs, and outputs the sum and carry values from this addition. The internal logic function uses XOR and AND logic gates.

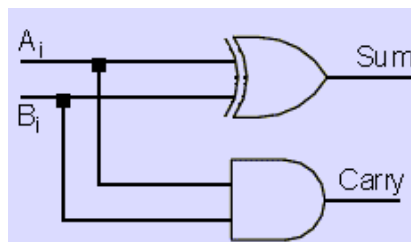


Figure 7.4: Logic Diagram for a 1-bit half adder circuit. It takes two Boolean values as input and outputs their sum and carry values.

7.2.1.1 Higher Level Programming

Although an HDL provides a means to directly describe how our circuit should function, programming a complex algorithm using an HDL can quickly become a difficult exercise. Successful usage of an HDL requires a foundation of digital logic design

```
module half_add(output reg sum,  
               output reg carry, input a, b);  
always @(a or b)  
begin  
    sum    = a ^ b;    //XOR  
    carry = a & b;    //AND  
end  
endmodule
```

Listing 7.2: Verilog program for a one bit half-adder

experience. As FPGAs do not execute code sequentially, as computers do with imperative languages such as C, developing an algorithm using an HDL requires a completely different programming methodology. Due to these difficulties, it is simpler to program an FPGA using a higher-level programming language that provides simpler conceptual constructs, and is capable of generating HDL code itself. This greatly simplifies the development process, and allows us to benefit from the power and flexibility of using FPGA without having mastered a particular HDL or digital logic design.

7.2.1.2 NI Labview and Labview FPGA

For our applications, we use the Labview programming language with its FPGA module as our higher-level interface. Labview provides a visual programming environment, where graphical symbols represent simple logic gates, and we can connect the gates using simulated wires. There are numerous benefits as well as drawbacks to selecting Labview FPGA as a development platform.

Benefits

Simplicity

The graphical aspect of Labview makes programming the FPGA much simpler, as we no longer need to learn a complex HDL syntax. Furthermore, once we construct a logic diagram for our circuit, we can create a working representation of it almost directly in Labview. This allows us to use conditional logic to easily create complex programs, which would become much more challenging if we were using traditional components. Figure 7.5 shows the half-adder circuit implemented in Labview FPGA. We can see that it matches that logic diagram shown in Figure 7.4 directly.

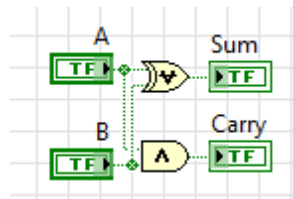


Figure 7.5: Half adder implemented in Labview. Created directly from logic diagram using logic gates, and Boolean controls (A,B) and indicators (Sum, Carry).

Cost

Another interesting benefit is that we can greatly reduce the cost of our device compared with fixed-purpose devices. As we wanted to create an application for timing control, we evaluated several models of digital pulse delay generators for comparison. Their prices averaged at around 600 Euros per digital output, thus allowing us to control eight devices for around 5000 Euros. By creating a pulse generator on an FPGA, we can use its 96 digital outputs to lower this price to 30 Euros per output, or even further depending on the FPGA model. Thus we can use it to control more devices in our experiment for a lower cost, and repurpose it on demand if needed.

Rapidity

Using Labview FPGA can greatly accelerate the development time for certain electronics tasks. We can develop simple applications in minutes, and complex applications in days that would normally weeks or months using standard analog electronics. Furthermore, our applications can handle much more complex cases, allowing us to attempt tasks which would otherwise be impossible.

Drawbacks

While using Labview FPGA presents enormous benefits, there are serious drawbacks that must be considered when deciding whether to use this system.

Proprietary Platform

Labview is a proprietary platform developed by the company National Instruments. This means that the software is closed to public analysis of its source code, and as a result, NI is the only entity capable of fixing platform bugs, of which there are many. Updates to the platform are costly and are only released twice a year. NI has been known to remove previously supported features from future versions of their software, making them available only at extra cost. Additionally, the HDL code generated by

Labview FPGA is encrypted and not available to the end user. Thus it is impossible to take the code, and run it on any hardware that is not sold by NI. This means that anyone who wants to use the Labview platform must purchase the core software, the FPGA module, and the FPGA hardware from NI.

Costs relative to other systems

As NI requires this purchase of specific hardware and platform licenses, this makes the initial investment of the material much more expensive than purchasing the equivalent FPGA components, and programming them directly in an HDL. However creating a system for FPGA programming from the basic components requires expertise in digital electronics, circuit layout and design, digital logic programming, and C programming. Thus the decision of whether to invest in the Labview platform or develop a system from the basic components requires a cost/benefit analysis on a case by case basis. Individual who have the necessary expertise may choose to develop their own systems, while groups who must transfer the knowledge from person to person might prefer the long term benefits of a simpler Labview platform.

7.2.2 The Labview FPGA Programming Model

In this section, we will illustrate the general structure of how the Labview platform allows us to easily develop FPGA programs. When running a program on the FPGA, it runs independently from the computer which we use to control the system, however we can benefit from using a computer interface to interact with it.

The development of every FPGA application is centered around a “Labview Project”, which links all of the files, dependencies and configuration resources needed to compile and run a program. In the Project Explorer window show in Figure 7.6, see the expanded project resources which list our host computer, and the FPGA target device that we wish to program. Beneath the FPGA device are additional resources configured for the FPGA such as analog and digital input and output ports, a 40 MHz clock which we can use as a timebase, and the FPGA.vi code which contains our program.

When running a Labview FPGA program, the FPGA can only run one source code file at a time. Thus, if multiple projects need to be run simultaneously, then the code for each project needs to be merged into one file. We thus place the code to be run on the FPGA under FPGA tree, and name it “FPGA.vi”. Although the program executes independently from the computer when it runs, Labview allows us to use the simple FPGA.vi front panel as a simple interface to control and monitor the program state. Not every function can be carried out on the FPGA however, and thus if we wish to have a more complicated interface, we are required to create a separate program on our host computer. Figure 7.6 shows this as the “Host.vi” file under the My Computer tree.

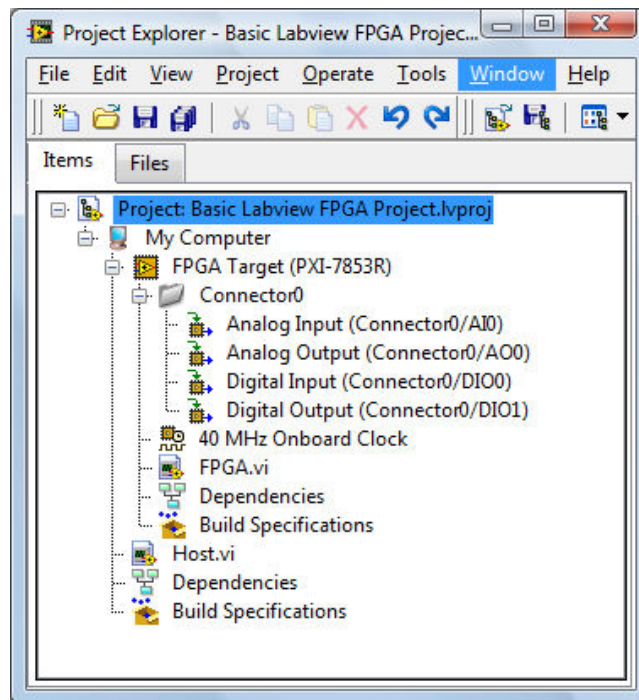
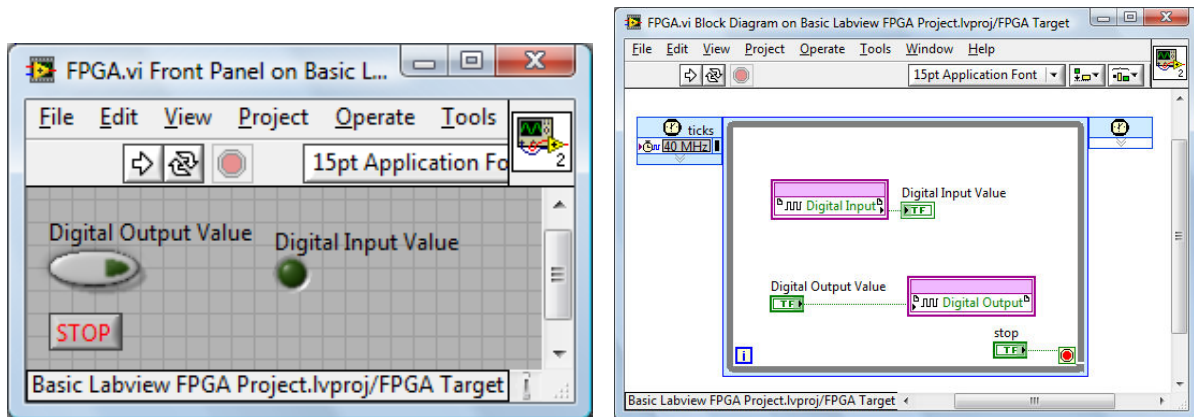


Figure 7.6: Labview project explorer lets us see all of the resources and dependencies needed for an FPGA project.

A simple example application is one which lets us monitor and change a digital voltage level on digital input/output ports. Once we have created our Labview FPGA project, we can then develop a program such as that shown in Figure 7.7 which runs on the FPGA. We see the actual code for the FPGA.vi file in the FPGA.vi block diagram shown in Figure 7.7b. This code continuously reads the values of the “Digital Input” port, sending them to the “Digital Input Value” indicator, and takes values from the “Digital Output Value” control and sends them to the “Digital Output” port. We can use the front panel shown in Figure 7.7a as a simple interface to interact with the program.

While the FPGA vi shown in Figure 7.7 suffices for a simple application, we would be obliged to create a host vi to interact with our program if we require more advanced functionality. We can create this host vi by programming the Host.vi file such as is shown in Figure 7.8. The block diagram shown in Figure 7.8b illustrates the operation. The host begins by connecting to the FPGA program, and then continuously sends the data to the FPGA that we enter on the front panel. When we hit the stop button and exit the program, the host vi closes the connection to the FPGA vi.

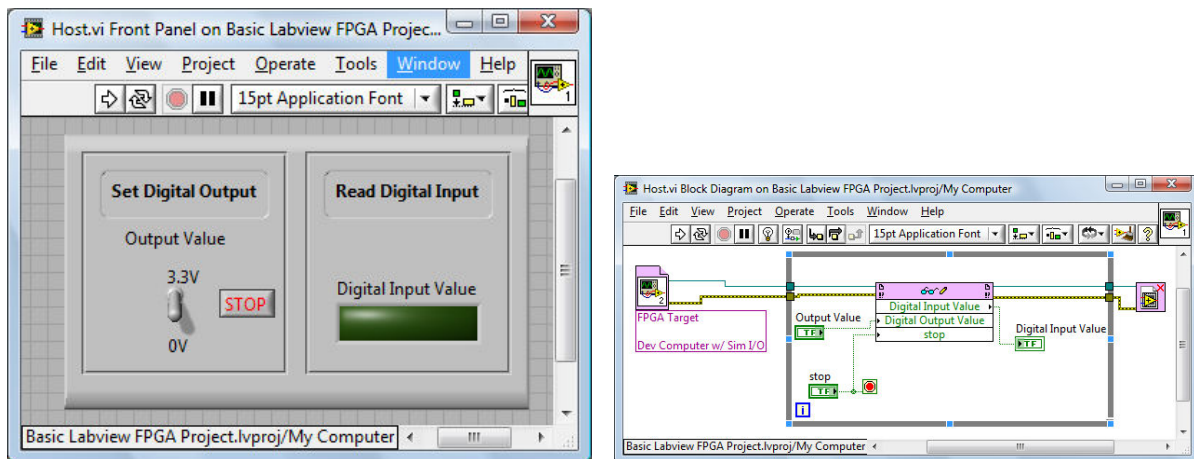
By using the host vi, we can monitor at behavior of our program executing on the FPGA. Figure 7.9 shows the result of us running this program. When we set the output



(a) FPGA based front panel interface allows simple interactions with FPGA program.

(b) FPGA based code which reads and writes data to and from digital input and output ports.

Figure 7.7: FPGA vi that we can use to generate and detect TTL level voltages.



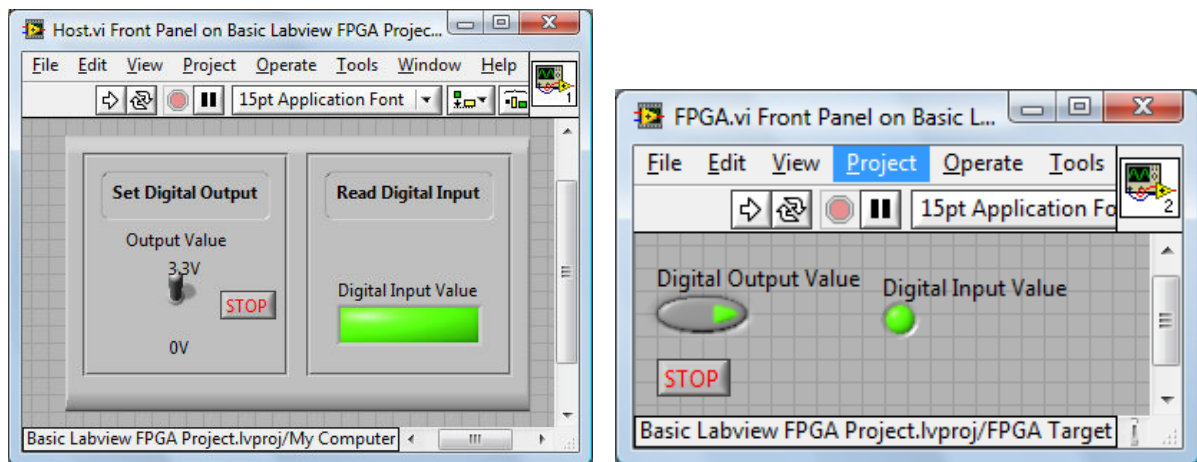
(a) Host.vi front panel interface run from the computer.

(b) Host.vi back panel code communicates with the program in the FPGA.vi

Figure 7.8: We can use a host vi to communicate with the FPGA vi when we need more advanced logging and monitoring functionality.

value to 3.3V in Figure 7.9a, we see in Figure 7.9b that the program mirrors the same behavior.

This simple example gives an overview of the process used to create a Labview FPGA program. We can use the same process to develop programs that provide more complex functionality, as we will see in the next sections.



(a) Host vi front panel while the program runs.

(b) The FPGA vi mirrors the input and output shown on the host vi.

Figure 7.9: Program running on the FPGA while interfaced with a computer-based host.

7.3 Basics Concepts in Digital Logic

Before diving into the implementation of our FPGA timing system, we will first overview a few necessary concepts of digital programming.

7.3.1 Data Representation

Any data that can be represented in a digital logic device, such as a computer or microcontroller, is composed of a series of bits, where each bit takes a value of 1 or 0, with 1 representing True and 0 representing False. Thus when we try to measure continuous data, we must first discretize it and form a digital representation composed of strings of 1's and 0's.

7.3.2 Digital Input and Output (DIO)

In order to interface a digital device with the analog world, we send data through pins connected to the device in the form of voltage levels. Although voltage is naturally continuous, we can use standardized voltage level definitions to represent a continuous voltage signal as a 1 or 0.

The voltage levels that we use for the FPGA are defined by Transistor-Transistor Logic (TTL). This logic interprets incoming voltages between 0-0.8 V as a low signal, or False, and it interprets voltages sent to the device from 2.0-5.0 V as a high signal, or True. Thus by encoding information into the voltage levels, we can recreate this information in the form of bit strings on the digital device.

In a similar way, we can send information from the device to the real world. If we instruct the device to set the value of a pin to True, or 1, the pin outputs a voltage of 5V (or 3.3V for Low-Voltage TTL). Similarly, by setting the value of the pin to False, the voltage on the pin goes to 0V. Thus by using TTL voltages, we can fully communicate digital information to and from our circuit.

7.3.3 Integers

We stated earlier that data is represented inside of a digital device by strings of 1's and 0's. A basic datatype that we can represent using these binary strings is an integer. The numeric value of a binary string is determined by the string length, and the numeric type. Integers typically use binary string lengths of 8, 16, 32, or 64 bits. The integers can also either have signed, or unsigned representations, where signed numbers can take on negative values.

There are consequences to using binary integer representations that must be considered. As there are only a finite number of permutations for a binary sequence of a given length, that means that our integer type can only represent a finite range of numbers. If we try to surpass this range, the number can *overflow* or *underflow*, and can take on unexpected values. Table 7.1 shows the ranges for the most common integer types.

Size	Name	Signed Range	Unsigned Range
8 bits	Byte	-128 to +127	0 to 255
16 bits	Word	-32,768 to +32,767	0 to 65,535
32 bits	Double Word	-2,147,483,648 to +2,147,483,647	0 to 4,294,967,295
64 bits	Long	-9e18 to +9e18	0 to 18e18

Table 7.1: Ranges for signed and unsigned integers

7.3.4 Floating Point Numbers

Floating point numbers add another level of complexity to our numerical types, and they can typically take on single or double precision representations. Usage of double precision floats usually offers more numerical stability in complex calculations. One limitation however, is that we can not represent every possible number using a double precision float. Therefore, calculations involving floating point numbers are often sensitive to rounding errors.

Although integers and floats are represented by binary strings, the FPGA can not natively interpret floating point numbers without additional software routines. Thus when implementing algorithms for the FPGA that require numerical operations, we must either use integers or fixed-point numbers.

7.4 Basic Building Blocks for Timing Applications

Now that we have described the fundamental concepts needed to work with digital logic, we will discuss simple logic applications that we can use on the FPGA in order to construct a larger timing application. The goal of our development was to use the FPGA to replicate a digital delay generator. This device allows us to regulate the timing of experiments by specifying precise trigger times, with high timing resolution and low jitter. It accomplishes this by producing TTL pulses at a set of digital outputs, which we can configure to have a desired time and width.

7.4.1 Describing a Pulse

The delay generator application we have developed for our experiment is a system to create TTL pulses with the ability to control their delays and durations with 25 ns precision. We can quickly analyze the creation of a TTL pulse to understand the method used.

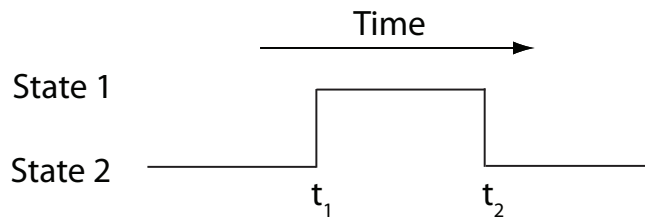


Figure 7.10: Representation of a pulse as change between two different states at two distinct time points t_1 and t_2 .

We can abstractly and succinctly define a square pulse as a binary state change at two points in time, as illustrated in Figure 7.10. We thus consider two dimensions in describing a pulse: the state dimension, and the time dimension. We can examine the time dimension by using the concept of a timebase, as shown in Figure 7.11. A timebase serves both as a reference for the flow of time, and a measuring system. We can represent this timebase as an infinite train of ticks, or events, where each tick represents the passage of a time interval. Once we have established our timebase, we can then pick an arbitrary point as a trigger, or initial time t_0 . By using the ticks in the timebase as a measuring system, we can specify two points after t_0 , t_{delay} and $t_{duration}$ in terms of the number of ticks after t_0 , which specify the start time and width of our pulse.

After determining the relevant time points for our pulse, we can now consider the second aspect - the state change. Since we are only considering binary state changes, we can use True and False values to identify the states. This allows us to define a positive

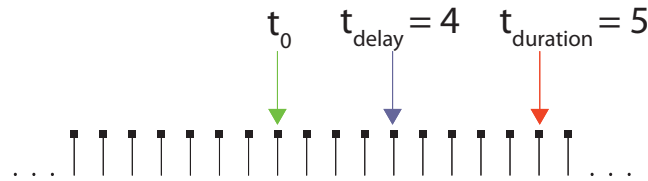


Figure 7.11: Infinite timebase with reference point t_0 chosen. We can express time intervals by counting the number of timebase ticks.

pulse as a sequence of False-True-False states, and a negative pulse as a sequence of True-False-True states.

7.4.2 Labview Timer Implementation

Now that we have developed the basic concepts, we can examine how to implement a timer using Labview FPGA. We first begin by creating our timebase. Labview FPGA provides a Single-Cycle Timed Loop (SCTL) which allows us to do this. The SCTL is a Labview construct which allows us to execute code in a loop that has a deterministic processing time - specifically, the code is executed within 1 clock cycle of the FPGA. For our timer, we configure the FPGA to use a 40 MHz oscillator as a clock source, and thus any code executed in a SCTL is guaranteed to repeat every 25 ns. We can visualize this using Figure 7.12, where we have a series of events executed at each timebase tick.

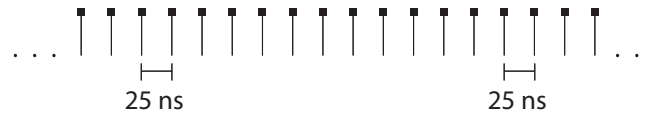
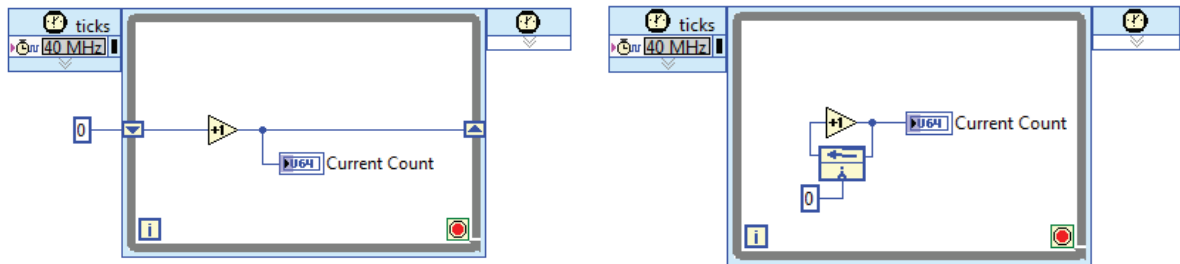


Figure 7.12: Example of a timebase represented by ticks.

Now that the timebase is established, we can create a clock to set an initial reference time, and track the number of ticks as time passes. In order to track this time, we can simply use a counter which is incremented by 1 with each passing tick.

Labview does not natively use the concept of a variable to store state such as we understand from C, due to that fact that it is based on a dataflow programming paradigm. Thus we can keep track of our counter in Labview by using a shift register or a feedback node. A shift register is a construct which passes the value of data present in a current loop's iteration, as input to the next loop iteration. Whenever we want to pass data between loop iterations, we must use one of these constructs. With this in mind, we can represent a counter using the layout in Figure 7.13a.

We initialize the counter to 0 before entering the loop, as mentioned in our algorithm. We must also take care to pick a numerical datatype large enough to avoid any



(a) Counter implemented with a Shift Register

(b) Counter with a Feedback Node. Provides the same behavior as the shift register implementation, but the compacted form allows us to enclose it in a SubVi.

Figure 7.13: Two options for implementing a counter using Labview.

unintentional overflows as we increment our counter. Considering that we will have 4×10^7 ticks per second at 40 MHz, if we select our counter to use a datatype of U64, our clock will be capable of running for over 14,000 years before overflowing.

By using a feedback node instead of a shift register, we can encapsulate this behavior in a subprogram, or subVi, and place the entire subVi in a SCTL as shown in Figure 7.13b, and thus create our FPGA based clock.

For our applications, we have developed over time a slightly more complex timer based on this method, shown in Figure 7.14, which provides expanded functionality.

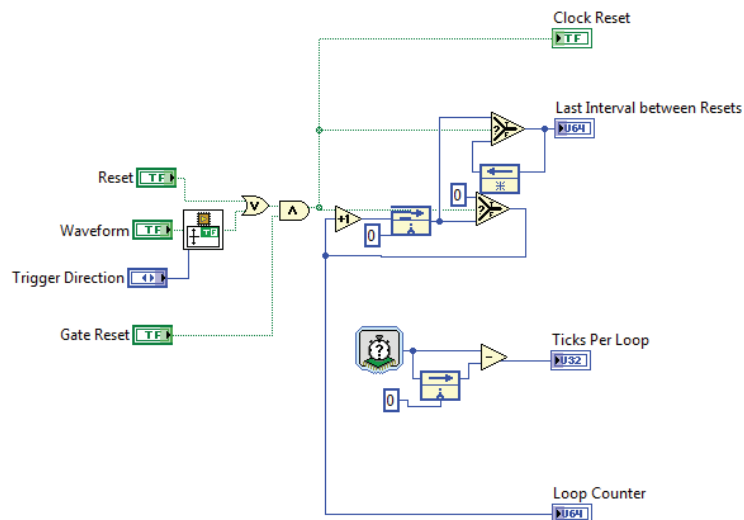


Figure 7.14: Full clock timer used for our FPGA programs. Timer is resettable by a Boolean signal or square waveform, and tracks the elapsed time as well as loop execution time.

This timer has the feedback loop counter embedded within it, but also gives us the ability to reset the counter on demand. We can reset it by either sending a True value on the Reset input, or by sending in a square waveform on the Waveform input. We can decide if we want to reset the counter on the waveform's rising edge, falling edge, or both.

This expanded timer outputs a True signal on the Clock Reset output indicator every time it is reset to 0, which allows us to monitor the timer progression and control other program logic. It also uses a second feedback register to track the number of times the loop is executed before each clock reset using the Last Interval Between Resets output. If we choose to use this timer in a normal while loop as opposed to a SCTL, the Ticks Per Loop output tells us the number of ticks needed for each loop to execute once, which allows us to measure the duration of our loop logic.

7.4.2.1 Digital Input and Output

The next aspect of creating a pulse is generating our state change event. Using a binary state allows us to use a Boolean value to represent our pulse outputs. When combined with LVTTTL logic, we can create voltage outputs from these Boolean values.

With Labview FPGA, we can accomplish this by using DIO ports as depicted in Figure 7.15. Our model of FPGA has 96 DIO ports available, each of which can be configured as a digital input, or a digital output. In order to use a pin as a digital output, we simply wire a Boolean control to a DIO port in Labview. If we set the control value to True, the FPGA outputs a 3.3V level, and if we set it to False, it outputs 0V.



Figure 7.15: Creating TTL voltage output using Labview FPGA. Writing a True value to a digital output produces 3.3V on the pin. Writing a False value produces 0V.

Using a similar method, we can detect voltage state changes as Boolean state changes. Thus if we wire a Boolean indicator to a DIO port in Labview and send 5V to its pin, the indicator will show a True value. Once its voltage falls below 0.8V, the indicator value will become False. Figure 7.16 shows an implementation in Labview.



Figure 7.16: Creating TTL voltage input using Labview FPGA. A 5V voltage on the pin of a digital input is read as a True value. A 0V signal is read as False.

7.4.2.2 Detecting Edge Transitions

We can use this method of digital input to detect TTL edge transitions and thus create triggers. If we send a square wave into a pin configured as a digital input, and read the DIO port over time, we will read out alternating True and False values where each value is read in 1 clock tick.

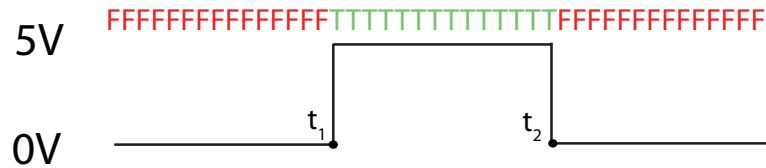


Figure 7.17: True-False representation of digital input. Input state changes between True and False at two distinct time points.

As an edge transition involves a state change, we can detect edge transitions by simply detecting when a state changes from False to True, or True to False, where $F \rightarrow T$ represents a rising edge, and $T \rightarrow F$ represents a falling edge, as we can see in Figure 7.17.

7.4.3 Labview Implementation

We can implement this edge detection logic in Labview using an SCTL and a feedback node as shown in Figure 7.18. Here we simply compare the current value of our DIO input to the value from the previous loop iteration. If the values are different, then an edge transition has taken place. We can more specifically determine which type of transition has occurred by using the inequality symbols. If the current value is less than the previous value, then we have a falling edge, and if the current value is greater than the previous value, then we have a rising edge.

7.4.4 Implementing the Pulse generator

With our clock implementation and our knowledge of how to create digital output, we can implement a full FPGA digital pulse generator. As stated before, we can define our pulse using a delay time, t_{delay} with respect to a certain start time t_0 and a duration $t_{duration}$. We can also define it as two times t_{start} and t_{stop} with respect to our reference time, where t_{start} and t_{stop} represent the state change events. It is this second definition that we use for our implementation. The block diagram in Figure 7.19 shows us the core component of our pulse generator.

We send the Loop Counter output from our timer to the Clock input of the pulse generator, where the clock uses 0 as the start time. We also send in the two values

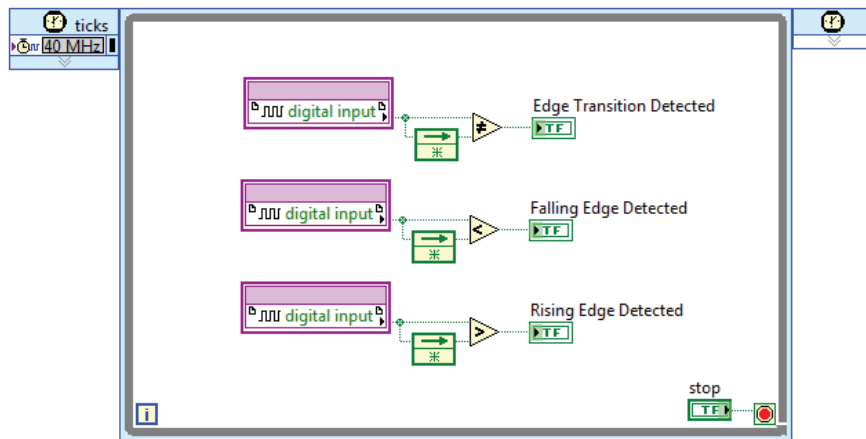


Figure 7.18: Methods of detecting edge transitions in Labview FPGA. The top example detects a rising or falling edge, the middle example detects falling edges, and the bottom example detects rising edges.

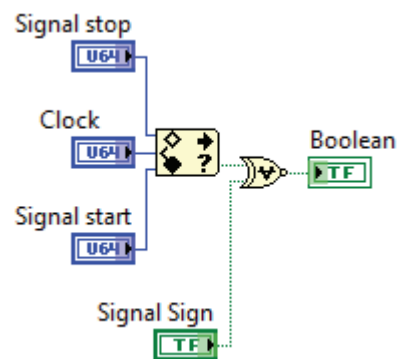


Figure 7.19: Pulse generation combinatorial logic function. Signal Stop and Signal Start specify the two time points for our pulse state change, and the clock input provides the current tick count. The Boolean valued state is output on the Boolean wire.

Signal Start and Signal Stop which specify the tick numbers at which we carry out the state changes. Finally, we use a Labview “In Range and Coerce” component which takes in three numbers - an upper limit, a lower limit, and a value, and outputs True if the value is between the limits and False otherwise. This behavior is the exact behavior that we use to describe our pulse. By connecting the output from this component to an XOR gate along with a “Signal Sign” Boolean control, we can easily change the output between positive and negative pulses. For a final step, we wire the output from our XOR gate to a DIO output terminal, and when we run the program, we produce voltage pulses with our desired timing characteristics on our output pin.

7.4.5 Putting the Blocks Together

Now that we have seen all of the necessary steps to create a digital delay generator, we can observe how to combine them to form a simple, but complete FPGA pulse generator with a computer based interface.

We can begin by creating a Labview project for the generator, such as shown in Figure 7.20. This project contains our PXI-7853R FPGA as a resource, which is configured with digital output ports named *trigger* and *laser control*. It also has a 40 MHz clock configured, along with an FPGA.vi program, and the subvis needed to run it. Additionally we have provided a Host.vi host interface program, along with its necessary subvis.

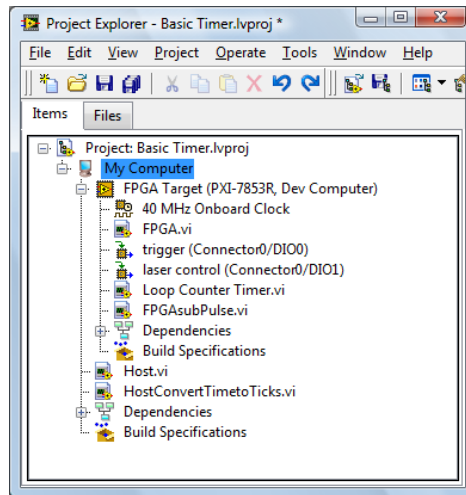
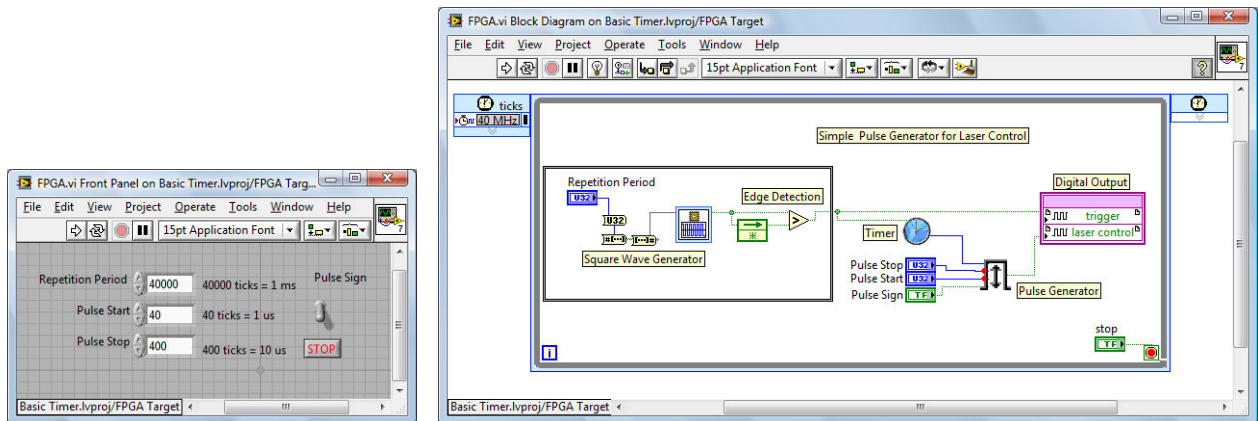


Figure 7.20: Project explorer showing the resources used to implement a digital delay generator. This includes clocks, digital outputs, subvis and other dependencies.

7.5 Experimental Application

We can now look at the FPGA.vi which contains the core timer itself. The block diagram shown in Figure 7.21 shows how we place our entire program in an SCTL timed at 40 MHz, so that each iteration executes within one 25 ns clock cycle. We then use the Square Wave Generator vi to create a square wave timebase with a period set by the *Repetition Period* control. Next we use the Edge Detector to detect the rising edges of our timebase, and on each rising edge, we reset the *Timer* subvi to zero. The timer subvi has the exact code shown in Figure 7.14, and tracks the number of ticks since each reset. We then use the *Pulse Generator* vi to configure a pulse state change at times *Pulse Start* and *Pulse Stop*, where these times are given as the number

of ticks elapsed with respect to the reset time t_0 provided by clock timer. The Pulse Generator block diagram has the code shown in Figure 7.19. The pulse generator's Boolean output then goes directly to the *laser control* digital output, which creates the TTL voltage that we can use to activate and extinguish a laser. Figure 7.21a shows a simple front panel for this FPGA.vi, where the times must be entered in the number of ticks due to the FPGA's inability to use double numbers.



(a) Front panel for FPGA.vi allowing us to configure the pulse timing. Timing information in specified in ticks, as the FPGA can not process floating point numbers.

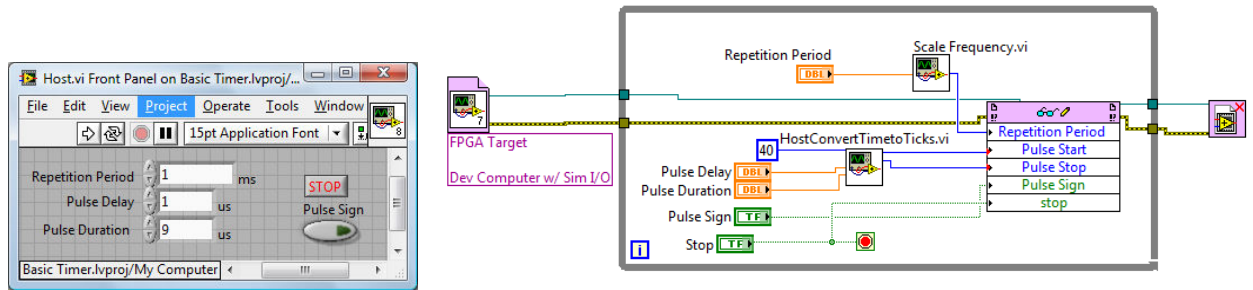
(b) Core FPGA.vi program for a digital delay generator. This includes a timebase, edge detection, and a pulse generator all executing within a 25 ns loop.

Figure 7.21: FPGA based code used for a digital delay generator.

We can take this example further and create an easier to use interface by creating a Host.vi file. Figure 7.22b shows how we can use the Host.vi pattern discussed earlier. It begins by opening a communication with the FPGA target, and then enters a loop where it continuously sends the configuration settings of our pulse generation to the FPGA. These settings include the *Repetition Period*, *Pulse Delay*, *Pulse Duration*, *Pulse Sign*, and a Stop command to exit the program. When we exit the program, the Host.vi breaks communication with the FPGA.

As our Host.vi program is executed on the computer instead of the FPGA, we can use double precision numbers to express our timing parameters, as shown in Figure 7.22a. We must however, convert these human-readable double precision numbers to a format which can be understood by the FPGA. Thus we use the subvis shown in Figure 7.22 to convert all times expressed in ms and μs into 40 MHz tick counts.

These figures show a fully usable but simple implementation of an FPGA based digital delay generator, using the concepts that we have developed throughout this chapter. The aim of this section was to outline a clear path of how we used the



(a) Host.vi front panel executing on the computer, which allows us to express the time in μs and ms.

(b) Back panel of Host.vi shows how the program communicates and sends the timing configuration to the FPGA based FPGA.vi.

Figure 7.22: Host.vi computer based interface program, which allows us more advanced interface features and functionality.



(a) HostConvertTimeToTicks.vi block diagram. Converts the pulse delay and pulse duration expressed in μs into a number of 40 MHz ticks.

(b) ScaleFrequency.vi block diagram. Converts the repetition frequency expressed in ms into a number of ticks.

Figure 7.23: The host vi uses these subvis to carry out conversions in order to convert our double precision time to a tick based format.

FPGA and basic logic structures to create a dynamic and powerful utility for timing and synchronization. While it is impossible to discuss the full-scale code used in the experiment due to its complexity, in the next section we will show the interfaces which illustrate a few of the tools that we were able to develop with these techniques.

7.5.1 Laser Timing via Pulse Delay Generation

The digital delay generator example we just developed offers a proof of concept for the timing applications we can implement with Labview FPGA. To control our quantum memory experiment, we expanded this application to provide more digital outputs, which allows us to control multiple lasers with 25 ns precision. We also added interface options which let us use an internally generated timebase to trigger the experiment, or send a TTL signal generated by the chopper's optical fork. Figure 7.24 shows the control panel for the MOT, which lets us configure all of the laser beam timings, as well as configure different timing sequences to run while the magnetic field

is cut. This allows us to select between the timing for the memory storage, Raman spectroscopy, optical density measurements, or other optimization steps, all from the same interface.

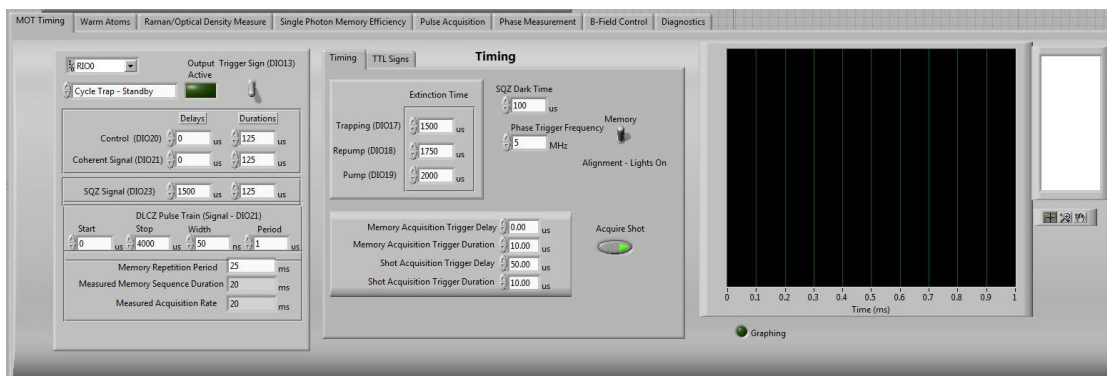


Figure 7.24: Interface used to control the MOT timing.

7.5.2 Chopper Period Measurement

We also developed a program to allow us to measure the pulses created by the optical chopper. As the chopper wheel turned, it output a TTL signal from its optical fork signifying the creation of a pulse. 7.25 shows the interface we developed to time the pulse arrival, and measure the mechanical jitter of the chopper.

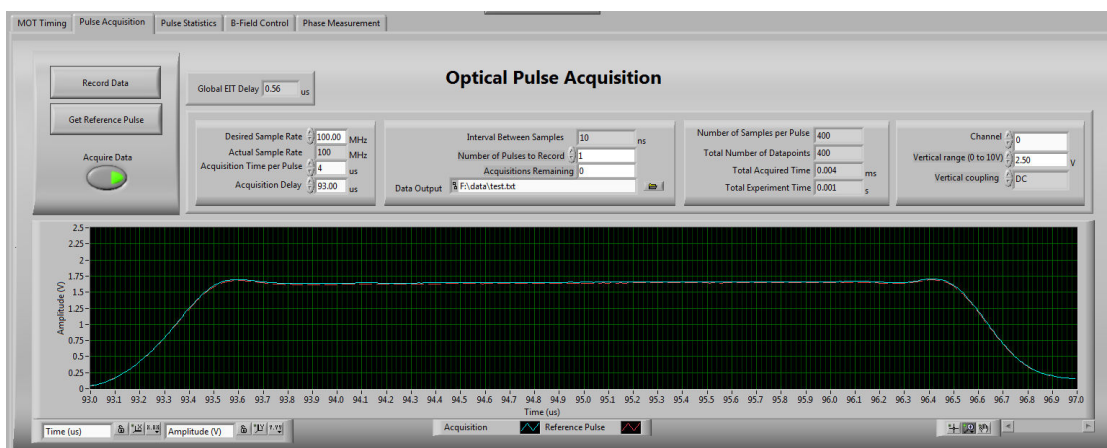


Figure 7.25: Interface use to measure pulses acquired from the optical chopper.

7.6 Where to find Source Code

All of the Labview code developed during this thesis can be found in the Git source code repository, located at <http://github.com/quantopt/eit-sequence> [Burks, 2010].

Conclusion

The recent development of the field of Quantum Information Processing has led to the discovery of new protocols for using quantum information in communication and computational applications. A quantum memory for light would serve as a core component in many of these applications such as quantum computing and long distance quantum information transfer, as it would allow us to synchronize the processing of quantum states. The technique of storing states of light in an atomic medium via EIT is currently a promising area of research due to its potential of obtaining reliable information transfer with long memory storage times. Our work during this thesis has focused on the novel goal of developing a quantum memory for squeezed light in a cold Cesium vapor.

In the first part of this thesis, we carried out a theoretical overview of Nonlinear and Quantum Optics in order to understand the mechanisms behind the generation of squeezed vacuum states. Next, we examined the development of a doubly degenerate OPO operating below threshold, which we used to generate -3 dB of squeezed vacuum resonant with the Cesium D_2 line at 852 nm. We then carried out a Quantum State Tomography of the homodyne measurements of these states, and by using the maximum likelihood estimation method, were able to reconstruct the state's density matrix and Wigner function. Finally we examined two methods of interfacing our squeezed vacuum with the Cesium atoms by creating squeezed pulses of light.

Once we obtained pulsed source of squeezed light, we began the construction of a quantum memory for Cesium. We examined the characteristics of a MOT that was built to cool and trap Cesium atoms, and we discussed the experimental techniques developed to create lasers at the necessary transitions, control the MOT's magnetic field, and time and synchronize different aspects of the experiment. We also discussed the results of characterizing the MOT performance with respect to its optical density, and our ability to cut the magnetic field.

Current Status and Future Outlook

The development of our quantum memory in cold Cesium atoms currently continues with the further optimization of the MOT performance, and the usage of Raman spectroscopy to completely cancel the magnetic field. Once these milestones are attained, work will turn towards the measurement of EIT in the MOT, and the storage and retrieval of a coherent state in our memory in order to establish a baseline memory efficiency. The successful storage of a coherent state will then allow us to continue with the storage of a squeezed state of light, and eventually the storage of entanglement in two separate quantum memories. Once these steps have been achieved, this will show the potential of using a Cesium based quantum memory as an element of quantum information processing.

Appendix

A Matisse Laser

The main laser that we use for squeezed light generation is a Matisse TR Titanium-Sapphire laser, provided by Spectra Physics. The laser is tunable from wavelengths of 770 nm up to 890 nm. In our usage, we pump this laser with 532 nm light provided by a Coherent Verdi V18 operating at 10 W. When we pump the Matisse with powers between 10 - 18 W, we can achieve between 2.2 - 4.2 W of output power at 852 nm. We chose to have an output coupler installed with a higher than normal transmissivity of $T=8\%$, in order to allow us the opportunity to pump it stably at higher powers. The laser outputs light in a TEM_{00} mode with a horizontal polarization.

The laser cavity has a ring shape shown in Figure 8.1, which is similar to other lasers used in our laboratory, and thus many of the components are described in detail in [Biraben, 1979], and [Bourzeix *et al.*, 1993]. The cavity has a length of 1.75 m, corresponding to a FSR of 170 MHz. The circulating cavity beam is focused onto a waist of 30 μm by two concave mirrors with a radius of curvature of $R = 150\text{mm}$.

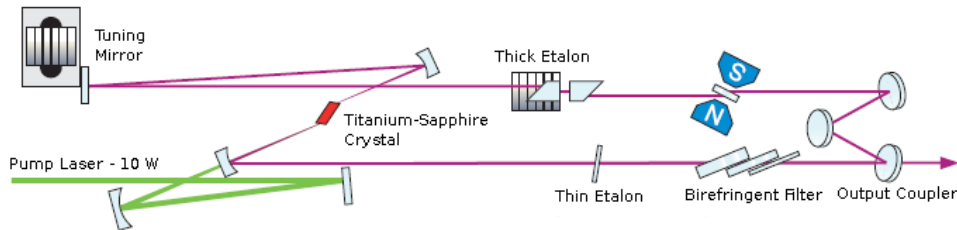


Figure 8.1: Illustration of the ring cavity for the Matisse TR laser. [Sirah Laser-und Plasmatechnik, 2006]

The laser frequency is tuned via three filters placed inside of the cavity: a birefringent filter, a thick etalon of $FSR = 20\text{GHz}$, and a thin etalon of $FSR = 150\text{GHz}$. The birefringent filter and thin etalon are adjusted via step motor, whereas the thick etalon is controlled with a piezo. We interface with the laser controls via the computer-based Matisse Commander interface software supplied by the manufacturer, which also allows us to lock the laser using its internal DSP control loop hardware.

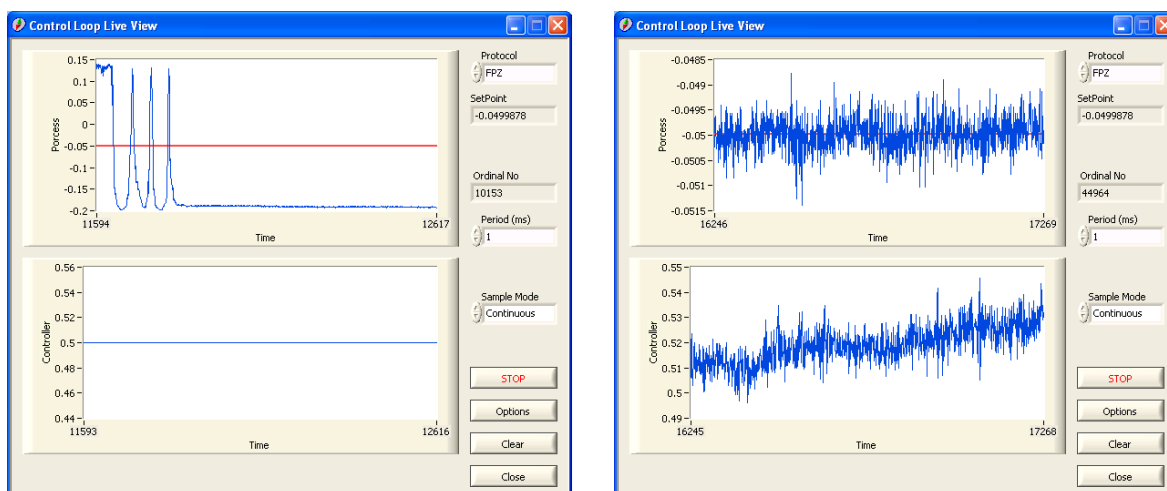
A.1 Laser Locking

In order to fix the laser's frequency at resonance with the Cesium D_2 line, we have implemented a system where we first lock that laser to a cavity, and then lock the cavity to the Cesium transition of interest using Saturated Absorption Spectroscopy. With these techniques, we manage to reduce the laser's linewidth down to 100 kHz when it is locked. In the next sections, we will outline the process of obtaining this lock.

A.1.1 Cavity Locking

We begin by locking the Matisse to a reference cavity using the fringe-side locking method. The cavity is a symmetric, linear, Fabry-Perot cavity made of Invar, with a length of $l = 240\text{mm}$ and having mirrors with a radius of curvature of $R = 1000\text{mm}$. The mirrors have a transmissivity of $T = 5\%$, and the cavity has a finesse of $\mathcal{F} = 60$, and a FSR of 625 MHz.

We send about 5 mW into this cavity, and detect the cavity peaks with a photodiode. We then send this photodiode output into the input connector of the laser communication box, which allows us to observe the cavity peaks in the Matisse Commander user interface, as shown in Figure 8.2a.



(a) Reference cavity peaks as observed in Matisse Commander. We lock to the middle of a fringe side

(b) Fast piezo lock is engaged at a setpoint near the side of a peak

Figure 8.2: We lock the laser to the cavity by using the side-fringe locking technique.



Figure 8.3: Matisse Commander Fast piezo gain and setpoint configuration.

Once we observe these peaks, we then can configure the fringe-side lock. We set the Fast Piezo controller of the Matisse to use gain of -2400 as shown in Figure 8.3, and a setpoint of -0.05, which corresponds to a light level at 50% of the cavity peak intensity. We then manually adjust the cavity length to position the output at the setpoint. When we enter the Control Loop Live View menu on the Matisse Commander and engage the Fast Piezo lock, we can see the Matisse lock to the cavity fringe, as we can see in Figure 8.2b.

While this compensates for rapid oscillations, we additionally adjust for slower derivations by locking with the Matisse's Slow Piezo. We again set a setpoint of 0.5, and apply a Free Proportional Gain of -1, a Locked Proportional Gain of -4, and a Locked Integral Gain of -4. When we then activate the Slow Piezo Control, the Matisse corrects for both slow and rapid drifts, as shown in Figure 8.4.

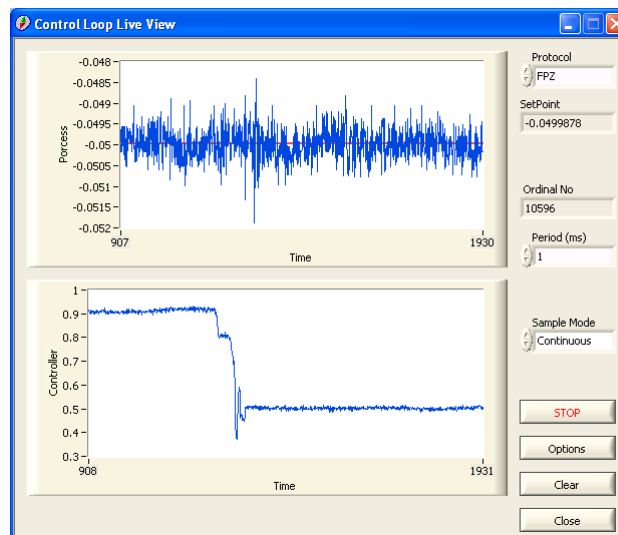


Figure 8.4: We engage the slow piezo lock, and the Matisse controller corrects for slow drifts of the cavity lock.

A.1.2 Saturated Absorption

Once we lock the laser to the cavity, we wish to fix the cavity position with respect to the atomic transition $F=4 \rightarrow F'=4$. We send another fraction of the Matisse beam through an AOM which is modulated at 30 kHz. This light then passes through into a Cesium cell, and we obtain the Doppler profile of our desired transition by using the saturated absorption technique. A photodiode detects the peaks and send the signal to the lock-in detector, which demodulates it at 30 kHz, and obtains an error signal. We send this error signal to a fast integrating circuit which is connected to the cavity piezo. In order to lock the reference cavity to our transition of interest, we slowly scan

the cavity length by adjusting its piezo, and then activate the integrator once the error signal is at zero for the proper transition. By closing this control loop, we lock the Matisse at resonance for our transition.

B Chopper Disc Diagram

We developed a disc in order to produce the desired optical pattern when passing the squeezed vacuum through the chopper. The disc was machined from a blank disc supplied by Scitec Instruments which we purchased along with the chopper. Figure 8.5 shows the specifications that we developed for the disc manufacture.

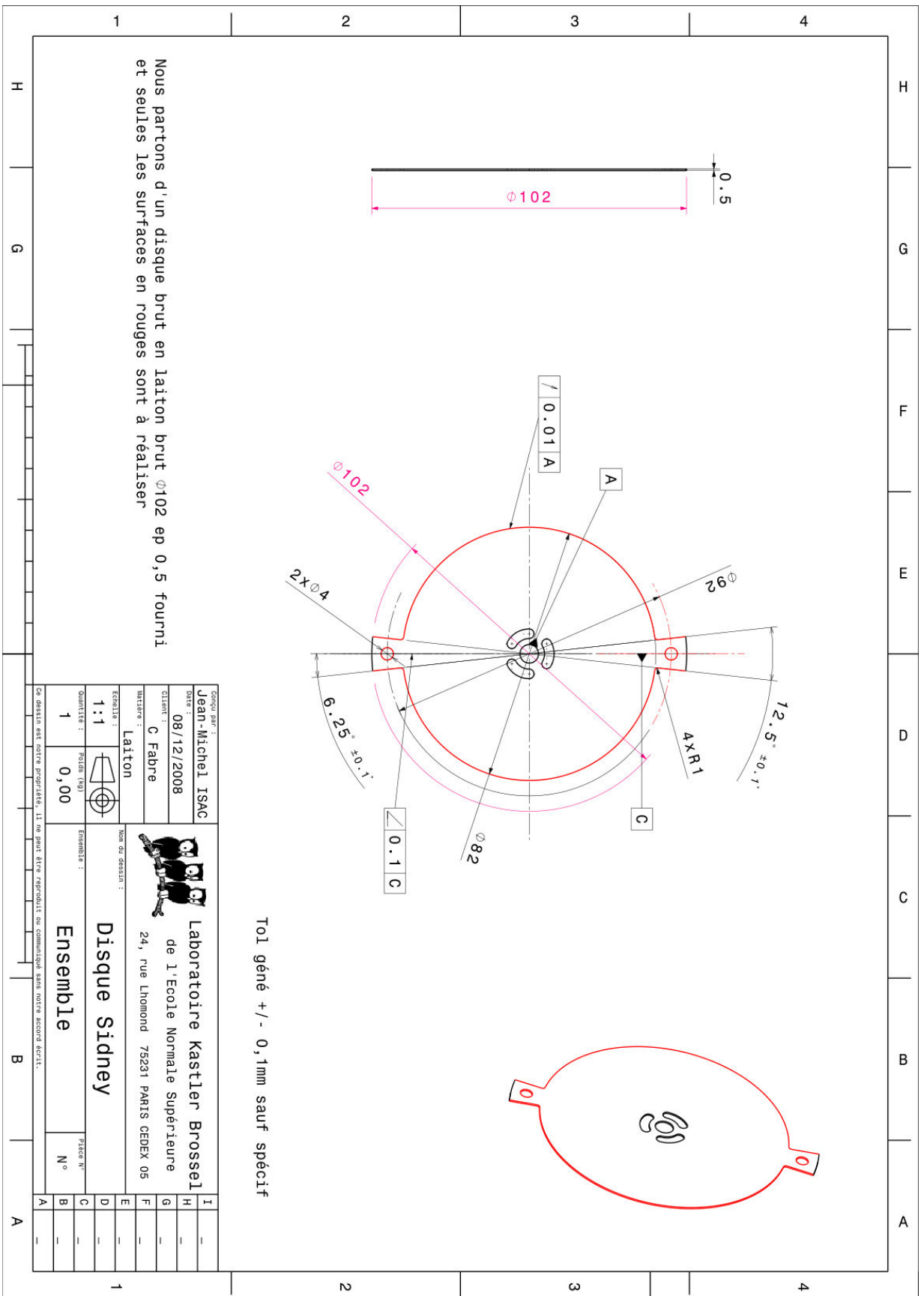


Figure 8.5: Chopper disc mechanical diagram

C Electronic Diagrams

The following figures show the electronic circuits developed over the course of this thesis, which were used to lock the doubling and OPO cavities, as well as the photodiode circuits used for tilt locking and Pound-Drever-Hall.

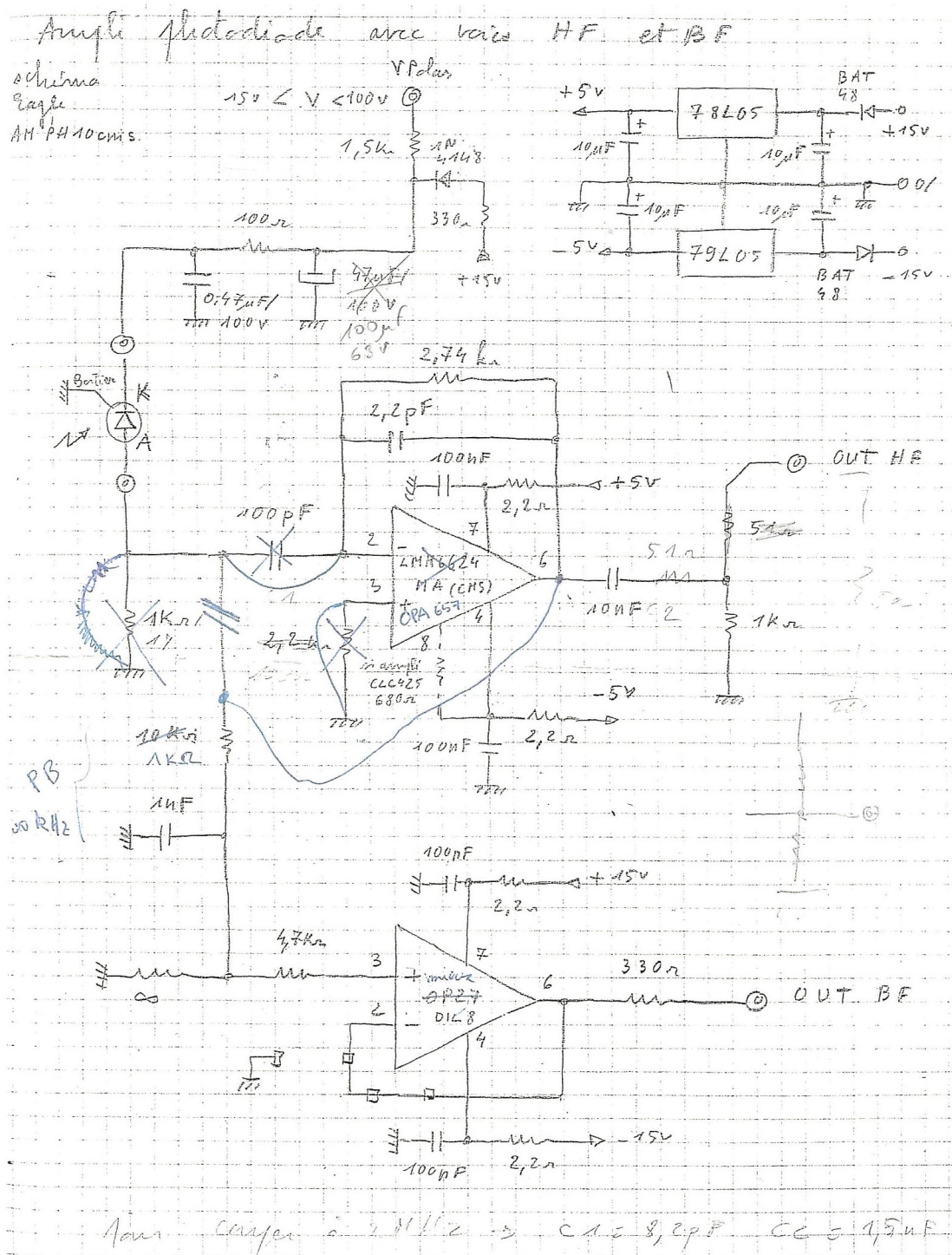


Figure 8.6: Electronic circuit developed for the low-noise, high photodiode amplifier used for Pound-Drever-Hall locking of the OPO.

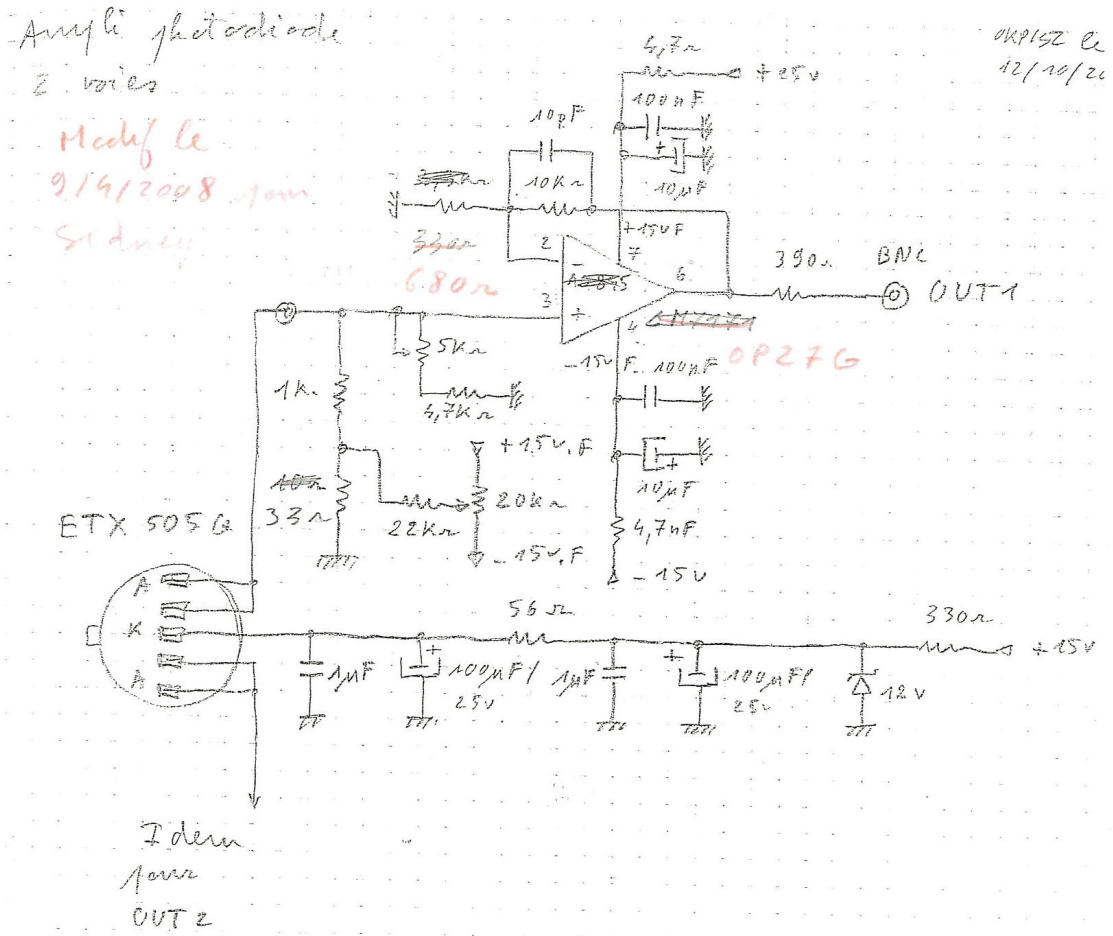


Figure 8.7: Electronic circuit developed for the tilt-locking photodiode amplifier used to lock the doubling cavity.

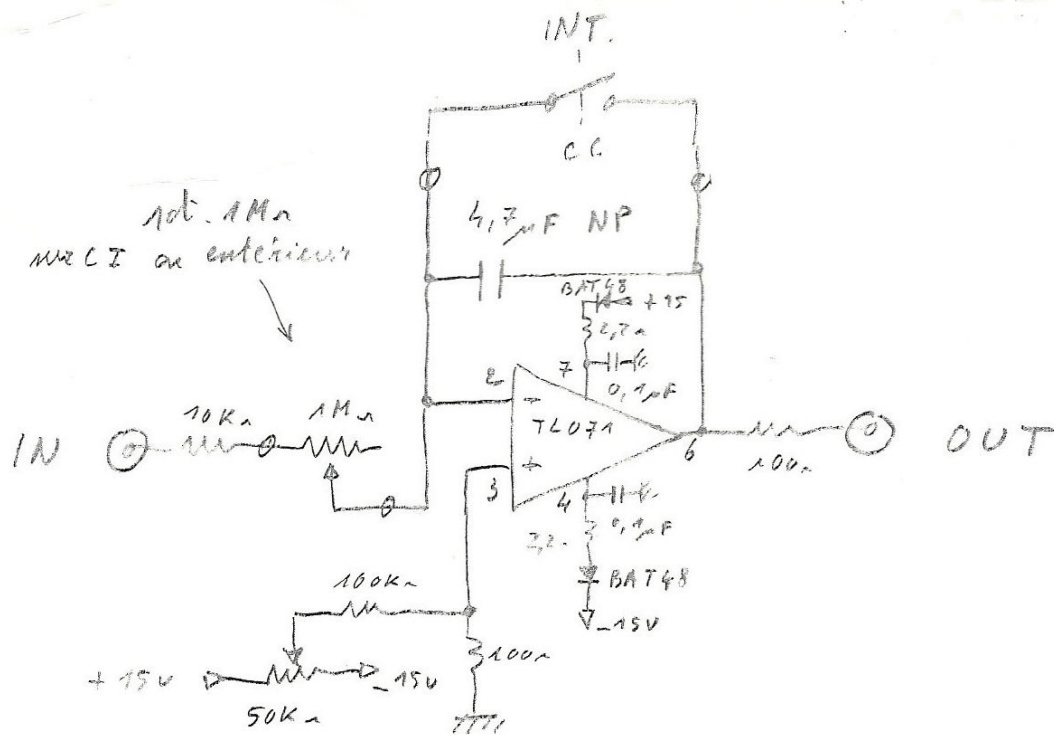


Figure 8.8: Integrator circuit used for the OPO's Pound-Drever-Hall lock.

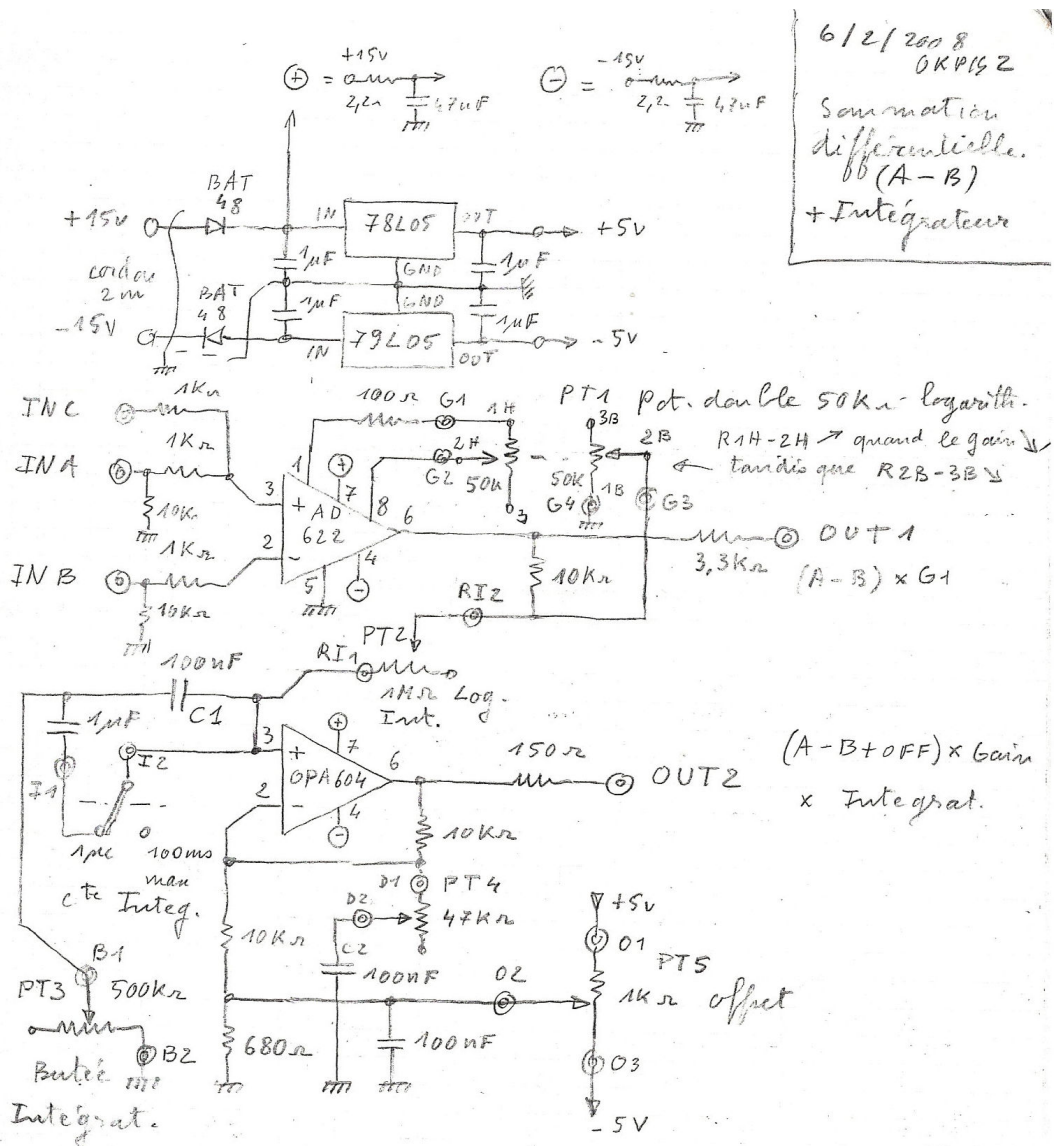


Figure 8.9: Difference and integrator circuit used to lock the doubling cavity via tilt-locking.

Bibliography

- [Aalto *et al.*, 2003] T. T. Aalto, M. Harjanne and M. Kapulainen, *Method for the rotational alignment of polarization-maintaining optical fibers and waveguides*, *Optical Engineering*, **42**, 2861–2867 (2003).
- [Abramovitch, 2002] D. Abramovitch, *Phase-locked loops: A control centric tutorial*, **1** (2002).
- [Alexander *et al.*, 2006] A. L. Alexander, J. J. Longdell, M. J. Sellars and N. B. Manson, *Photon Echoes Produced by Switching Electric Fields*, *Phys. Rev. Lett.*, **96**, 043602 (2006).
- [Appel *et al.*, 2008] J. Appel, E. Figueroa, D. Korystov, M. Lobino and A. I. Lvovsky, *Quantum memory for squeezed light*, *Phys. Rev. Lett.*, **100**, 093602 (2008).
- [Appel *et al.*, 2009] J. Appel, A. MacRae and A. Lvovsky, *A versatile digital GHz phase lock for external cavity diode lasers*, *Measurement Science and Technology*, **20**, 055302 (2009).
- [Arie *et al.*, 1997] A. Arie, G. Rosenman, V. Mahal, A. Skliar, M. Oron, M. Katz and D. Eger, *Green and ultraviolet quasi-phase-matched second harmonic generation in bulk periodically-poled KTiOPO₄*, *Optics Communications*, **142**, 265 – 268 (1997).
- [Arikawa *et al.*, 2009] M. Arikawa, K. Honda, D. Akamatsu, S. Nagatsuka, A. Furusawa and M. Kozuma, *Quantum memory of a squeezed vacuum for arbitrary frequency sidebands*, arXiv:0905.2816v1 [quant-ph] (2009).
- [Bachor and Ralph, 2004] H. Bachor and T. Ralph, *A Guide To Experiments In Quantum Optics*, wiley-vch (2004).

- [Baillard *et al.*, 2006] X. Baillard, A. Gauguet, S. Bize, P. Lemonde, P. Laurent, A. Clairon and P. Rosenbusch, *Interference-filter-stabilized external-cavity diode lasers*, *Opt. Comm.*, **266**, 609 (2006).
- [Banaszek *et al.*, 1999] K. Banaszek, G. M. D'Ariano, M. G. A. Paris and M. F. Sacchi, *Maximum-likelihood estimation of the density matrix*, *Phys. Rev. A*, **61**, 010304 (1999).
- [Bennett and Brassard, 1984] C. H. Bennett and G. Brassard, *Quantum cryptography: public key distribution and coin tossing*, Proceedings of IEEE International conference on computers, systems, and signal processing, page 175 (1984).
- [Biaggio *et al.*, 1992] I. Biaggio, P. Kerkoc, L.-S. Wu, P. Gunter and B. Zysset, *Refractive indices of orthorhombic KNbO₃. II. Phase-matching configurations for nonlinear-optical interactions*, *J. Opt. Soc. Am. B*, **9**, 507 (1992).
- [Biraben, 1979] F. Biraben, *Efficacité des systèmes unidirectionnels utilisables dans les lasers en anneau*, *Optics Comm.*, **29**, 353 (1979).
- [Black, 2001a] E. Black, *Notes on the pound-drever-hall technique*, Technical Note LIGO-T980045-00-D, **4**, 16–98 (2001).
- [Black, 2001b] E. D. Black, *An introduction to Pound–Drever–Hall laser frequency stabilization*, *American Journal of Physics*, **69**, 79–87 (2001).
- [Boulanger *et al.*, 2000] B. Boulanger, J.-P. Fève and Y. Guillien, *Thermo-optical effect and saturation of nonlinear absorption induced by gray tracking in a 532-nm-pumped KTP optical parametric oscillator*, *Opt. Lett.*, **25**, 484 (2000).
- [Bourzeix, 1995] S. Bourzeix, *Laser continu à 205 nm: application à la mesure du déplacement de Lamb dans l'hydrogène*, Ph.D Thesis, Université Pierre et Marie Curie (1995).
- [Bourzeix *et al.*, 1993] S. Bourzeix, M. D. Plimmer, F. Nez, L. Julien and F. Biraben, *Efficient frequency doubling of a continuous wave titanium:sapphire laser in an external enhancement cavity*, *Optics Comm.*, **99**, 89 (1993).
- [Boyd and Kleinman, 1968] G. D. Boyd and D. A. Kleinman, *Parametric interaction of focused gaussian light beams*, *J. Appl. Phys.*, **39**, 3597 (1968).
- [Boyd, 1992] R. Boyd, *Nonlinear Optics. 1992*, New York: Academic Press (1992).

- [Briegel *et al.*, 1998] H.-J. Briegel, W. Dur, J. I. Cirac and P. Zoller, *Quantum repeaters: the role of imperfect local operations in quantum communication*, Phys. Rev. Lett., **81**, 5932 (1998).
- [Burks, 2010] S. Burks, *Source Code*, Github repository - <http://github.com/quantopt> Public Domain (2010). sid137@alum.mit.edu.
- [Chanelière *et al.*, 2005] T. Chanelière, D. N. Matsukevich, S. D. Jenkins, S.-Y. Lan, T. A. B. Kennedy and A. Kuzmich, *Storage and retrieval of single photons transmitted between remote quantum memories*, Nature, **438**, 833 (2005).
- [Chanelière *et al.*, 2010] T. Chanelière, J. Ruggiero, M. Bonarota, M. Afzelius and J. Gouët, *Efficient light storage in a crystal using an atomic frequency comb*, New Journal of Physics, **12**, 023025 (2010).
- [Choi *et al.*, 2008] K. Choi, H. Deng, J. Laurat and H. Kimble, *Mapping photonic entanglement into and out of a quantum memory*, Nature, **452**, 67–71 (2008).
- [Cohen-Tannoudji *et al.*, 1973] C. Cohen-Tannoudji, B. Diu and F. Laloe, *Quantum Mechanics, Vol 1*, Editions Hermann (1973).
- [Coudreau, 1997] T. Coudreau, *Réduction du bruit et tomographie quantique d'un faisceau laser interagissant avec des atomes froids: théorie et expériences*, Ph.D Thesis, Université Pierre et Marie Curie (1997).
- [Courtilot, 2003] I. Courtilot, *Première observation de la transition fortement interdite $1S_0-3P_0$ du strontium, pour une horloge optique à atomes piégés*, Ph.D Thesis, Université Pierre et Marie Curie (2003).
- [Courty, 2005] J. M. Courty, *Optique Quantique, notes de course* (2005).
- [Curtin and O'Brien, 1999] M. Curtin and P. O'Brien, *Phase-Locked Loops for High-Frequency Receivers and Transmitters-Part 3*, Analog Dialogue, **33** (1999).
- [Cviklinski, 2008] J. Cviklinski, *Interface quantique atomes-champs en régime de variables continues*, Ph.D Thesis, Université Pierre et Marie Curie (2008).
- [Dantan, 2005] A. Dantan, *Génération, stockage et manipulation d'états non classiques pour des ensembles atomiques et des champs électromagnétiques*, Ph.D Thesis, Université Pierre et Marie Curie (2005).

- [Deutsch, 1985] D. Deutsch, *Quantum theory, the Church-Turing principle and the universal quantum computer*, Proceedings of the royal society of London A, **400**, 97 (1985).
- [Duan *et al.*, 2000] L.-M. Duan, G. Giedke, J. I. Cirac and P. Zoller, *Inseparability Criterion for Continuous Variable Systems*, Phys. Rev. Lett., **84**, 2722–2725 (2000).
- [Duan *et al.*, 2001] L.-M. Duan, M. D. Lukin, J. I. Cirac and P. Zoller, *Long-distance quantum communication with atomic ensembles and linear optics*, Nature, **414**, 413 (2001).
- [Eckardt *et al.*, 1991] R. C. Eckardt, C. D. Nabors, W. J. Kozlovsky and R. L. Byer, *Optical parametric oscillator frequency tuning and control*, J. Opt. Soc. Am. B, **8**, 646–667 (1991).
- [Eisaman *et al.*, 2005] M. D. Eisaman, A. André, F. Massou, M. Fleischhauer, A. S. Zibrov and M. D. Lukin, *Electromagnetically induced transparency with tunable single-photon pulses*, Nature, **438**, 837 (2005).
- [Ekert, 1991] A. K. Ekert, *Quantum cryptography based on Bell's theorem*, Phys. Rev. Lett., **67**, 661 (1991).
- [Fabre, 1990] C. Fabre, *Quantum noise in optical systems*, Les Houches, Session LIII, 1990, North-Holland (1990).
- [Fabre *et al.*, 1989] C. Fabre, E. Giacobino, A. Heidmann and S. Reynaud, *Noise characteristics of a non-degenerate Optical Parametric Oscillator-Application to quantum noise reduction*, Journal de Physique, **50**, 1209–1225 (1989).
- [Felinto *et al.*, 2005] D. Felinto, C. Chou, H. De Riedmatten, S. Polyakov and H. Kimble, *Control of decoherence in the generation of photon pairs from atomic ensembles*, Physical Review A, **72**, 53809 (2005).
- [Feynman, 1982] R. Feynman, *Simulating physics with computers*, International journal of theoretical physics, **21**, 467–488 (1982).
- [Fox, 2006] A. Fox, *Quantum optics: an introduction*, Oxford University Press, USA (2006).

- [Garrido Alzar *et al.*, 2007] C. Garrido Alzar, P. Petrov, D. Oblak, J. Mueller and E. Polzik, *Compensation of eddy-current-induced magnetic field transients in a MOT* (2007).
- [Garrison and Chiao, 2008] J. Garrison and R. Chiao, *Quantum Optics*, Oxford University Press, USA (2008).
- [Gerry and Knight, 2005] C. Gerry and P. Knight, *Introductory Quantum Optics*, Cambridge Univ Pr (2005).
- [Glauber, 1963] R. J. Glauber, *Coherent and incoherent states of the radiation field*, Phys. Rev., **131**, 2766 (1963).
- [Gorshkov *et al.*, 2007] A. Gorshkov, A. André, M. Lukin and A. Sørensen, *Photon storage in Λ -type optically dense atomic media. II. Free-space model*, Physical Review A, **76**, 33805 (2007).
- [Grover, 1996] L. K. Grover, *A fast quantum mechanical algorithm for database search*, Proceedings, 28th annual ACM symposium on the theory of computing, page 212 (1996).
- [Hansson *et al.*, 2000] G. Hansson, H. Karlsson, S. Wang and F. Laurell, *Transmission measurements in KTP and isomorphic compounds*, Appl. Opt., **39**, 5058 (2000).
- [Harris, 1997] S. Harris, *Electromagnetically induced transparency*, Physics Today, **50**, 36 (1997).
- [Heidmann *et al.*, 1987] A. Heidmann, R. J. Horowicz, S. Reynaud, E. Giacobino, C. Fabre and G. Camy, *Observation of quantum noise reduction on twin laser beams*, Phys. Rev. Lett., **59**, 2555 (1987).
- [Hilico, 1992] L. Hilico, *Réduction du bruit quantique de la lumière par une cavité bistable*, Ph.D Thesis, Université Pierre et Marie Curie (1992).
- [Hockel *et al.*, 2009] D. Hockel, M. Scholz and O. Benson, *A robust phase-locked diode laser system for EIT experiments in cesium*, Applied Physics B: Lasers and Optics, **94**, 429–435 (2009).
- [Honda *et al.*, 2008] K. Honda, D. Akamatsu, M. Arikawa, Y. Yokoi, K. Akiba, S. Nagatsuka, T. Tanimura, A. Furusawa and M. Kozuma, *Storage and retrieval of a squeezed vacuum*, Phys. Rev. Lett., **100**, 093601 (2008).

- [Hubel *et al.*, 2007] H. Hubel, M. R. Vanner, T. Lederer, B. Blauensteiner, T. Lorunser, A. Poppe and A. Zeilinger, *High-fidelity transmission of polarized encoded qubits from an entangled source over 100 km of fiber*, Opt. Express, **15**, 7853 (2007).
- [Joffre, 2009] M. Joffre, *Optique non-linéaire en régimes continu et femtoseconde*, notes de cours de Master 2 disponibles à l'adresse suivante: <http://www.enseignement.polytechnique.fr/profs/physique/Manuel.Joffre/onl/cours.pdf> (2009).
- [Josse, 2003] V. Josse, *Réduction du bruit de polarisation et intrication quantique en variables continues avec un nuage d'atomes froids*, Ph.D Thesis, Université Pierre et Marie Curie (2003).
- [Julsgaard *et al.*, 2004] B. Julsgaard, J. Sherson, J. I. Cirac, J. Fiurasek and E. S. Polzik, *Experimental demonstration of quantum memory for light*, Nature, **432**, 482 (2004).
- [Lam, 1998] P. K. Lam, *Applications Of Quantum Electro-Optic Control and Squeezed Light*, Ph.D Thesis, Australian National University (1998).
- [Lambrecht, 1995] A. Lambrecht, *Atomes froids et fluctuations quantiques*, Ph.D Thesis, Université Pierre et Marie Curie (1995).
- [Laurat, 2004] J. Laurat, *Etats non-classiques et intrication en variables continues à l'aide d'un oscillateur paramétrique optique*, Ph.D Thesis, Université Pierre et Marie Curie (2004).
- [Leonhardt, 1997] U. Leonhardt, *Measuring the Quantum State Of Light*, Cambridge Univ Pr (1997).
- [Lu-Ming *et al.*, 2008] L. Lu-Ming, T. Wen-Zhuo, H. Zhen-Yan and G. Hong, *Realization of Optical Phase Locked Loop at 9.2 GHz between Two Independent Diode Lasers*, Chinese Physics Letters, **25**, 3253–3256 (2008).
- [Lvovsky, 2004] A. Lvovsky, *Iterative maximum-likelihood reconstruction in quantum homodyne tomography*, Journal of Optics B: Quantum and Semiclassical Optics, **6** (2004).
- [Lvovsky *et al.*, 2009] A. Lvovsky, B. Sanders and W. Tittel, *Optical quantum memory*, Nature Photonics, **3**, 706–714 (2009).

- [Lvovsky and Raymer, 2009] A. I. Lvovsky and M. G. Raymer, *Continuous-variable optical quantum-state tomography*, *Rev. Mod. Phys.*, **81**, 299–332 (2009).
- [Mabuchi *et al.*, 1994] H. Mabuchi, E. S. Polzik and H. J. Kimble, *Blue-light-induced infrared absorption in KNbO₃*, *J. Opt. Soc. Am. B*, **11**, 2023–2029 (1994).
- [On Semiconductor, 2006] On Semiconductor, *MCH12140 Phase-Frequency Detector Datasheet* (2006).
- [Ortalo, 2009] J. Ortalo, *Transparence induite électromagnétiquement et mémoire quantique dans une vapeur de césium*, Ph.D Thesis, Université Pierre et Marie Curie (2009).
- [Reháček *et al.*, 2001] J. Reháček, Z. Hradil and M. Jezek, *Iterative algorithm for reconstruction of entangled states*, *Phys. Rev. A*, **63**, 040303 (2001).
- [Reid, 1988] M. Reid, *Quantum correlations of phase in nondegenerate parametric oscillation*, *Phys. Rev. Lett.*, **60**, 2731 (1988).
- [Reid, 1989] M. Reid, *Demonstration of the Einstein-Podolsky-Rosen paradox using non-degenerate parametric amplification*, *Phys. Rev. A*, **40**, 913 (1989).
- [Ringot *et al.*, 2001] J. Ringot, P. Szriftgiser and J. Garreau, *Subrecoil Raman spectroscopy of cold cesium atoms*, *Physical Review A*, **65**, 13403 (2001).
- [Schleich, 2001] W. Schleich, *Quantum optics in phase space*, Vch Verlagsgesellschaft MbH (2001).
- [Scully and Zubairy, 1997] M. Scully and M. Zubairy, *Quantum optics*, Cambridge Univ. Press (1997).
- [Shaddock, 2001] D. Shaddock, *Advanced Interferometry for Gravitational Wave Detection*, Ph.D Thesis, The Australian National University (2001).
- [Shaddock *et al.*, 1999] D. A. Shaddock, M. B. Gray and D. E. McClelland, *Frequency locking a laser to an optical cavity by use of spatial mode interference*, *Opt. Lett.*, **24**, 1499–1501 (1999).
- [Shen, 1984] Y. Shen, *The principles of nonlinear optics*, Wiley-Interscience, New York, NY, USA (1984).

- [Shor, 1994] P. W. Shor, *Algorithms for quantum computation: discrete logarithms and factoring*, Proceedings, 35th annual symposium on foundations of computer science, IEEE Press, Los Alamitos, CA, page 124 (1994).
- [Siegman, 1986] A. E. Siegman, *Lasers*, University Science Books, Mill Valley, California (1986).
- [Simon, 2000] R. Simon, *Peres-Horodecki Separability Criterion for Continuous Variable Systems*, Phys. Rev. Lett., **84**, 2726–2729 (2000).
- [Sirah Laser-und Plasmatechnik, 2006] Sirah Laser-und Plasmatechnik, *Matisse TR Datasheet* (2006).
- [Sørensen, 1998] J. L. Sørensen, *Nonclassical light for atomic physics and quantum teleportation*, Ph.D Thesis, University of Aarhus (1998).
- [Targat *et al.*, 2005] R. L. Targat, J.-J. Zondy and P. Lemonde, *75%-Efficiency blue generation from an intracavity PPKTP frequency doubler*, Optics Communications, **247**, 471 – 481 (2005).
- [Treppe and Fabre, 2005] N. Treppe and C. Fabre, *Criteria of Quantum Correlation in the Measurement of Continuous Variables in Optics*, Laser Physics, **15**, 187–194 (2005).
- [Vanherzeele *et al.*, 1988] H. Vanherzeele, J. D. Bierlein and F. C. Zumsteg, *Index of refraction measurements and parametric generation in hydrothermally grown KTiOPO₄*, Appl. Opt., **27**, 3314–3316 (1988).
- [Vernac, 2001] L. Vernac, *Etude expérimentale et théorique des fluctuations quantiques de champs et d'atomes couplés en cavité*, Ph.D Thesis, Université Pierre et Marie Curie (2001).
- [Villa *et al.*, 2007] F. Villa, A. Chiummo, E. Giacobino and A. Bramati, *High-efficiency blue-light generation with a ring cavity with periodically poled KTP*, Journal of the Optical Society of America B, **24**, 576–580 (2007).
- [Wigner, 1932] E. Wigner, *On the quantum correction for thermodynamic equilibrium*, Phys. Rev., **40**, 749 (1932).

-
- [Zhao *et al.*, 2008] B. Zhao, Y. Chen, X. Bao, T. Strassel, C. Chuu, X. Jin, J. Schmiedmayer, Z. Yuan, S. Chen and J. Pan, *A millisecond quantum memory for scalable quantum networks*, Nature Physics, **5**, 95–99 (2008).
- [Zhu and Hall, 1993] M. Zhu and J. Hall, *Stabilization of optical phase/frequency of a laser system: application to a commercial dye laser with an external stabilizer*, Journal of the Optical Society of America B, **10**, 802–816 (1993).